

Copyright  
by  
Michelle Diane Chabot  
2001

The Dissertation Committee for Michelle Diane Chabot  
Certifies that this is the approved version of the following dissertation:

**FORCE DETECTION OF NUCLEAR MAGNETIC RESONANCE  
USING DOUBLE-TORSIONAL MICRO-OSCILLATORS**

Committee:

---

John T. Markert, Supervisor

---

Alex de Lozanne

---

Josef Kas

---

Ken Shih

---

Dean Neikirk

**FORCE DETECTION OF NUCLEAR MAGNETIC RESONANCE  
USING DOUBLE-TORSIONAL MICRO-OSCILLATORS**

by

**MICHELLE DIANE CHABOT, B.A., M.A.**

**DISSERTATION**

Presented to the Faculty of the Graduate School of  
The University of Texas at Austin  
in Partial Fulfillment  
of the Requirements  
for the Degree of

**DOCTOR OF PHILOSOPHY**

THE UNIVERSITY OF TEXAS AT AUSTIN

August 2001

UMI Number: 3025004

UMI<sup>®</sup>

---

UMI Microform 3025004

Copyright 2001 by Bell & Howell Information and Learning Company.

All rights reserved. This microform edition is protected against  
unauthorized copying under Title 17, United States Code.

---

Bell & Howell Information and Learning Company  
300 North Zeeb Road  
P.O. Box 1346  
Ann Arbor, MI 48106-1346

To my family:

To my mother for giving me the love and support that only a mother can.

To my father for loving me even when I don't do "good."

To my sister for setting the highest of standards, and for killing the cockroach.

## ACKNOWLEDGEMENTS

*“Now, here, you see, it takes all the running you can do to keep in the same place.*

*If you want to get somewhere else, you must run at least twice as fast as that.”*

*- Lewis Carrol, in Through the Looking Glass*

First I must give my extreme gratitude to my advisor John T. Markert. Not only for his endless support and advice, but also for allowing me to stop running and catch my breath when I needed to. I also want to thank him for instilling a friendly and cooperative atmosphere in his lab. And to the Markert lab – those that are long gone, those that are still here, and those that are leaving with me – it’s been remarkably fun. Thanks for all the help – with the experiments, with the computers (Troy), and with the crosswords.

To my closest friends I also want to say thank you. To Bob (Wiggle), Dave (the original Mang), Jen (Sunshine), and Casey (the Kid): I don’t know what to say except thank you for everything. I wouldn’t have made it without you guys. And even if I had, I definitely wouldn’t have smiled as much! And of course to Nicole Jamison – doctor, mother, and wife: Nik, no matter what other new and great titles you may acquire over the years, you will always be my best friend. Some things really do never change, and I thank you for that.

Finally, to my family, for their love, support, and encouragement. (Now I really win Daughter-of-the-Year, don’t I?) Joking aside, I really do mean it. *Thank you.*

# FORCE DETECTION OF NUCLEAR MAGNETIC RESONANCE USING DOUBLE-TORSIONAL MICRO-OSCILLATORS

Publication No. \_\_\_\_\_

Michelle Diane Chabot, Ph.D.  
The University of Texas at Austin, 2001

Supervisor: John T. Markert

The nuclear magnetic resonance of a sample of ammonium sulfate has been detected by coupling the magnetic force from the spins to a double torsional micro-oscillator. A single-sweep sensitivity of  $3 \times 10^{-15}$  N/Hz<sup>1/2</sup> was observed at room temperature for a sample-on-oscillator configuration. Microelectronic fabrication techniques were employed to create the high-Q single crystal silicon multiple torsional oscillators. With no sample mounted, the upper resonances of the oscillators were found to have force sensitivities as low as  $1.5 \times 10^{-16}$  N/Hz<sup>1/2</sup> at room temperature. The design, fabrication, and characterization of these novel oscillators are discussed. Also, non-adiabatic and relaxation effects on the observed force signal in nuclear magnetic resonance force microscopy are considered in detail.

## TABLE OF CONTENTS

<b>Acknowledgements</b>	<b>v</b>
<b>Abstract</b>	<b>vi</b>
<b>Chapter 1. Introduction</b>	<b>1</b>
<b>Chapter 2. Magnetic Resonance Force Microscopy</b>	<b>4</b>
2.1 General Theory . . . . .	4
2.1.1 Nuclear Magnetic Resonance . . . . .	4
2.1.2 Force Detection of Magnetic Resonance . . . . .	7
2.1.3 Oscillation of Magnetization: Cyclic Adiabatic Inversion . . . . .	8
2.1.4 Scanning Techniques . . . . .	11
2.1.5 Sensitivity Comparison . . . . .	14
2.2 Specific Experimental Concerns . . . . .	15
2.2.1 The Ideal Signal . . . . .	15
2.2.2 Non-Adiabatic Effects . . . . .	17
2.2.3 Relaxation Effects During Inversion . . . . .	19
2.2.4 Measuring Relaxation Times . . . . .	26
<b>Chapter 3. Mechanical Oscillators</b>	<b>29</b>
3.1 Design . . . . .	29
3.1.1 Damping Minimization . . . . .	29
3.1.2 Spring Constant Considerations . . . . .	31
3.1.3 Estimated Resonant Frequencies . . . . .	32
3.2 Fabrication of Boron-Doped Silicon Oscillators . . . . .	34
3.2.1 Mask Creation . . . . .	34
3.2.2 Wafer Patterning . . . . .	36
3.2.3 Oxide Etch . . . . .	40



3.2.4	Boron Implant and Anneal . . . . .	42
3.2.5	Final KOH Etch . . . . .	43
3.2.6	Extraction: Overcoming Stiction . . . . .	47
3.3	Fabrication of Oscillators from SOI Wafers . . . . .	48
3.4	Characterization . . . . .	51
3.4.1	Frequency Scans . . . . .	51
3.4.2	Resonances of Double-Torsional Oscillators . . . . .	54
3.4.3	Low Temperature Run . . . . .	56
3.4.4	Thickness Measurements . . . . .	57
3.4.5	Force Sensitivity . . . . .	60
<b>Chapter 4. NMRFM Experimental Apparatus and Considerations</b>		<b>61</b>
4.1	Cryostat Probe . . . . .	61
4.2	Fiber-Optic Interferometer . . . . .	65
4.2.1	Photo Diode Circuitry and Considerations . . . . .	65
4.2.2	Feedback Circuit for Fringe Stability . . . . .	68
4.3	Magnetic Field Gradients . . . . .	70
4.4	Modulation Electronics . . . . .	72
4.5	Sample Mounting . . . . .	72
<b>Chapter 5. Force Detection of NMR: Results of a 1D Scan</b>		<b>80</b>
5.1	Experimental Parameters . . . . .	80
5.2	Results . . . . .	83
5.2.1	Signal Artifact . . . . .	83
5.2.2	Signal Caused by Nuclear Magnetic Resonance . . . . .	84
5.3	Summary . . . . .	87
<b>Appendices</b>		<b>89</b>
<b>Appendix A. Relevant Reference Values</b>		<b>90</b>
<b>Appendix B. Fringe-Stability Circuit: Directions for Use</b>		<b>92</b>
<b>Bibliography</b>		<b>95</b>
<b>Vita</b>		<b>100</b>

# CHAPTER 1

## INTRODUCTION

*“I have yet to see any problem, however complicated, which when you looked at it in the right way, did not become still more complicated.”*

*- Poul Anderson, in John D. Barrow’s Book of Nothing*

Magnetic Resonance Force Microscopy (MRFM) is a quickly growing field with applications in all areas of science. Developed initially by Sidles [1-3] in 1991, it has been adapted and improved upon by various groups. The basic idea is that it directly detects the force created by an oscillating magnetization by coupling it via a field gradient to a mechanical oscillator. This novel method offers significant improvement in sensitivity over the conventional inductive measurement technique. Thus far, a main focus of MRFM has been towards electron spin resonance (ESRFM) detection [4-8], due to not only the popular appeal of being able to “image” an electron, but also because the magnetic moment of the electron is more than 650 times larger than that of common nuclei. The first successful force detection of magnetic resonance was observed in an ESR experiment performed by Rugar’s group at IBM [4]. Their results displayed a force sensitivity of  $10^{-14}$  N with a spatial resolution of 19  $\mu\text{m}$ . Subsequently, they published the first images generated from an MRFM experiment [5].

The idea of nuclear magnetic resonance force microscopy (NMRFM) appeals greatly to the area of condensed matter physics, since thus far the ability to do NMR

studies of thin films and other interesting sub-micron materials has been elusive. After their ground-breaking ESRFM experiment, Rugar performed the first successful NMRFM experiment [9]. They saw the response from ammonium nitrate with a force sensitivity of  $5 \times 10^{-16}$  N. The NMR origin of the sample was verified by measuring the signal at different positions and frequencies, as is done in this study (See Chapter 5). Rugar's experiment was also the first to use cyclic adiabatic inversion, a method for manipulating the magnetization which was first suggested by Sidles [10]. Following Rugar's experiment, a few other groups have successfully demonstrated the ability to detect NMR via a direct force measurement [11-15]. Alloul's group at Ecole Polytechnique, France, has recently performed NMRFM experiments to measure relaxation times [11], as is frequently done in conventional NMR and as is discussed in this work (Chapter 2). Sidles' group at University of Washington continues to make significant improvements in the control and detection apparatus [16-18]. This work attempts to demonstrate our ability to do NMR via force detection, with focus given to the mechanical oscillators which are integral to the experiment and to the eventual force sensitivity limits.

In the quest for improved sensitivity, mechanical oscillators need to be made which have low enough thermal noise as to allow for the detection of small volumes of spins. Due to the frequency restrictions imposed by the method used for manipulating the magnetization, this is done mainly through improving the quality factor and decreasing the effective spring constant. Microelectronic fabrication techniques are employed to achieve these goals. This work focuses on the design, fabrication, and characterization of single-crystal silicon multiple-torsional micro-oscillators, as will be discussed in Chapter 3. Chapter 2 presents an overview of the basic theory of MRFM and a thorough discussion of some of the lesser-understood parameters of this new field. During the inversion of the magnetization, non-adiabatic and relaxation effects are present which must be carefully considered in order to successfully and accurately detect and interpret the force signal. Chapter 4 outlines the experimental design, including the main mechanical and electronic components of the microscope.

Finally, an experiment demonstrating the capabilities of this instrument is detailed in Chapter 5, with evidence given to show the NMR origin of the detected signal.

## CHAPTER 2

### MAGNETIC RESONANCE FORCE MICROSCOPY

*“All of us were stuck to the surface of a ball, incidentally. The planet was ball-shaped. Nobody knew why we didn’t fall off, even though everybody pretended to kind of understand it.”*

*- Kurt Vonnegut, Breakfast of Champions*

#### 2.1 GENERAL THEORY

To comprehend and construct all facets of a magnetic resonance force microscopy experiment, a wide range of topics must first be well understood. Therefore, some basics of nuclear magnetic resonance will be touched upon, followed by the details of force detection of magnetic resonance. Finally, since this is a relatively new field, a thorough discussion of some unknown experimental parameters will be given.

##### 2.1.1 NUCLEAR MAGNETIC RESONANCE

An overview of the relevant topics in conventional NMR will be given here [18-20], treated in a classical manner for ease of understanding.

It is well known that a magnetic moment  $\vec{\mu}$  in an applied external field  $\vec{H}_o$  experiences a torque equal to  $\vec{\mu} \times \vec{H}_o$ , which also equals the rate of change of the angular momentum  $\vec{J}$ . This causes it to precess about  $\vec{H}_o$  at the Larmor frequency,  $\omega_o = \gamma H_o$ , where  $\gamma$  is the gyromagnetic ratio of the nuclei being probed. Taking into

account all the magnetic moments in the sample yields the bulk magnetic moment,  $\vec{M} = \gamma \vec{J}$ , whose equation of motion for can be written as:

$$\frac{d\vec{M}}{dt} = \gamma \vec{M} \times \vec{H}_o. \quad (2.1)$$

$\vec{H}_o$  is chosen to be along the  $\hat{z}$  axis, and a circulating<sup>1</sup> radio frequency field  $\vec{H}_1$  is applied in the  $xy$  plane with a frequency  $\omega_{rf}$ :

$$\vec{H}_1 = H_1 (\cos(\omega_{rf}t) \hat{x} + \sin(\omega_{rf}t) \hat{y}). \quad (2.2)$$

Transforming to a rotating frame  $(x', y', z)$  where the rf field is static<sup>2</sup>, the equation of motion becomes:

$$\frac{d\vec{M}}{dt} = \gamma \vec{M} \times \left[ \underbrace{\left( H_o - \frac{\omega_{rf}}{\gamma} \right) \hat{z} + H_1 \hat{x}'}_{\equiv \vec{H}_{eff}} \right]. \quad (2.3)$$

$$\equiv \vec{H}_{eff} \quad (2.4)$$

The last term in this expression is the effective field ( $\vec{H}_{eff}$ ) that the magnetization sees. In the rotating frame  $\vec{H}_{eff}$  is static, but in the lab frame it rotates about the  $\hat{z}$  axis at a frequency  $\omega_{rf}$ . Now, if  $\omega_{rf} = \omega_o = \gamma H_o$ , then the  $\hat{z}$  component of  $\vec{H}_{eff}$  disappears and  $\vec{H}_{eff} = H_1 \hat{x}'$ . When this criterion is met, the system is considered to be *on resonance*.

Recall that a moment in a field will precess about that field with a frequency  $\omega = \gamma H$ . Thus in the rotating frame, the spins precess about  $H_{eff}$  at  $\omega = \gamma H_{eff}$ . This leads directly to the basis of pulse NMR. If the rf field is applied suddenly at resonance for some time  $t = \frac{\theta}{\gamma H_1}$ , then the magnetization will rotate by  $\theta$  in the  $y'/z$  plane (about the  $x'$  axis). Thus if the time is chosen to be  $\frac{\pi}{2\gamma H_1}$ , then the

---

<sup>1</sup>In practice, it is experimentally more feasible to apply a linear rf field  $H_x = 2H_1 \cos \omega_{rf}t$ . This field can be decomposed into two rotating elements, one which precesses counterclockwise as desired, and one which precesses clockwise. Without a loss of generality, the clockwise field can be neglected since it has no effect on the precession of the magnetic moments.

<sup>2</sup>Recall the transformation laws for vectors and their time-dependent component:  $\vec{A} \rightarrow \vec{A}$  and  $\dot{\vec{A}} \rightarrow \dot{\vec{A}} + \omega_{rot} \times \vec{A}$

magnetization rotates by  $\pi/2$  so that it is parallel to the  $y'$  axis. In conventional NMR,  $\pi/2$  and  $\pi$  pulses are used to manipulate the magnetization, and the resulting precession which takes place in the  $x'y'$  plane induces a measurable voltage in a pickup coil.

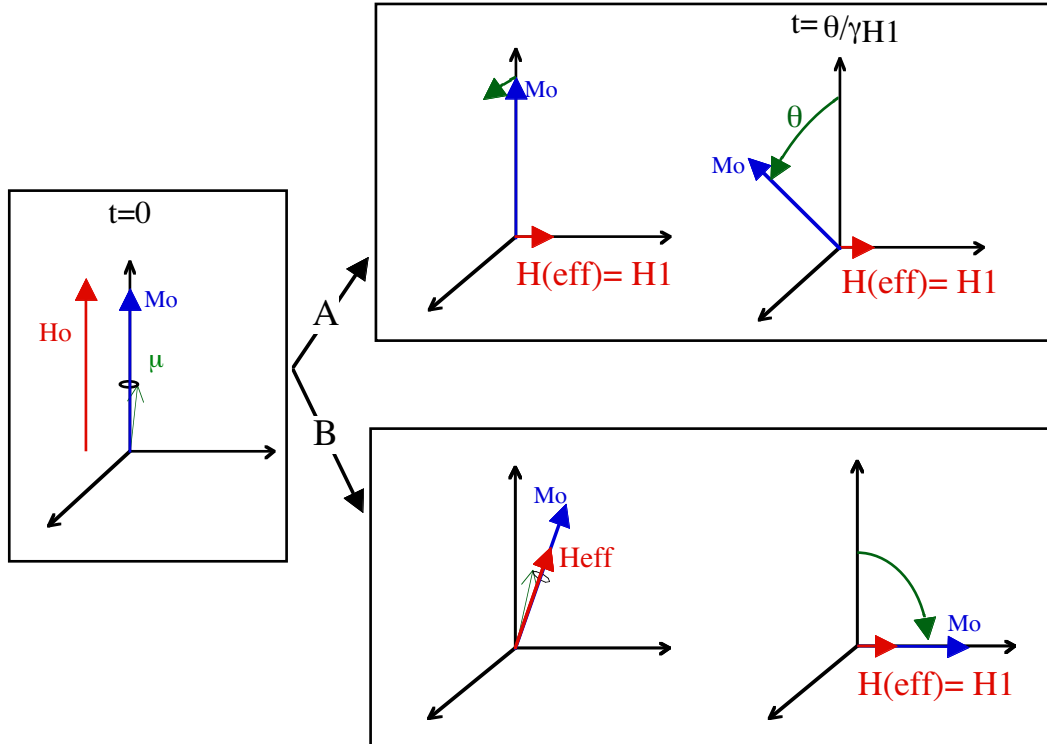


Figure 2.1: At  $t = 0$  the magnetization is aligned with the external field. (a) If the rf field  $H_1$  is turned on suddenly, the magnetization will rotate about this field with a frequency  $\gamma H_1$ . (b) If instead the rf field is slowly ramped to its resonance value, then the magnetization is spin-locked with it and will follow the field.

There are two main ways of manipulating the magnetization and the distinction is crucial. Both situations are illustrated in Figure 2.1. In the pulse technique described above, the magnetization, which is initially in equilibrium with  $H_o$ , rotates about the effective field  $H_1 \hat{x}'$  until the rf field is turned off. At this point the magnetization decays back to its equilibrium value with  $H_o$  parallel to  $\hat{z}$ . However, if the rf field is applied so that the effective field is *slowly* moved from its initial value of  $H_o \hat{z}$

to some final value  $\vec{H}_{eff}$ , then the moments continue to rotate about the effective field the entire time, causing the magnetization to *follow* it. Cyclic adiabatic inversion, an important application of this method, will be discussed in detail in Section 2.1.3.

### 2.1.2 FORCE DETECTION OF MAGNETIC RESONANCE

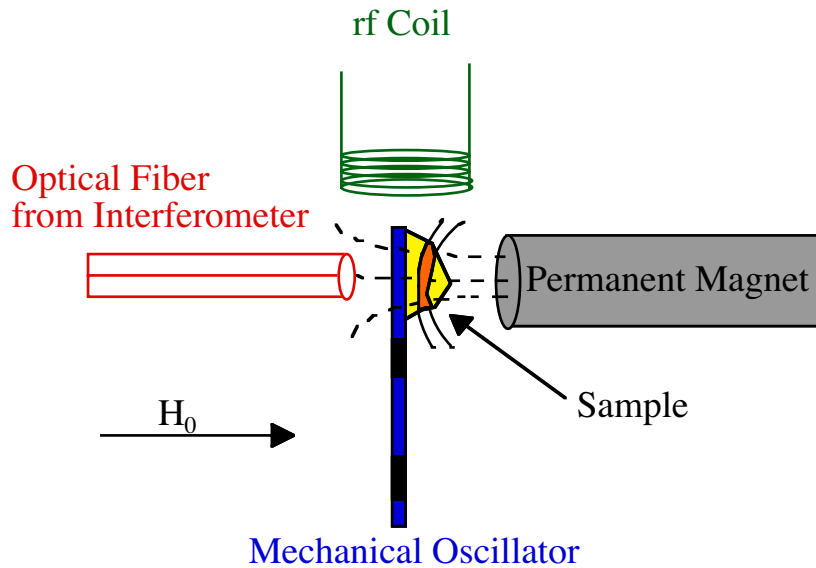


Figure 2.2: Basic set-up used in a nuclear magnetic resonance force microscope. The permanent magnet and the sample can be interchanged without any effect on the resulting force.

NMRFM directly couples the magnetization in a sample to a mechanical oscillator through an applied field gradient, instead of using a pickup coil for detection as is done conventionally. The magnetization is oscillated at the resonance frequency of the mechanical oscillator using rf radiation applied through a coil, and the resulting force is given by:

$$\vec{F} = (\vec{M} \cdot \vec{\nabla}) \vec{B}. \quad (2.5)$$

Since this work focuses on one-dimensional NMRFM, equation 2.5 can be rewritten



as:

$$F_z(t) = M_z(t) \frac{\partial B}{\partial z}, \quad (2.6)$$

where a constant field gradient has been assumed. From this, it is clear that an oscillating magnetization will result in an oscillating force in the presence of a magnetic field gradient. As depicted in Figure 2.2, the amplitude of the oscillation is detected with a fiber optic interferometer, giving a measurement of the force and therefore the magnetization. Since the magnetization is made to oscillate at the resonance frequency of the mechanical oscillator, the detected amplitude,  $A_z$ , is enhanced by the quality factor,  $Q$ , of the oscillator:

$$A_z = \frac{F_z Q}{k}, \quad (2.7)$$

where  $k$  is the effective spring constant of the mechanical oscillator.

### 2.1.3 OSCILLATION OF MAGNETIZATION: CYCLIC ADIABATIC INVERSION

One extremely important component of NMRFM is the method with which the magnetization is inverted at the resonance frequency of the mechanical oscillator. The method of interest here is referred to as cyclic adiabatic inversion (Figure 2.3). The frequency of the applied rf field is slowly varied so that the effective field has a  $z$  component of oscillation at the resonance frequency of the mechanical oscillator,  $\omega_{osc}$ . By varying the field “slowly enough”, the magnetization will “follow” it, as mentioned in Section 2.1.1. This statement leads to the *adiabatic condition*<sup>3</sup> :

$$\gamma H_1 \gg \omega_{osc}. \quad (2.8)$$

In other words, the speed at which the spins are rotating about the effective field, (which has a minimum value at  $\gamma H_1$ ), must be much faster than the speed at which

---

<sup>3</sup>The expression given here is actually an approximation of the exact adiabatic condition which takes into account the time-variation of the angular velocity of the effective field during one cycle. However, this is not important for the current discussion and will be treated in detail in Section 2.2.1.

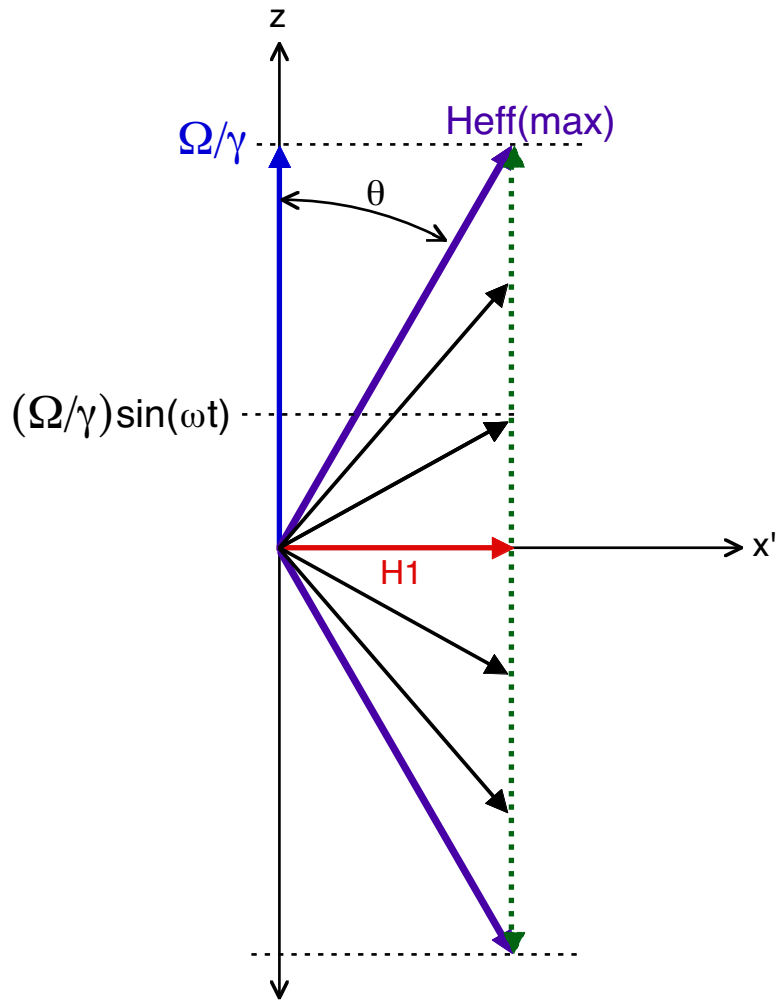


Figure 2.3: The path of the effective field during cyclic adiabatic inversion as seen in the rotating frame.

the effective field is moving, ( $\sim \omega_{osc}$ ). If this condition is not met, some of the moments will be lost, resulting in a decay of the magnetization following  $H_{eff}$  over the period of oscillation.

This time-dependent effective field is achieved by applying a time-dependent rf signal through the coil:

$$\omega_{rf}(t) = \omega_o + \Delta\omega_{rf}(t), \quad (2.9)$$

where  $\omega_o$  is the Larmor frequency and  $\Delta\omega_{rf}(t)$  is a sinusoidal modulation at the resonance frequency of the mechanical oscillator, given by:

$$\Delta\omega_{rf}(t) = \Omega \sin \omega_{osc}t. \quad (2.10)$$

Therefore, the effective field is:

$$\vec{H}_{eff}(t) = \frac{-\Delta\omega_{rf}(t)}{\gamma} \hat{z} + H_1 \hat{x}' = \frac{-\Omega}{\gamma} \sin \omega_{osc}t \hat{z} + H_1 \hat{x}'. \quad (2.11)$$

Initially, the net magnetization is equal to its equilibrium value along  $H_o$  ( $\equiv M_o$ ). The rf field is then turned on far off resonance ( $\approx 400$  kHz) and slowly ramped toward resonance as the cyclic adiabatic inversion process is started. If the adiabatic condition is met and relaxation effects are neglected, the magnetization  $M_z$  can be found from simple trigonometry:

$$\cos \theta = \frac{M_z}{M_o} = \frac{\vec{H}_{eff} \cdot \hat{z}}{H_{eff}}, \quad (2.12)$$

where  $\theta$  is the angle the effective field makes with the  $z$  axis. This leads directly to an expression for the  $\hat{z}$  component of the magnetization:

$$M_z(t) = M_o \frac{\frac{\Omega}{\gamma} \sin \omega_{osc}t}{\sqrt{(\frac{\Omega}{\gamma} \sin \omega_{osc}t)^2 + H_1^2}}. \quad (2.13)$$

This expression is plotted in Figure 2.4 for various values of  $\frac{\Omega}{\gamma H_1}$ . The most obvious feature is that, when  $\frac{\Omega}{\gamma}$  is large compared to  $H_1$ , the maximum  $z$  component

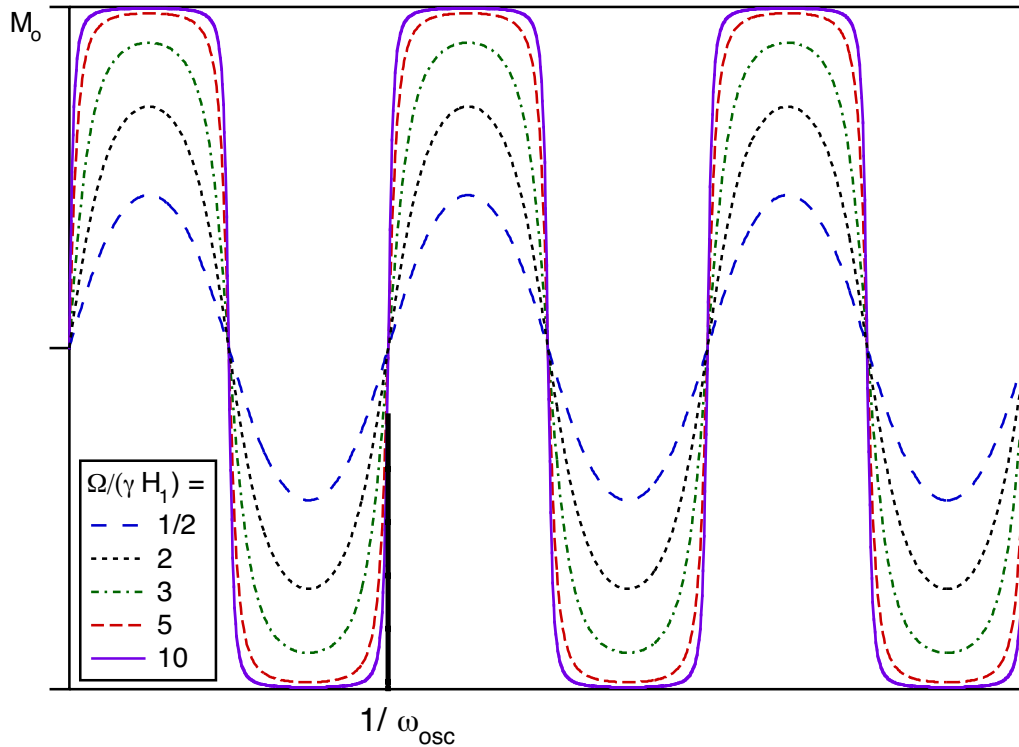


Figure 2.4: Equation 2.13 for the  $z$  component of the magnetization plotted for various values of  $\frac{\Omega}{\gamma H_1}$ .

of the magnetization approaches  $M_o$ , and the oscillation becomes more square-wave-like.<sup>4</sup> This topic will be revisited in Section 2.2.1.

#### 2.1.4 SCANNING TECHNIQUES

The terminology used to describe the force detection of NMR has been irreversibly entwined with the word microscopy. This stems from its first intended applications in the field of biology, in which MRFM has the potential to do magnetic resonance imaging (MRI) with much greater sensitivities than currently possible. However, for

<sup>4</sup>However, it is the first component of the Fourier expansion at the resonance frequency of the mechanical oscillator which contributes most to the observed force. This fact should be considered when analyzing results.

the purposes relevant to this work, no physical images will be created. Instead, the present microscope is used to scan over the sample in one dimension and give the corresponding forces which are detected at each point.

The spatial resolution is a key parameter of the microscope. It is determined by the resonance shell which is determined by the permanent magnet which supplies the field gradient (Figure 2.5). This is easily understood by considering that the static field actually experienced by the sample is  $\vec{H}_{total} = \vec{H}_o + \vec{H}_{pm}$ , where  $\vec{H}_{pm}$  is the field from the permanent magnet.  $\vec{H}_o$  is constant over the entire sample. However,  $\vec{H}_{pm}$  clearly varies significantly. Therefore only part of the sample will fulfill the resonance condition  $\gamma(|\vec{H}_o + \vec{H}_{pm}|) = \omega'_o$ . (Here  $\omega'_o$  refers to the adjusted Larmor frequency taking into account the static field from the permanent magnet.)

Thus the spatial resolution is determined by the thickness of this resonance slice. This is determined by two main factors: the strength of the field gradient and the modulation amplitude  $\Omega$  of cyclic adiabatic inversion. The first should be obvious, since a stronger field gradient results in a thinner slice because the value of the field is changing more rapidly with distance. The dependence on  $\Omega$  results from how many spins are “grabbed” during the inversion of the magnetization. (See Figure 2.5.) Since the frequency is modulated about resonance, a larger deviation from resonance will result in a larger volume of spins contributing to the force and thus the detected signal. Likewise, for a smaller deviation about resonance, fewer spins will contribute and the force exerted will be smaller.

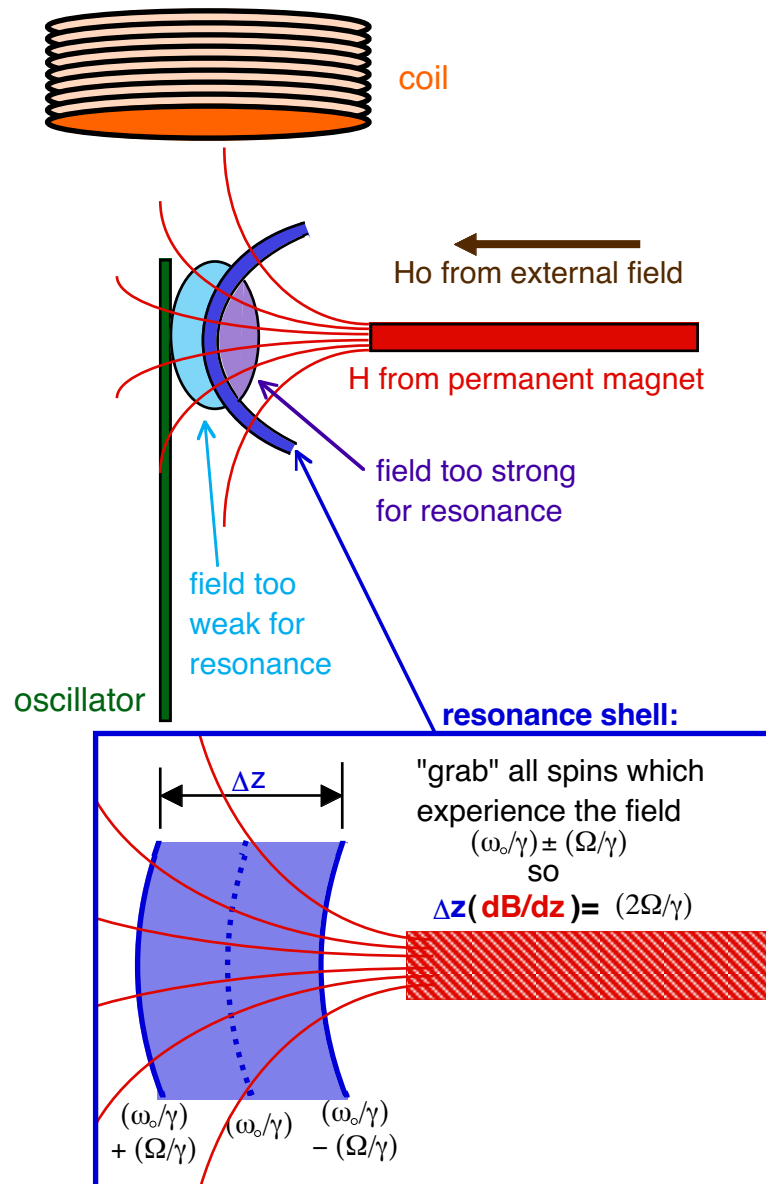
Taking these two effects into consideration, the thickness of the resonance shell,  $\Delta z$ , can be estimated by:

$$\Delta z = \frac{2\Omega/\gamma}{dB/dz}. \quad (2.14)$$

The detected force is then proportional to the number of spins,  $N$ , contained in the resonance shell [21]:

$$F(z) = \left( N \frac{\gamma^2 I(I+1)}{3k_B T} H_{total} \right) \frac{dB}{dz}. \quad (2.15)$$

Figure 2.5: Illustration of the resonance slice created by the permanent magnet.



Thus, to get an accurate prediction for  $N$  and therefore for the expected magnetization, it is not only important to know the value of the field gradient, but also to understand the effect that the amplitude of the cyclic adiabatic inversion and the strength of the rf field are having on the detected signal.

### 2.1.5 SENSITIVITY COMPARISON

Shortly after the method of NMRFM was thought of, a comprehensive analysis was done by Sidles which compared the sensitivity of MRFM to that of conventional inductive magnetic resonance detection [22]. It was shown that both systems can be described by three parameters. The first two parameters are the resonant frequency and quality factor of the oscillator (either the pickup coil or the mechanical oscillator). The other parameter is less intuitive, and is referred to as the magnetic stiffness,  $k_{mag}$ . Physically, this parameter describes how much energy the oscillator requires to generate an oscillating magnetic field at the sample. In order to calculate this parameter for each method, relationships were found which put  $k_{mag}$  in terms of known quantities. For the inductive detection method, it was found that this parameter depends mainly on the volume of the pickup coil, and can be written (SI units):

$$k_{mag} \approx \frac{2V_{coil}}{\mu_o}, \quad (2.16)$$

For the mechanical oscillator,  $k_{mag}$  is given by:

$$k_{mag} = \frac{k_{mech}}{(dB/dz)^2}, \quad (2.17)$$

where  $k_{mech}$  is the mechanical spring constant of the oscillator.

These three parameters allow for the comparison of the two methods by making them equivalent to a fluctuating magnetic moment with a spectral density

$S_\mu$ :

$$S_\mu = \frac{4k_B T k_{mag}}{Q\omega_{osc}}. \quad (2.18)$$

The force sensitivity achievable through this process is ultimately limited by the Brownian motion of the mechanical oscillator, given in  $\text{N}/\sqrt{\text{Hz}}$  by:

$$F_{min} = \sqrt{\frac{4k_B T k_{mech}}{Q\omega}}. \quad (2.19)$$

Using typical values for each system, it was estimated that single spin detection is theoretically possible with MRFM.

## 2.2 SPECIFIC EXPERIMENTAL CONCERNS

As previously mentioned, there are some fundamental experimental concerns that still require extensive investigation. This work considers these in detail in order to aid in the analysis of future measurements.

### 2.2.1 THE IDEAL SIGNAL

Before discussing potential problems, it is first necessary to explain what type of signal would be expected from an ideal experiment. Once a clear understanding of this has been achieved, then each possible deviation can be investigated separately. Here, *ideal* refers to the case where the adiabatic condition is met and where there are no relaxation effects. Figure 2.6 shows an example of a curve which may be expected for the ideal case. The measured amplitude is directly related to the measured force through equation 2.7. Due to the complexity of equation 2.13, the maximum force exerted on the oscillator *is not necessarily equal to*  $M_o \frac{dB}{dz}$ , even in the ideal case. Instead, for a given initial value of the magnetization, the maximum force exerted in the  $z$  direction depends on the modulation parameter  $\Omega/\gamma H_1$ , as was plotted in Figure 2.4.<sup>5</sup> By knowing the initial conditions, the expected maximum force

---

<sup>5</sup>Again, it is important to note that the first component of the Fourier expansion must be found in order to exactly determine the value of the maximum expected magnetization in the  $z$  direction



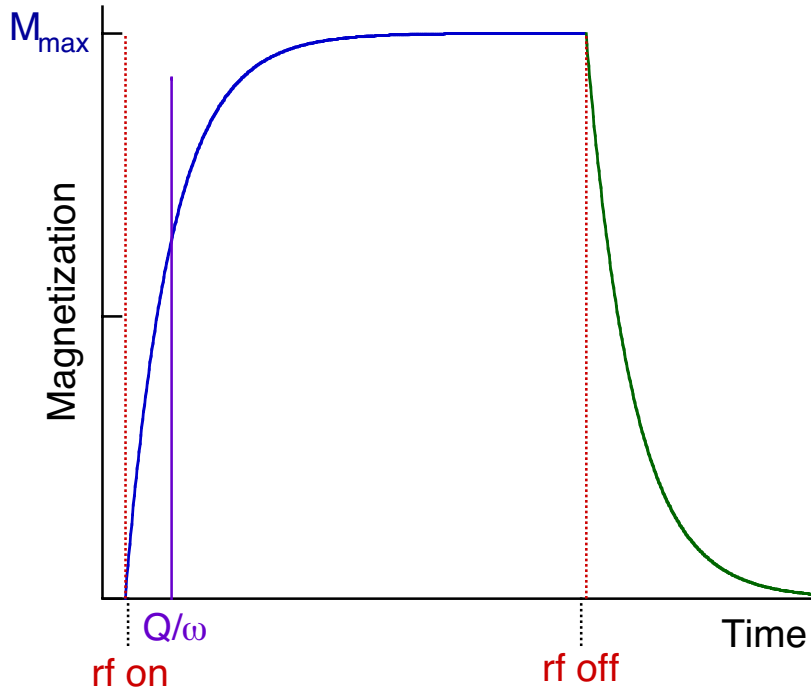


Figure 2.6: Example of a signal which is expected in an ideal experiment.

can be calculated. In this section the predicted maximum force value will simply be referred to as  $F_{max}$  (corresponding to an amplitude  $A_{max}$  and a magnetization  $M_{max}$ ). The equilibrium magnetization,  $M_o$ , can then be calculated by knowing the exact parameters used for the modulation.

When the rf modulation is applied, the mechanical oscillator will *ring up* to its maximum amplitude with a time constant  $\tau = Q/\omega_{osc}$ .<sup>6</sup> After some time larger than  $\tau$ , the oscillator will have reached a maximum amplitude given by equation 2.7. This oscillation will continue indefinitely until the rf modulation (and therefore the applied force) is turned off. At this point, the oscillator's amplitude will decay with

---

*which is acting on the oscillator at its resonant frequency.*

<sup>6</sup>This is one disadvantage of having an extremely high Q. This time taken for the maximum signal to be reached increases with the Q, and therefore for experiments in which short time scales are important, it may be worthwhile to use active feedback to effectively decrease the Q [17].

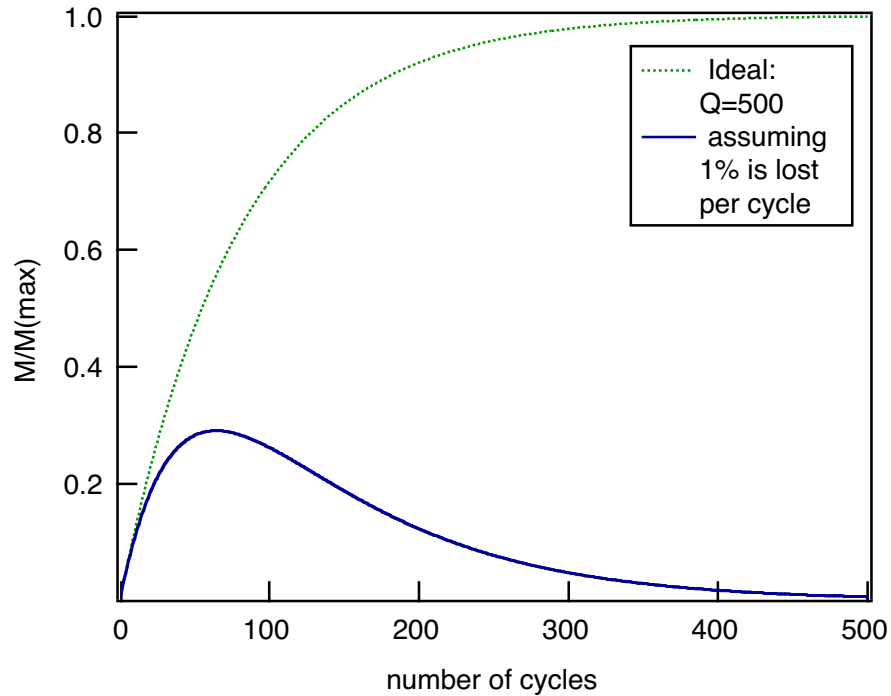


Figure 2.7: Example of an expected signal when non-adiabatic effects are included (assuming no relaxation during inversion).

the same time constant  $\tau$ . Therefore, one rf signal will result in a curve such as Figure 2.6.  $M_{max}$  can then be extracted easily and accurately. The position of the resonance shell can then be moved, and the entire sample can be scanned.

### 2.2.2 NON-ADIABATIC EFFECTS

In order for the ideal case to occur, the adiabatic condition must be met. Thus far, there has been little to no research done which investigates this important condition. This work will consider non-adiabatic effects in detail and will attempt to devise a way to probe the limits of the adiabatic condition. It is assumed that relaxation effects can still be neglected. This is a reasonable assumption because samples can be chosen that have long, and therefore negligible, relaxation times.

Figure 2.7 illustrates a curve that may result if the adiabatic condition is not

met. The dotted line represents the ideal signal. The solid line shows a possible non-adiabatic effect on the signal. To model this effect, it has been assumed that a fixed percentage of the spins are lost per cycle. This seems to be a reasonable assumption because the cycle parameters are not changing and therefore the same fraction of spins,  $p$ , should be lost for all cycles.<sup>7</sup> The total magnetization contributing to the observed signal can then be written as a function of the number of cycles,  $n$ :

$$M(n) = M_{max} \left( 1 - \exp \left[ -\frac{2\pi n}{Q} \right] \right) (1 - p)^n; \quad n = 0, 1, 2... \quad (2.20)$$

The first term is simply the ideal curve, expressed in terms of finite values of  $t = (2\pi n/\omega_{osc})$ . Making the magnetization a function of the discrete number of cycles does not result in any loss of generality since our model assumes many cycles and a high  $Q$ .

The study of this non-adiabatic effect can be approached in different ways. For the present work, the resonant frequency of the mechanical oscillator, and therefore the speed at which the effective field is modulated, is relatively non-variable. Thus, the other half of the adiabatic condition, the speed at which the moments precess about the effective field, must be varied. This precession has a minimum value of  $\gamma H_1$  (assuming that  $\Omega/\gamma > H_1$ ). By increasing the rf field  $H_1$  the adiabatic condition will be approached. The different signals can be measured for each value, and simple fits of the data can estimate the percentage lost as a function of  $H_1$ .

However, the previous expression for the adiabatic condition is not in its exact form. The speed at which the spins precess about the effective field does indeed have a minimum value of  $\gamma H_1$ , but the angular velocity of the effective field is *not* equal to  $\omega_{osc}$ . From Figure 2.3:

---

<sup>7</sup>It must also be considered that some spins are possibly “gained” during each cycle as the effective field grabs them. Therefore the total percentage lost will most likely be small.

$$\tan \phi = \frac{\Omega \sin \omega_{osc} t}{\gamma H_1}, \quad (2.21)$$

where  $\phi \equiv (\frac{\pi}{2} - \theta)$ . Therefore the angular velocity can be expressed by:

$$\frac{d\phi}{dt} = \omega_{osc} \left( \frac{\frac{\Omega}{\gamma H_1} \cos \omega_{osc} t}{1 + \left(\frac{\Omega}{\gamma H_1}\right)^2 \sin^2 \omega_{osc} t} \right). \quad (2.22)$$

The relevant value here is the maximum angular velocity that the effective field experiences. This leads to the exact statement of the adiabatic condition:

$$\gamma H_1 \gg \left. \frac{d\phi}{dt} \right|_{max} = \omega_{osc} \frac{\frac{\Omega}{\gamma H_1}}{1 + \left(\frac{\Omega}{\gamma H_1}\right)^2}. \quad (2.23)$$

Changing  $H_1$  also changes the maximum angular velocity of the effective field, as plotted in Figure 2.8. This needs to be taken into account when analyzing the results. Ideally, an adiabatic limit could be found for the ratio  $\gamma H_1 : d\phi/dt|_{max}$ , which is a function of not only  $H_1$ , but also  $\omega_{osc}$  and the modulation amplitude  $\Omega$ . These parameters can be checked numerically before running an experiment to ensure the adiabatic condition is met.

### 2.2.3 RELAXATION EFFECTS DURING INVERSION

Assuming the adiabatic condition is met as described above, a study needs to be done to determine relaxation effects during inversion. For extremely long relaxation times (relative to  $Q/\omega_{osc}$ ), this effect can be neglected. However, for many samples (especially biological ones) this will not be the case, and this therefore poses a serious potential problem to the method of cyclic adiabatic inversion.

For the following discussion, the relaxation times will be assumed to be long compared to one period of inversion ( $2\pi/\omega_{osc}$ ). This is a reasonable assumption because if it is not met, then the method of cyclic adiabatic inversion will not work

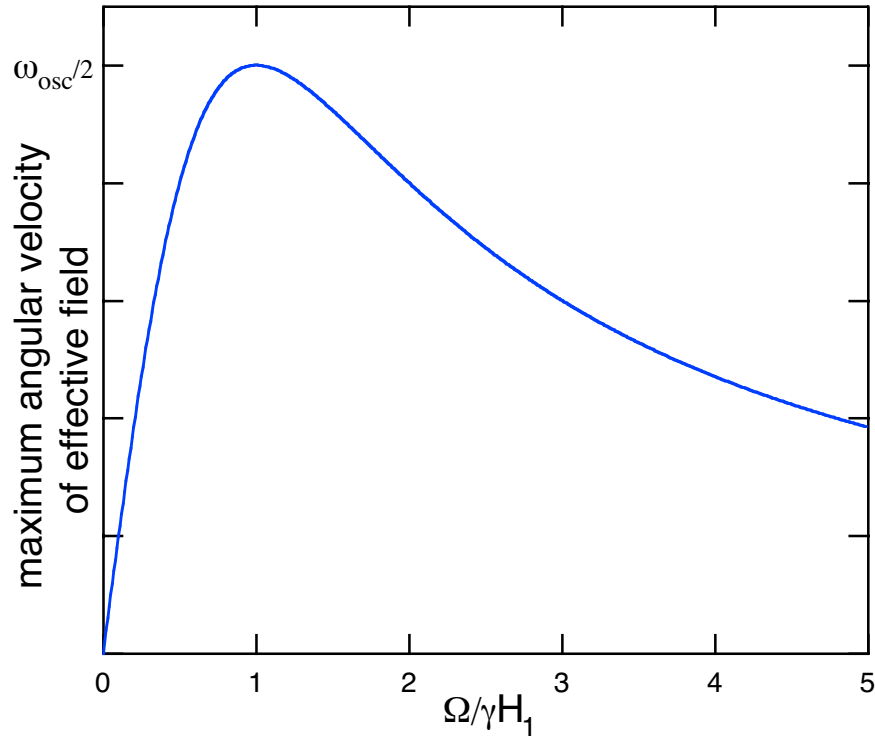


Figure 2.8: Dependence of the maximum angular velocity of the effective field on the modulation parameter  $\Omega/\gamma H_1$ .

due to the decay of the magnetization to a negligibly small value before the oscillator can be rung up.<sup>8</sup> (For such short relaxation times, other methods must be used, such as the inversion-recovery method [12].) Therefore, it is assumed that the magnetization will see one *effective adiabatic inversion relaxation time*, denoted  $T_{AI}$ , which is an average of the different values of the relaxation time during one cycle. If this relaxation effect is taken into account, then the ideal curve is modified by the addition of an exponential decay, as shown in Figure 2.9. It is clear that even relatively long relaxation times compared to the ring-up time of the oscillator result

---

<sup>8</sup>Even if fast recovery times are taken into account, the magnetization will never recover to a measurable value once it decays since the maximum field is only  $\Omega/\gamma$ , which is much smaller than the initial field  $H_o$ .

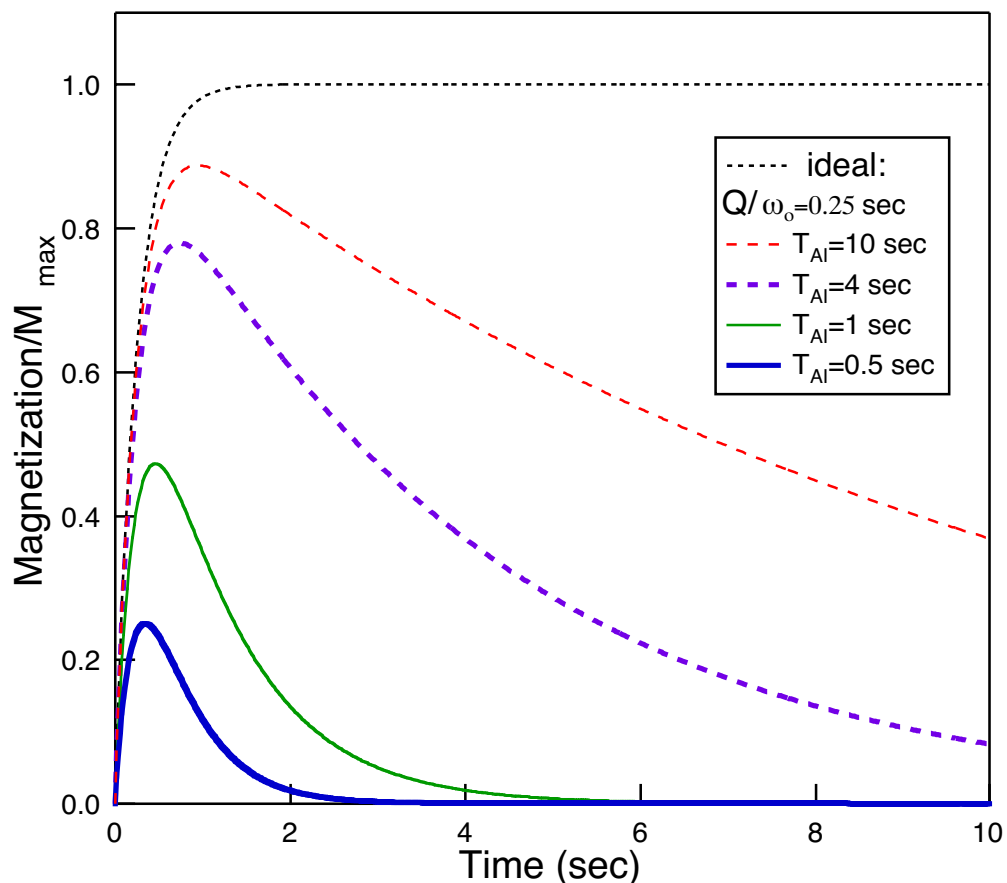


Figure 2.9: Example of an expected signal when relaxation effects during inversions are included (assuming the adiabatic condition is met).

in a significantly decreased observed signal maximum. In fact, for  $T_{AI} = 16Q/\omega$ , the maximum is still decreased by approximately 20 percent. Although obviously detrimental to the overall force sensitivity achievable, this effect may in fact become useful in the future; by measuring  $T_{AI}$ , one may in fact be able to extract some extremely useful dynamical information about the sample, without having to do any tedious pulse-type experiments. But first an expression for  $T_{AI}$  must be found. To do this, some of the fundamental relaxation times in NMR must first be understood [18-20].

The main relaxation mechanism in NMR is the spin-lattice relaxation time  $T_1$ . This is the relaxation in the *lab frame* to the equilibrium value  $M_o$ . If for some reason the magnetization is destroyed, then it will grow back to  $M_o$  with a time constant  $T_1$ . Physically, this is the rate at which energy can be transferred to the lattice when a moment antiparallel to the field jumps to its lower energy state parallel to the field. When this jump occurs, an energy of  $2\mu H_o$  must be absorbed by the lattice. For a spin-1/2 particle undergoing isotropic motion this relaxation rate can be expressed as [23, 24]:

$$\frac{1}{T_1} = \frac{2}{3} \langle \Delta\omega^2 \rangle (J(\omega) + 4J(2\omega)), \quad (2.24)$$

where  $\langle \Delta\omega^2 \rangle$  is the second moment in terms of frequency, and  $J(\omega)$  is the spectral density which can be estimated by:

$$J(\omega) \approx \frac{\tau_c}{1 + \omega^2\tau_c^2}. \quad (2.25)$$

The correlation time,  $\tau_c$ , is a measure of the field fluctuations and increases with decreasing temperature. In the case of relaxation by motion-induced fluctuations of dipole-dipole interactions, it is the time it takes for a molecule to rotate by an angle of one radian. This spectral density function is plotted for various values of  $\tau_c$  in Figure 2.10. Figure 2.11 shows the dependence of the spin-lattice relaxation time on the correlation time for various frequency values, given in terms of the Larmor frequency.

However, spin-lattice relaxation is not directly relevant to the relaxation that will occur during the cyclic adiabatic inversion process. Instead, the relevant relaxation time is the spin-lattice relaxation time in the *rotating frame*,  $T_{1\rho}$ . In the rotating frame, the magnetization only sees the effective field. If the magnetization is manipulated so that it lies parallel to the effective field on resonance ( $= H_1\hat{x}'$ ) then it will decay with a time constant  $T_{1\rho}$  to an equilibrium value with this field,

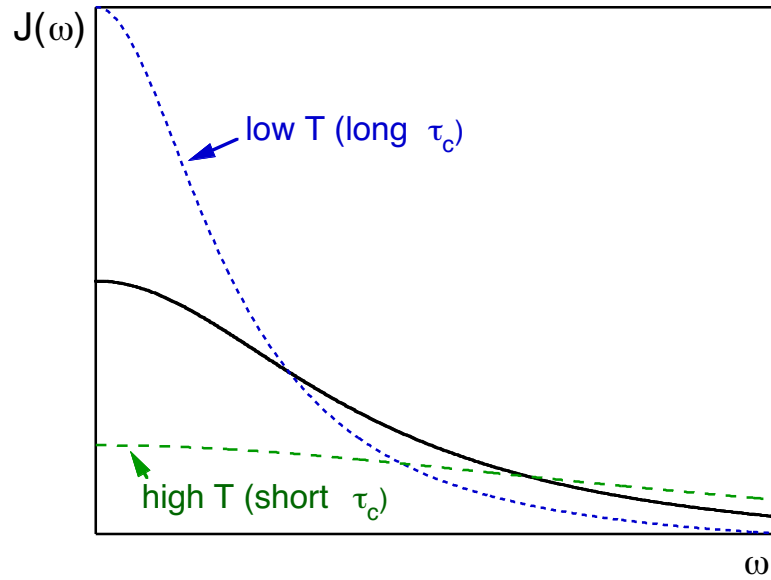


Figure 2.10: Spectral density as a function of frequency for various values of the correlation time.

given by:

$$M = N \frac{\gamma^2 I(I+1)}{3k_B T} H_1. \quad (2.26)$$

At first glance, it may seem that  $T_{1\rho}$  should be the same as  $T_1$ . This is not the case because the effective Larmor frequency is different in the two frames. The relaxation rate for a given static field is most affected by fluctuations occurring at the Larmor frequency about that field, and  $\gamma H_1 \ll \gamma H_o$ . If  $T_1$  is measured at extremely low fields then it should approach the measured values of  $T_{1\rho}$ . However, lowering the field significantly reduces the sensitivity. Therefore, measuring  $T_{1\rho}$  allows for the investigation of relaxation rates in the low field regime without losing sensitivity.

An expression for  $T_{1\rho}$  in terms of the applicable spectral densities can be



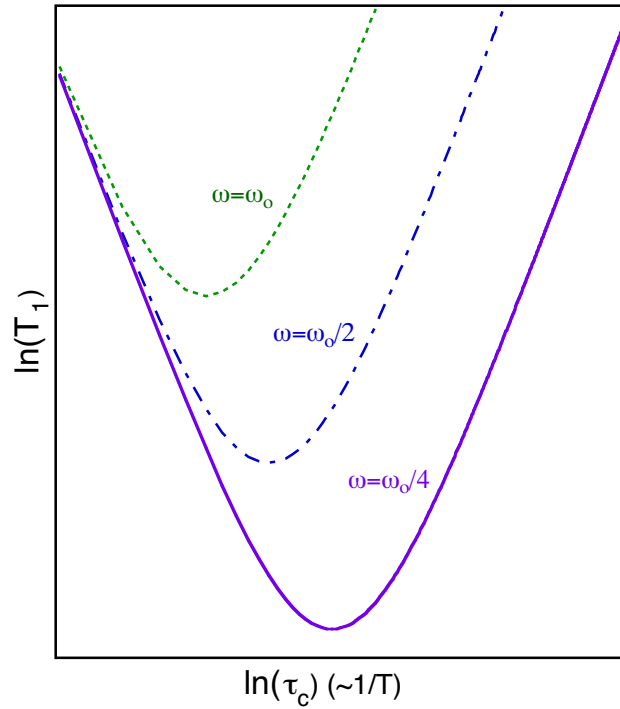


Figure 2.11: Dependence of the spin-lattice relaxation rate on temperature for different frequencies (fields).

written [25]:

$$\frac{1}{T_{1\rho}} = \frac{1}{10} \left( \frac{\mu_o \gamma^2 \hbar}{4\pi r^3} \right)^2 \left[ 3J(2\omega_o) + \frac{9}{2}J(\omega_o) + \frac{5}{2}J(2\omega_1) \right],^9 \quad (2.27)$$

where  $r$  is the interatomic distance,  $\omega_o$  is the Larmor frequency in the lab frame, and  $\omega_1$  is the Larmor frequency in the rotating frame. It is important to note that this expression was derived assuming that the effective field in the rotating frame was static and equal to its resonance value. Therefore it does not completely account for all effects which may occur during the cyclic adiabatic inversion process.

During cyclic adiabatic inversion, the magnetization is exposed to a moving effective field in the rotating frame. Recall that the value of the effective field has

<sup>9</sup>For  $^1\text{H}$  this =  $\frac{1}{r^6} 28.4654 \times 10^9 [3J(2\omega_o) + \frac{9}{2}J(\omega_o) + \frac{5}{2}J(2\omega_1)]$ , where here  $r$  is in units of Angstroms.

a maximum value of  $\sqrt{(\Omega/\gamma)^2 + H_1^2}$ , which is significantly lower than the external field  $H_o$  and closer in magnitude to  $H_1$ . Also, it was assumed that the relaxation rate during inversion is much greater than the time it takes for one inversion cycle ( $= 1/\omega_{osc}$ ). Physically, this assumption means that the magnetization sees an average value for the magnitude of the effective field during inversion, given by:

$$\langle |H_{eff}| \rangle = \frac{\omega_{osc}}{\pi} \int_0^{\pi/\omega_{osc}} \left[ \left( \frac{\Omega}{\gamma} \sin \omega_{osc} t \right)^2 + H_1^2 \right]^{1/2} dt. \quad (2.28)$$

Thus, a reasonable approximation of the relaxation time during inversion can be written using this value for the effective field instead of the resonance value  $H_1$ . Equations 2.25 and 2.27 yield:

$$\frac{1}{T_{AI}} = \frac{1}{10} \left( \frac{\mu_o \gamma^2 \hbar}{4\pi r^3} \right)^2 \left[ \frac{6\tau_c}{1 + 4\gamma^2 H_o^2 \tau_c^2} + \frac{9\tau_c}{1 + \gamma^2 H_o^2 \tau_c^2} + \frac{5\tau_c}{1 + 4\gamma^2 \langle |H_{eff}| \rangle^2 \tau_c^2} \right]^{10}. \quad (2.29)$$

It may however be the case that the relaxation behavior can be better estimated by averaging the *rate* over one cycle, which is different than the rate caused by the average field. The expression for the adiabatic relaxation time in this scenario can be written:

$$\begin{aligned} \langle \frac{1}{T_{AI}} \rangle = & \frac{1}{10} \left( \frac{\mu_o \gamma^2 \hbar}{4\pi r^3} \right)^2 \left[ \frac{6\tau_c}{1 + 4\gamma^2 H_o^2 \tau_c^2} + \frac{9\tau_c}{1 + \gamma^2 H_o^2 \tau_c^2} \right. \\ & \left. + \frac{\omega_{osc}}{\pi} \int_0^{\pi/\omega_{osc}} \left( \frac{5\tau_c}{1 + 4\gamma^2 \left( \frac{\Omega^2}{\gamma^2} \sin^2(\omega_{osc} t) + H_1^2 \right) \tau_c^2} \right) dt \right]. \end{aligned} \quad (2.30)$$

In either case, if the adiabatic condition has been met, the decay of the observed signal can be fit to a simple exponential. This will allow for an extrapolation of both  $M_o$  and  $T_{AI}$ .

---

<sup>10</sup>Since  $H_{eff} \ll H_o$ , equation 2.30 can be written:  $\frac{1}{T_{AI}} = \frac{1}{10} \left( \frac{\mu_o \gamma^2 \hbar}{4\pi r^3} \right)^2 \frac{\tau_c}{4 + 16\gamma^2 \langle |H_{eff}| \rangle^2 \tau_c^2}$ , eliminating the dependence on  $H_o$ .

### 2.2.4 MEASURING RELAXATION TIMES

One main application of conventional NMR is the measurement of relaxation times. It is obviously desirable to acquire the ability to make these measurements using NMRFM. Potential schemes for performing these measurements are given in this section. They all rely on pulse techniques (as described in Section 2.1.1) and assume that an accurate value of  $M_o$  can be found using cyclic adiabatic inversion in accordance with the considerations mentioned above.

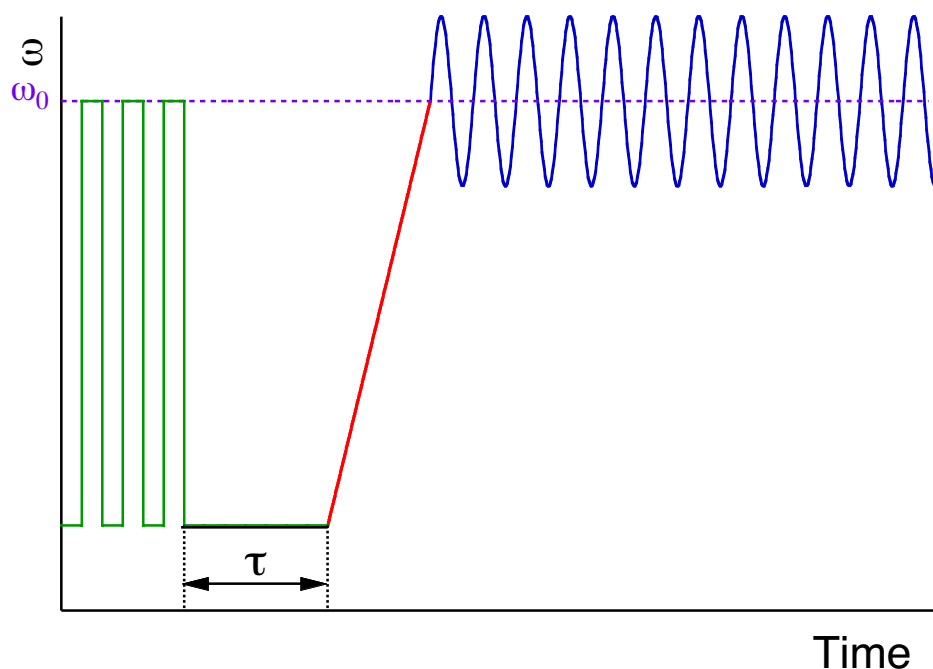


Figure 2.12: Frequency modulation which can be used to measure the spin-lattice relaxation rate.

A method for measuring  $T_1$  is depicted in Figure 2.12. First, the magnetization, which has an initial value of  $M_o$ , is destroyed using a saturation comb of  $\pi/2$  pulses. After this step the magnetization is assumed to be zero. At this point the rf frequency is moved far off resonance allowing the magnetization to recover. After some variable time  $\tau$ , the frequency is ramped back up to resonance so that the

magnetization follows it. The cyclic adiabatic inversion sequence is then started.<sup>11</sup> This is repeated for different recovery times, and the resulting  $M(\tau)$  curve can be fit to:

$$M(\tau) = M_o \left( 1 - \exp \frac{-\tau}{T_1} \right), \quad (2.31)$$

giving a direct measurement of  $T_1$ .

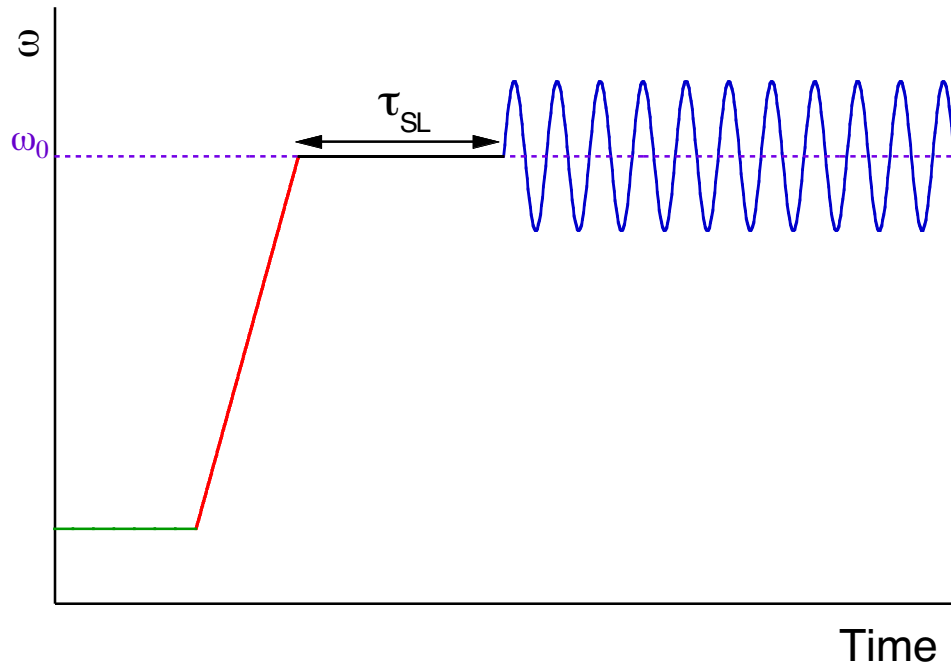


Figure 2.13: Frequency modulation which can be used to measure the spin-lattice relaxation in the rotating frame.

A method has also been devised for the measurement of the spin-lattice relaxation time in the rotating frame,  $T_{1\rho}$ . Due to its relevance to the relaxation effects that occur during cyclic adiabatic inversion, measurements of this relaxation rate will be extremely helpful in understanding the inversion process. Figure 2.13 illustrates the sequence that allows for a measurement of  $T_{1\rho}$ . The magnetization is initially

<sup>11</sup>Even if there is some decay during the ramp time, this can be accounted for since it will be a constant offset for all values of  $\tau$ .

equal to  $M_o$ . The frequency is slowly ramped to resonance so that the magnetization follows the effective field. The frequency is then held constant at resonance for some variable time  $\tau$ . The magnetization is spin-locked and will want to decay to its equilibrium value along  $H_1$ . Cyclic adiabatic inversion is then used to make a measurement of the magnetization for a given decay time  $\tau$ . The resulting  $M(\tau)$  curve can be fit to:

$$M(\tau) = M_o \left( \exp \frac{-\tau}{T_{1\rho}} \right), \quad (2.32)$$

giving a measurement of  $T_{1\rho}$ . However, it is important to note that this value of  $T_{1\rho}$  is not exactly equal to that which is measured with conventional NMR. This is due to the fact that many of the moments are spin-locked off resonance. It should be clear that this effect depends on the modulation amplitude  $\Omega/\gamma$ . The value of  $T_{1\rho}$  measured with the above technique can be expressed as [26]:

$$\frac{1}{T_{1\rho}} = \frac{1}{(\Omega/\gamma)^2 + H_1^2} \left( \frac{(\Omega/\gamma)^2}{T_1} + \frac{H_1^2}{T_{1\rho(\text{conv})}} \right), \quad (2.33)$$

where  $T_{1\rho(\text{conv})}$  is the value exactly on resonance, as is measured with conventional inductive techniques. In other words, the measurement of  $T_{1\rho}$  using cyclic adiabatic inversion gives an average value of the relaxation time in the frequency range over which the measurement is taken. Thus as the modulation amplitude is decreased, the measured value of  $T_{1\rho}$  will approach  $T_{1\rho(\text{conv})}$ .

## CHAPTER 3

### MECHANICAL OSCILLATORS

*“Shake down the thunder from the sky...”*

*- Notre Dame University Fight Song*

The sensitivity of a magnetic resonance force microscopy experiment is ultimately limited by the thermal noise of the mechanical oscillator to which the sample is coupled. The controllable parameters of this expression are the quality factor,  $Q$ , the spring constant,  $k$ , and the resonance frequency,  $\omega$ . However, as explained in the previous chapter, the resonance frequency is limited by the adiabatic condition and is currently kept less than 100 kHz. Therefore, to achieve the lowest possible thermal noise, mechanical oscillators need to be fabricated with large  $Q$ 's and low  $k$ 's. This goal has been achieved by implementing a multiple-torsional design [27] as will be described in this chapter. The fabrication process, which uses microelectronic fabrication techniques, will also be discussed here. Finally, characterization results and the predicted force sensitivities will be given for these multiple-torsional oscillators.

#### 3.1 DESIGN

##### 3.1.1 DAMPING MINIMIZATION

Figure 3.1(a) illustrates the simple double torsional design. It is connected at one end to a fixed *base*, with a large *wing* and a smaller *head*. The long skinny pieces

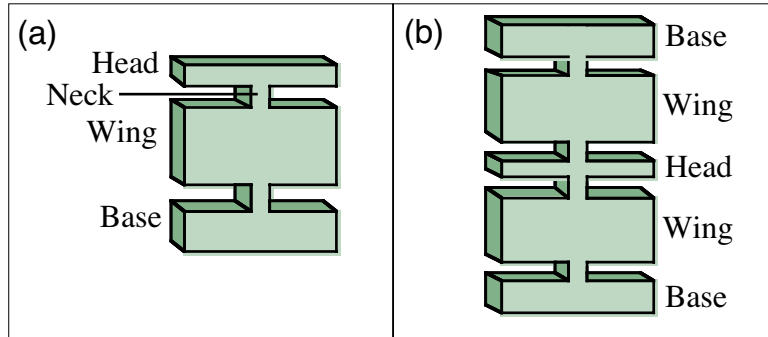


Figure 3.1: Basic geometry of the (a) double torsional and (b) triple torsional designs.

connecting the base, wing, and head are referred to as the *necks*. This design has received quite a bit of attention in recent literature, and finite element modeling has been done to predict many of the possible resonances [28, 29]. For the purposes of this work, only four main resonances will be considered in detail: the lower cantilever mode, in which the head and wing tilt in phase with each other; the upper cantilever mode, in which the head and wing tilt with opposite phases; the lower torsional mode, in which the head and wing twist together; and, finally, the upper torsional mode, in which the head and wing twist opposite each other. The lower modes offer no significant improvement in the  $Q$  over the commercial cantilevers and are therefore just used for characterizing the accuracy of the predicted resonances. However, for the upper modes, most of the energy is stored in the head, which is not directly coupled to the base. For the upper torsional mode, this follows directly from the conservation of angular momentum:

$$I_{head}\omega_{head} = I_{wing}\omega_{wing}, \quad (3.1)$$

where  $I$  is the moment inertia. Using this expression with the equations for the energy of oscillation:

$$E_{head} = \frac{1}{2}I\omega_{head}^2 \quad (3.2)$$

$$E_{wing} = \frac{1}{2}I\omega_{wing}^2, \quad (3.3)$$

the stored energies of oscillation for the upper torsional mode can be related by:

$$E_{head} = \frac{I_{wing}}{I_{head}} E_{wing}. \quad (3.4)$$

Since  $I_{wing}/I_{head} \gg 1$ , most of the energy of oscillation is in the head. Because the head is not directly coupled to the base, damping is minimized.

Likewise, for the upper cantilever mode, conservation of linear momentum,  $m_h v_h = m_w v_w$ , along with the energy expression  $E_{w,h} = \frac{1}{2} m_{w,h} v_{w,h}^2$ , leads to the relation:

$$E_{head} = \frac{m_{wing}}{m_{head}} E_{wing}. \quad (3.5)$$

Triple torsional designs (Fig. 3.1b) have also been fabricated to increase the sturdiness of the oscillators. The final etching process (Section 3.2.5) can cause the double torsional oscillators to bend slightly. The triple torsional design is connected at both ends and avoids this problem while still maintaining the benefits of the upper-torsional mode of operation. Note that for these micro-oscillators which are fixed at both ends, only torsional and “guitar string” modes are relevant, and cantilever modes do not apply.

### 3.1.2 SPRING CONSTANT CONSIDERATIONS

The other main consideration in the design is the desire to have a low spring constant. The spring constant for the torsional modes can be estimated by [30, 31]:

$$\kappa \approx \frac{Gwt^3}{h} \left[ \frac{1}{3} - 0.209 \frac{t}{w} \left( 1 - \frac{1}{12} \left( \frac{t}{w} \right)^4 \right) \right], \quad (3.6)$$

where  $G$  is the shear modulus,  $t$  is the thickness of the oscillator, and  $w$  and  $h$  are the width and the height, respectively, of the neck.

This torsional spring constant translates to a measured force through an effective spring constant, defined as:

$$k_{eff} = \frac{\kappa}{r^2}, \quad (3.7)$$



where  $r$  is the distance that the spins in the sample are from the axis of rotation.<sup>1</sup>

The spring constant for the cantilever modes is given by [32]:

$$k = \frac{Et^3w}{4h^3}, \quad (3.8)$$

where  $E$  is the Young's modulus of elasticity.

From equations 3.6 and 3.8, it is clear that both the torsional and cantilever spring constants will be decreased by decreasing the size (and therefore the thickness) of the oscillators. However, the size and thickness can not be decreased too much due to practical limitations; samples (or magnets) need to be mounted onto the oscillators, so they must be large enough so that their resonances will not be greatly affected by the extra weight. They must also be sturdy enough to withstand the mounting process. For this reason, the multiple-torsional design is much more appropriate for the current work than the simple solution of fabricating thinner AFM-type cantilevers, as has been successfully done with force sensitivities as low as  $5.6 \times 10^{-18} \text{N/Hz}^{1/2}$  [33].

### 3.1.3 ESTIMATED RESONANT FREQUENCIES

The resonant frequencies of each design were calculated before processing efforts began. This was done by assuming a classical harmonic system with the parameters indicated in Figure 3.2. For the double torsional design, the equations describing the torsional motion are written:

$$\begin{aligned} I_h \ddot{\theta}_h + k_2 (\theta_h - \theta_{w1}) &= 0 \\ I_{w1} \ddot{\theta}_{w1} + k_1 \theta_{w1} - k_2 (\theta_h - \theta_{w1}) &= 0, \end{aligned} \quad (3.9)$$

and for the triple torsional designs:

$$I_h \ddot{\theta}_h + k_2 (\theta_h - \theta_{w1}) + k_3 (\theta_h - \theta_{w2}) = 0 \quad (3.10)$$

---

<sup>1</sup>The torque exerted on the oscillator ( $= \frac{\theta \kappa}{Q}$ ) is translated to a force ( $= \frac{Ak_{eff}}{Q}$ ) for the measurement. Equation 3.7 follows directly from the small angle approximation  $\theta \approx \tan \theta = \frac{\Delta}{r}$ , where  $\theta$  is the angular amplitude of oscillation.

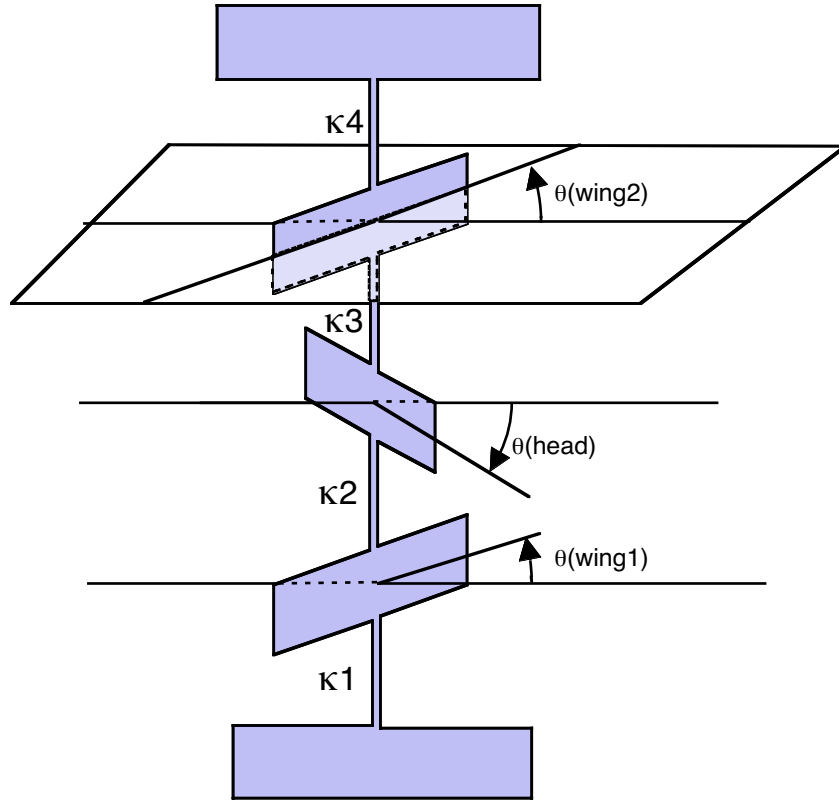


Figure 3.2: Schematic of the parameters used to describe the torsional motion of the triple torsional oscillators. For the double torsional design, the same parameters are used, neglecting the upper wing and the two upper necks.

$$I_{w1}\ddot{\theta}_{w1} + k_1\theta_{w1} - k_2(\theta_h - \theta_{w1}) = 0,$$

$$I_{w2}\ddot{\theta}_{w2} + k_4\theta_{w2} - k_3(\theta_h - \theta_{w2}) = 0,$$

where  $\theta_j = A_j e^{-i\omega t}$ . The cantilever modes are analogous to the torsional ones above, with  $I \rightarrow m$  and  $\theta \rightarrow x$ . Simple diagonalization results in the expressions for the torsional resonant frequencies dependent upon the torsional spring constant and moments of inertia. Likewise, the cantilever resonances are in terms of the spring constant and the masses. All of these can be calculated from the known dimensions as well as the properties of silicon (Appendix A). Thus the normal mode frequencies can be solved numerically. An Excel spreadsheet has been made for this, and a

sample is given in Figure 3.3.

The current dimensions have been chosen taking into consideration the desire for a low spring constants, the need for sturdy designs, and the frequency limit of  $< 100$  kHz. The oscillators have been made with approximately the dimensions shown in Figure 3.4.

## 3.2 FABRICATION OF BORON-DOPED SILICON OSCILLATORS

The process used to fabricate boron-doped silicon oscillators is depicted in the flow chart of Figure 3.5. Single crystal silicon 4" (100) wafers with 7500Å of pre-grown oxide on them are currently used. The important steps in the fabrication process are detailed below. The photolithography steps and the reactive ion etching are done at Pickle Research Center; the remaining steps are done in the Markert Lab unless otherwise specified.

### 3.2.1 MASK CREATION

The first step in the processing is the generation of a mask with the desired pattern. Various mask patterns have been made, but much of the work discussed here results from the mask pattern shown in Figure 3.6. Various methods can be used to make the initial mask. For most of the oscillators discussed here, the procedure outlined in Figure 3.7 was used to make the initial mask. The pattern is first drawn on a computer with 100 times magnification to avoid limitations due to poor printer quality. Then the pattern is photo-reduced to its final 1 cm<sup>2</sup> size. The negative is then used to expose a blank glass mask with a metallic film on it using a positive photoresist. The pattern is exposed approximately 40 times onto one mask so that each 4" wafer results in 40 individual chips, each containing approximately 150 oscillators. Once the mask is exposed, it is developed, post-baked, and the metal<sup>2</sup> is etched away. The

---

<sup>2</sup>The metal is either iron oxide or chrome, and both metal etchants are readily available in the lab.

<b><i>enter dimensions:</i></b>	<i>microns</i>
head width	150
head length	50
wing width	150
wing length	100
neck width	14
wing-to-base length	40
head-to-wing length	30
<b>thickness in meters</b>	4.00E-07

<b><i>silicon information:</i></b>	
<i>G (torsion modulus) (N/m<sup>2</sup>)</i>	6.63E+10
<i>E (Young's modulus) (N/m<sup>2</sup>)</i>	1.00E+11
<i>density (kg/m<sup>3</sup>)</i>	2.33E+03
<b><i>calculation results</i></b>	
<i>head I (N-m<sup>2</sup>)</i>	1.46E-20
<i>wing I (N-m<sup>2</sup>)</i>	3.79E-20
<i>head mass (kg)</i>	6.99E-12
<i>wing mass (kg)</i>	1.40E-11
<i>torsional k; wing-base (N m)</i>	4.95E-10
<i>torsional k; head-wing (N m)</i>	6.60E-10
<i>bending k; wing-base (N/m)</i>	3.50E-01
<i>bending k; head-wing (N/m)</i>	8.30E-01
<b><i>frequencies:</i></b>	
for double-torsional	kHz
<b><i>lower cantilever</i></b>	<b>14.97</b>
<b><i>upper cantilever</i></b>	<b>41.19</b>
<b><i>lower torsional</i></b>	<b>20.05</b>
<b><i>upper torsional</i></b>	<b>68.86</b>
for symmetric triple-torsional	
<b><i>lower cantilever</i></b>	<b>16.49</b>
<b><i>upper cantilever</i></b>	<b>52.89</b>
<b><i>lower torsional</i></b>	<b>22.32</b>
<b><i>upper torsional</i></b>	<b>87.48</b>

Figure 3.3: Example of the spreadsheet created for the calculation of the various resonance frequencies for given oscillator dimensions.

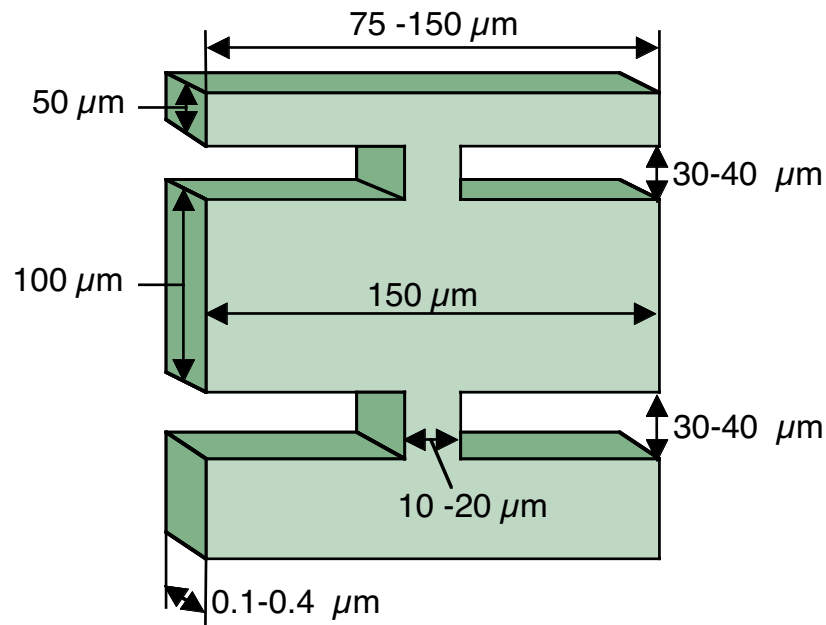


Figure 3.4: Typical dimensions of successfully fabricated and characterized oscillators.

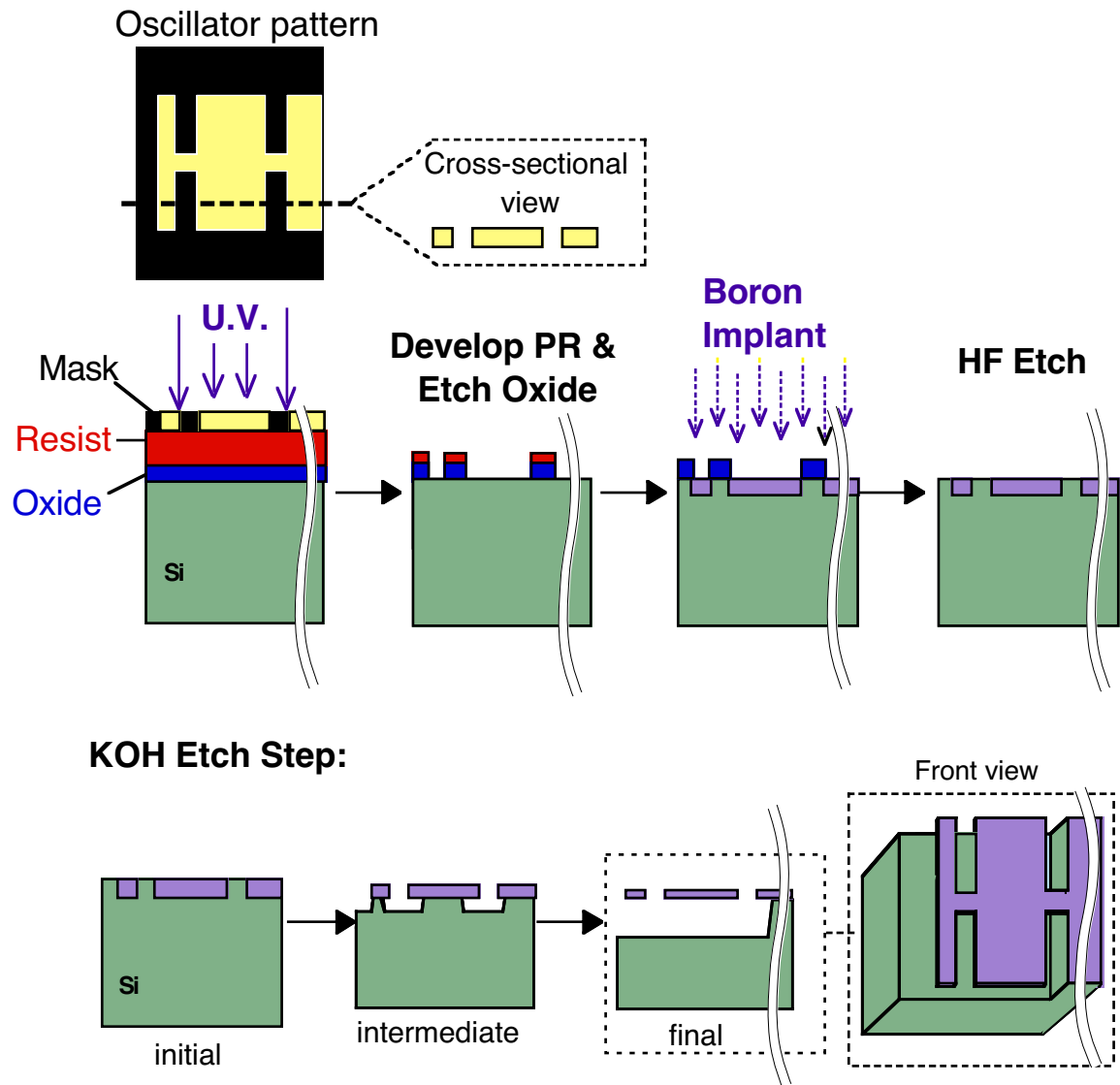
mask is then ready for use.

In the future, it is recommended that this step be simplified by using the technology now offered by some industries which will take a computer drawing and translate it directly onto a glass mask. This method not only will be less tedious, but will also result in greater resolution. This will be increasingly important as the oscillator dimensions get smaller.

### 3.2.2 WAFER PATTERNING

The mask is used to expose the silicon wafer with a positive photoresist on it. The wafers are first coated in a primer, and then the photoresist is spun on. This is done for 30 seconds at 3000 rpm. Other times and rates were used, but the resulting thickness of the photoresist remains approximately constant, determined by the type of resist used. After the resist is spun on, the wafer is pre-baked at 90°C for one

Figure 3.5: Outline of the process used to fabricate the oscillators.



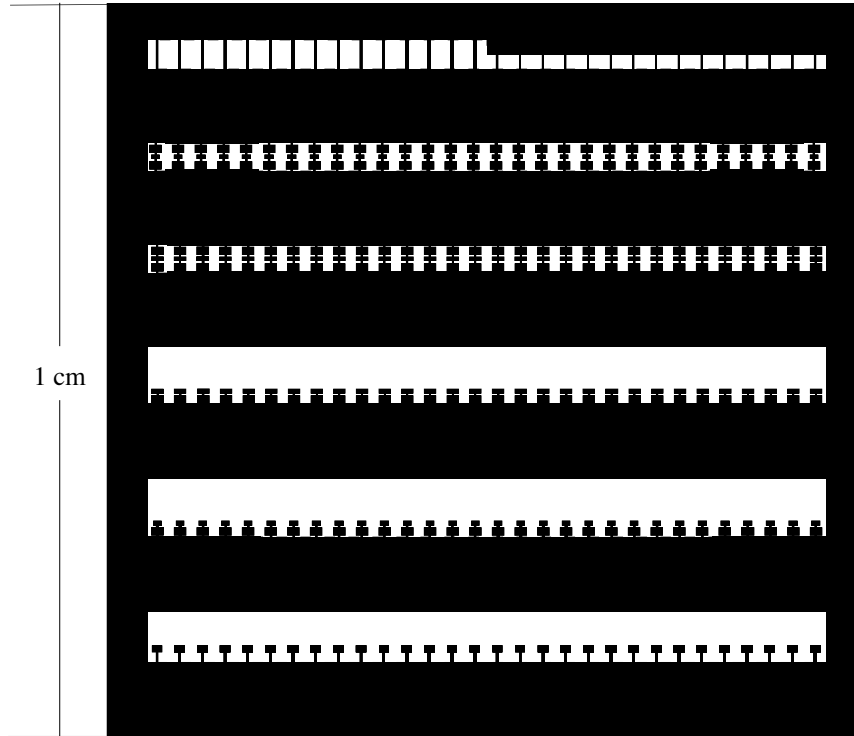
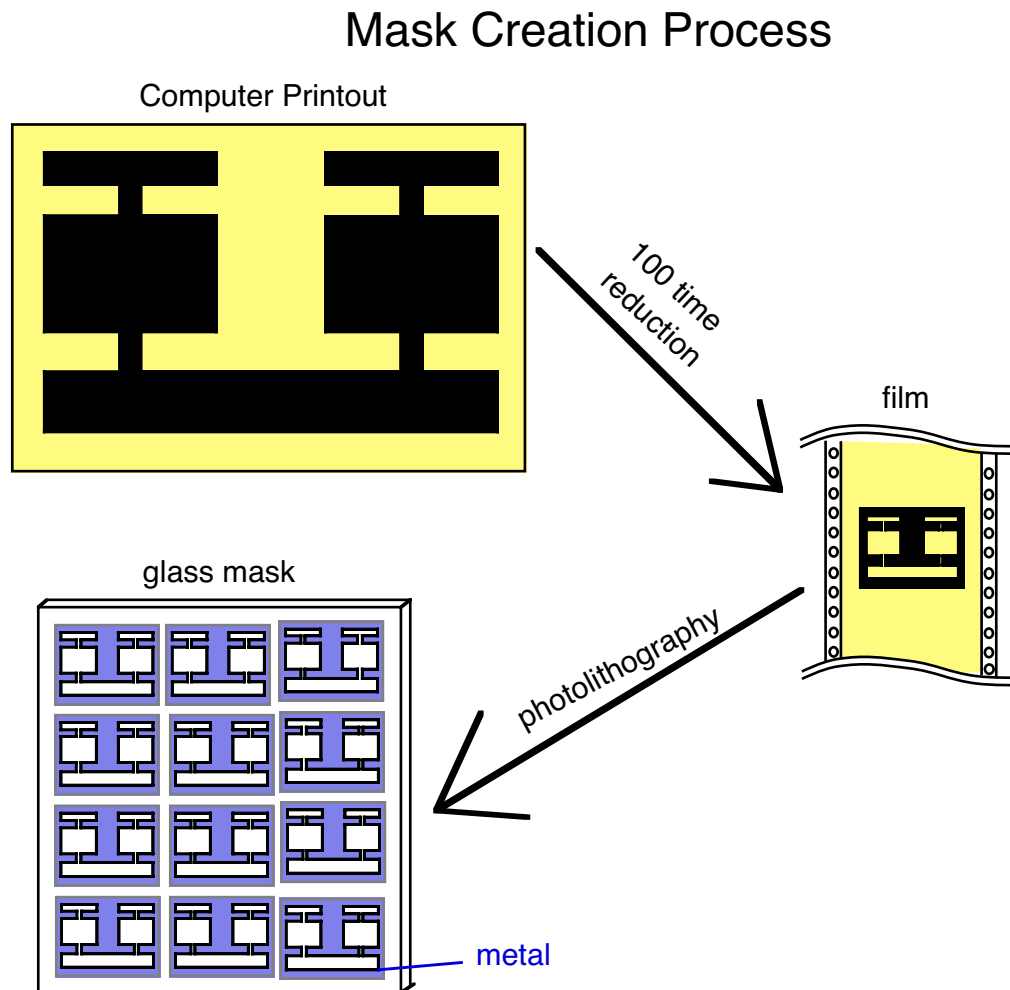


Figure 3.6: Example of a mask pattern which has been used.

minute.

Only one type of photoresist (AZ5209E) is allowed into the silicon bay at Pickle, so the processing is limited by this. It has been found that using two layers of photoresist works best when later using the reactive ion etch to etch away 750 nm of oxide. To apply two layers, simply spin on another layer after pre-baking the first coat, then repeat the pre-bake. There will be an obvious discoloration indicating that the photoresist is not of uniform thickness over the wafer. For the mask pattern shown in Figure 3.6, in which the smallest dimension is 10  $\mu\text{m}$ , this effect has not proven detrimental since the exposure and developing times are relatively flexible. However, for smaller oscillators, these parameters will become more important, and a more uniform photoresist may be desired. If this becomes the case, it is recommended

Figure 3.7: Outline of the mask-making process used to make the oscillators shown in Figure 3.6.





that the photolithography steps be performed at Xidex Corporation, where a thicker photoresist may be used.

Once the photoresist is applied, the wafer and the mask are put into the aligner.<sup>3</sup> The alignment of the mask with respect to the wafer flat has varied to study effects of anisotropic etching. One configuration aligns the base of the oscillators parallel to the wafer (110) flat. In the other, the base of the oscillators are at 45° to the (110) plane. The reasons for this will become evident in Section 3.2.5.

The wafers are exposed for approximately 15 seconds to UV light. They are then developed for approximately 45 seconds, rinsed thoroughly in water, examined under the microscope, and post-baked for one minute at 120°C. They can now be taken out of the lithography bay.

### 3.2.3 OXIDE ETCH

At this point, the photoresist has been removed from the area where the oscillators will be. The 750 nm of oxide is uncovered in these regions. The rest of the wafer is protected by the layer(s) of photoresist. An oxygen and freon plasma is then used to etch away the exposed oxide.<sup>4</sup> The etch rate of the plasma used was found to be approximately 50 nm/min. Initially the oxide is a dark green color; as the wafer etches, the color changes depending on the thickness of oxide remaining [34]. Typical colors which are observed at different etch times all are given in Table 3.1. The oxide is completely removed when the exposed areas look silver. However, anything less than 100 nm is sufficient, and many times a judgement call needs to be made in order to make sure the photoresist which is blocking the etch on the rest of the wafer does not get completely removed.

This reactive ion etch etches photoresist, pure silicon, oxide, and nitride

---

<sup>3</sup>Specific direction for the use of this machine are given in the cleanroom notebook.

<sup>4</sup>A buffered oxide etch was also tried in replacement of the reactive ion etch. It was found that the undercutting is most likely too significant because wafers fabricated in this manner never produced any working oscillators.

Table 3.1: Colors of Oxide During RIE

RIE time	Oxide Color	estimated oxide thickness
0 min	green	750 nm
3 min	dark pink	600 nm
5 min	bright green	500 nm
7 min	yellow-green	400 nm
9 min	blue-ish	300 nm
11 min	metallic light green-yellow	200 nm
12.5 min	blue	150 nm
13.25 min	darker blue/brown	100 nm
14 min	brownish	<100 nm
15 min	all silver(DONE!)	0 nm

at approximately the same rate (within an order of magnitude). Therefore, the protective photoresist layer is extremely crucial to this step. If it is too thin (when just one coat is used) then it gets completely etched away before the 750 nm of oxide does. If this happens, in order to completely expose the silicon where the oscillators will be, some of the 750 nm of oxide on the rest of the wafer must be sacrificed. But then the remaining oxide is no longer thick enough to block the boron implantation (Section 3.2.4) in the desired areas, and the entire process must be repeated with a new wafer. To make sure that there is still photoresist on the wafer after the RIE before sending it off to implant, simply look at the color once the wafer has been cleaned in acetone. The acetone will remove all remaining photoresist, causing the wafer to return to the uniform green color it was initially. If it is not uniformly green, then the photoresist was not thick enough and some of the oxide was etched. The wafer is not worth sending off for boron implantation, and the entire process must be started over.

Once a wafer has been produced that is silver in the areas where the oscillators will be and uniformly green over the rest of the wafer, it is ready for the boron

implantation step.

#### 3.2.4 BORON IMPLANT AND ANNEAL

The wafers are sent away to be implanted with boron since the equipment necessary for this step is locally unavailable. The dose and energy of the boron beam are specified, and the wafers are returned within one week. There are many considerations which go into determining the energy and dose to use for a given implant. The energy determines the peak implant depth, as shown in Figure 3.8. Recall there is 750 nm of oxide blocking the boron from the areas where the oscillators will not be. There are two relevant concentration values for boron in silicon: The first is the solid solubility limit of  $6 \times 10^{20} \text{ cm}^{-3}$  [34]. If the boron implant results in concentrations above this, it is expected that many defects will form that are perhaps irreparable in a post-implant anneal. Therefore, it is desirable to keep the concentration below this level. The second concentration value is the KOH etch-stop value of approximately  $1 \times 10^{20} \text{ cm}^{-3}$  [35]. For concentrations above this, the rate of etching is decreased by a factor of 100. Therefore, concentrations above this should not be found past a depth of 750 nm.

Deciding on the implant energy and dose becomes even more complicated when the effects of the post-implant anneal are taken into consideration. The post-implant anneal is necessary to repair implant damage by recrystallizing the boron-doped silicon [36]. The anneal is done in a tube oven at approximately  $1000^\circ\text{C}$  with an argon gas flow. This step broadens the Gaussian profile as shown in Figure 3.9 and is therefore a possible factor in the final thickness of the oscillators. Short anneal times and low temperatures are most desirable to minimize spreading. However, it has been found that a temperature of at least  $975^\circ\text{C}$  is required for at least 30 minutes; if these conditions are not met, the defects destroy the oscillators during the final wet etch (Section 3.2.5). Applying this effect to the implant profiles of potential doses and energies, reasonable values can be chosen. The dose has been varied from  $1 \times 10^{16} \text{ ions/cm}^2$  to  $4.2 \times 10^{16} \text{ ions/cm}^2$ , and the energy has been 100 or 134 keV.

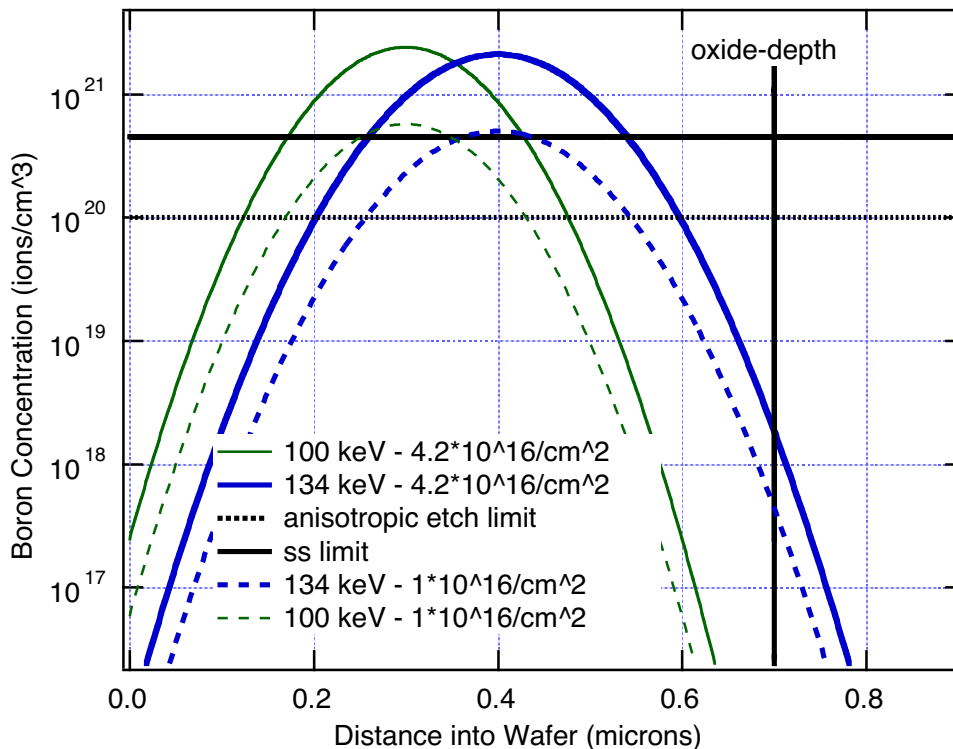


Figure 3.8: Boron concentration profiles as a function of implant energy and dose. The horizontal solid line is the solid solubility limit of boron in silicon. The vertical line indicates the width of the blocking oxide. The dotted horizontal line indicates the concentration necessary to stop the KOH etch.

After the anneal has been completed a buffered HF etch is done to remove the remaining oxide from each chip. This step should take approximately 10 minutes, after which the oscillators should be cleaned and air-dried.

### 3.2.5 FINAL KOH ETCH

The most critical processing step is the final wet-etch. This step is an anisotropic, differential etch using potassium hydroxide (KOH) mixed with water and alcohol [35, 37-41]. KOH is commonly used to etch silicon. The reaction mechanisms have been described in an electrochemical model. The process is an oxidation and reduction, where the reacting species is the HOH/OH<sup>-</sup> in the etching solution. (The potassium

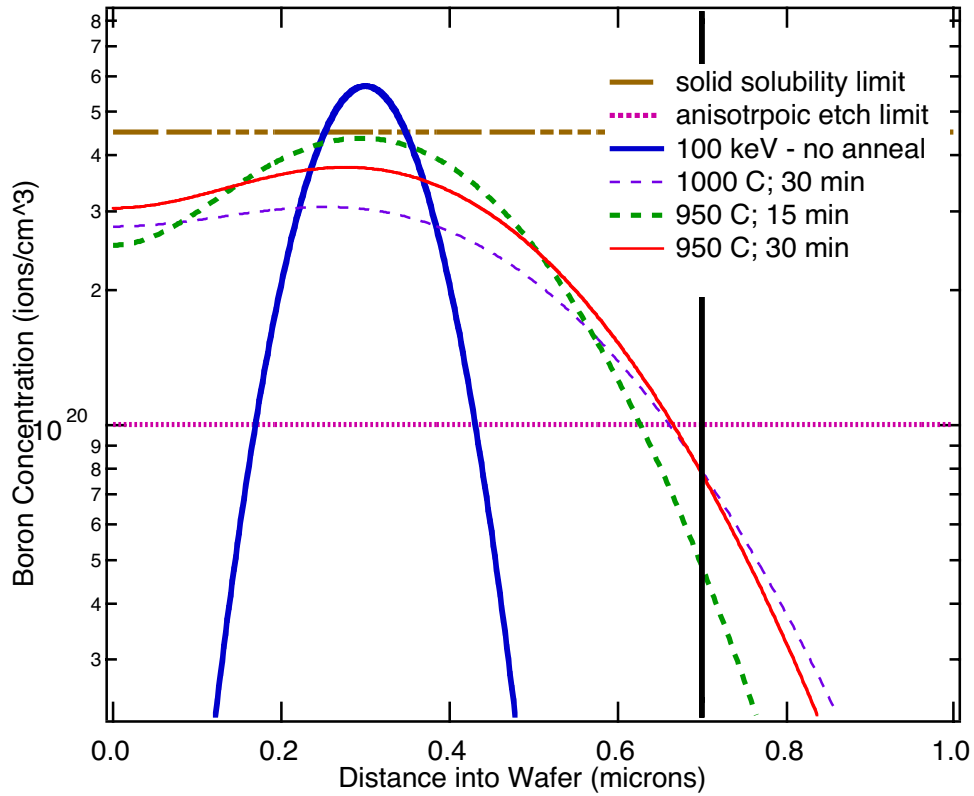
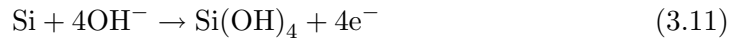


Figure 3.9: Effects of various anneal times and temperatures on the Gaussian profile after implant.

plays no role in the reaction, and in fact solutions such as NaOH have nearly identical etching properties.) First, four  $\text{OH}^-$  ions react with a surface silicon atom:



The  $\text{Si}(\text{OH})_4$  diffuses away, and the four electrons are located in the silicon very close to the surface. These electrons then react with HOH molecules close to the silicon surface, creating one  $\text{H}_2$  molecule and four  $\text{OH}^-$  ions. It is these generated  $\text{OH}^-$  ions which are considered the main reacting species. In fact, the  $\text{OH}^-$  ions in the bulk of the solution experience a repulsive force from the strongly negative silicon surface and do not play a major role in the reaction.

The important characteristic of the KOH solution is the significant reduction of the etch rate for highly hole-doped silicon [35, 41, 38]. This can be understood in a basic model by considering that the four electrons created in the oxidation reaction are more likely to recombine with the readily available holes. Thus the electrons are no longer available for the reduction reaction which creates the crucial  $\text{OH}^-$  ions. The etch rates as a function of boron concentration are illustrated in Figure 3.10 for various concentrations of KOH. Concentrations of KOH higher than 10 percent result in a less distinct transition (as can be seen from the rounding of the transition region) and a slightly higher critical boron concentration. For a solution of 10 percent, a etch selectivity of 100 of the pure silicon to the highly doped silicon takes place for boron concentrations above  $1 \times 10^{20} \text{ cm}^{-3}$ . As the temperature is increased, the etch selectivity does not change significantly. However, it has been found that lower temperatures are significantly easier to work with for two reasons: First, the etch rate is much lower for lower temperatures. (Raising the temperature  $20^\circ\text{C}$  results in approximately a factor of 10 increase in the etch rate) This is beneficial so the etch can be stopped right when the oscillators are done. Second, and more crucial, is the turbulence that occurs in the solution at the higher temperatures. The reactions result in  $\text{H}_2$  bubbles leaving the silicon surface. As the etch rate increases, the bubbles are more numerous in time and tend to be more destructive since the thin oscillators cannot recover between escaping bubbles. Thus room temperature etches are currently performed.

The KOH etching is an extremely anisotropic etch [37, 39, 40], meaning that the etch rate is significantly different for the different crystal directions in silicon. There is an absolute minimum in the etch rate for (111) directions. The etch rate ratio at room temperature is (110):(100):(111) is 160:100:1. Thus the  $\langle 111 \rangle$  planes will form the “walls” of the final etched product. (See Figure 3.11 for an illustration of the planes.) This anisotropy results in varying geometries depending on the initial orientation, as illustrated in Figure 3.12. Although KOH is often used because of its anisotropic results, this fabrication process uses it *in spite* of this reason. Be-

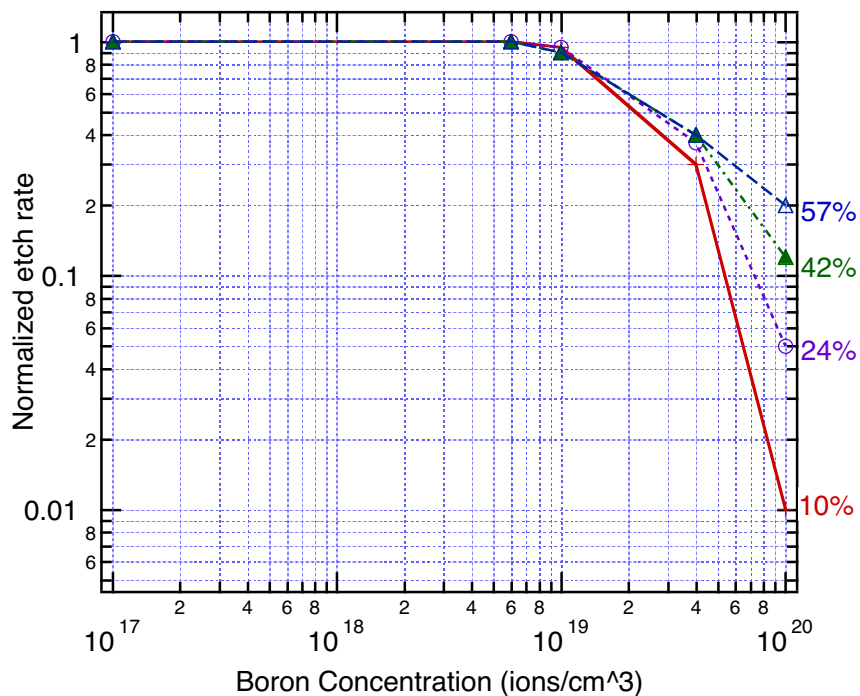


Figure 3.10: KOH etch rates as a function of boron concentration for various KOH concentrations. (Produced using data from [35]).

cause some of the etch must take place along the slower directions, the etch time is significantly increased, leaving more time for the oscillators to gain unwanted defects.

Figure 3.13 gives SEM images of oscillators which have been prepared under identical conditions except for the length of the KOH wet-etch. Figure 3.13(a) is clearly underetched and the oscillators are still attached at the bottom neck. The slow etch direction in the (111) direction is the cause of this underetching. Figure 3.13(b) shows triple torsional oscillators which have been taken out of the etch at the perfect time. They are not attached to the substrate below them yet have not been left in the etch any longer than necessary. Figure 3.13(c) is an example of over-etched triple torsional oscillators. The substrate beneath the oscillators is much flatter than that of Figure 3.13(b), indicating that the oscillators were subjected to the KOH longer than necessary.

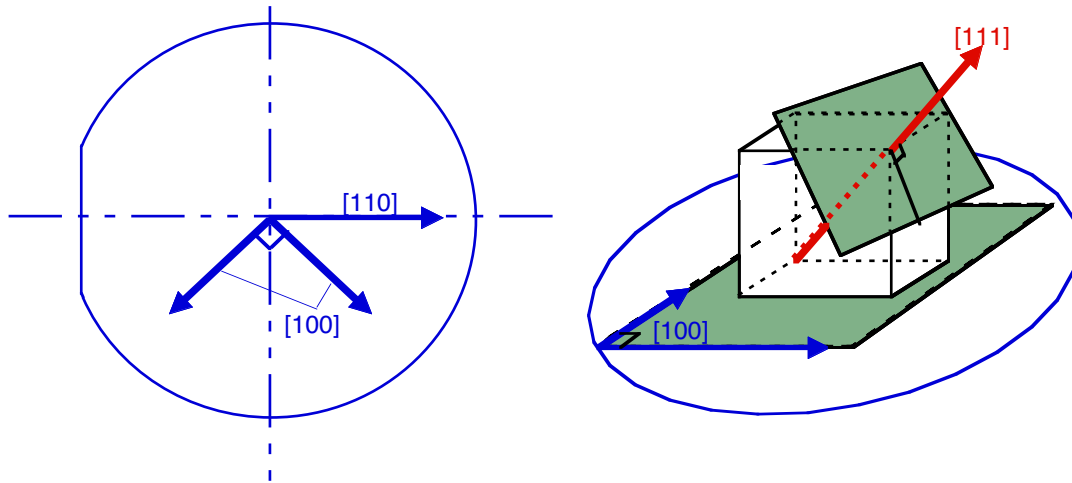


Figure 3.11: Illustration of the planes in silicon.

It is relatively easy to see the under-etching phenomena under a microscope during the etch due to the non-transparent nature of the part which has yet to be etched. Thus this situation can be readily avoided. However, determining the difference between perfectly etched and over-etched is not easily done without using the SEM. Because this characteristic may have an effect on the final quality of the oscillator and therefore its force sensitivity, it is best to closely watch the etch and take the oscillator out within 4 hours of the last noticeable attachment in order to fabricate reliable oscillators.

### 3.2.6 EXTRACTION: OVERCOMING STICTION

When the oscillators come out of the etch, surface tension brings them in contact with the silicon back and various forces, such as van der Waals forces, keep them stuck even after they have dried completely [42-44]. An accessible method for overcoming this problem involves rinsing the still-submerged oscillators in a solution of deionized water and ethanol. The wet chip is then frozen by applying a vacuum and continuously pumped on until the frozen solution completely sublimates away.



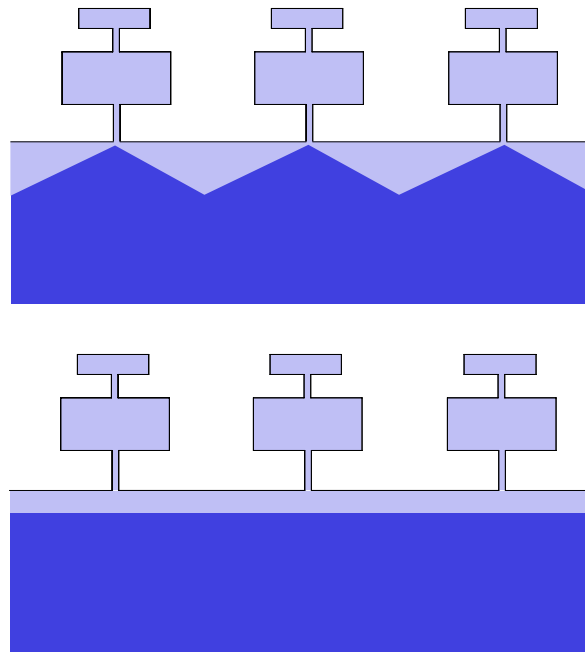


Figure 3.12: The oscillators resulting from the anisotropic KOH etch, when the mask is aligned (a) at  $45^\circ$  to the wafer flat and (b) parallel to the flat.

Surface tension no longer exists and thus stiction is avoided. The oscillators are then ready for use in the NMRFM experiment.

### 3.3 FABRICATION OF OSCILLATORS FROM SOI WAFERS

The above process has many apparent faults. First of all, the long and temperamental KOH etch results in many defects and non-uniform oscillators. Also, the implant itself causes serious defects, jeopardizing the quality of the final product and therefore increasing the damping. In addition, the final oscillators as prepared above are highly conductive and this could be a potential problem for NMRFM applications due to the damping that will result from eddy currents. It would be most beneficial to do away with all of these factors, and recently the opportunity has been presented to do just that. Silicon-On-Insulator (SOI) wafers have been acquired, and are seemingly perfect for the fabrication of these oscillators. The process has to be modified slightly

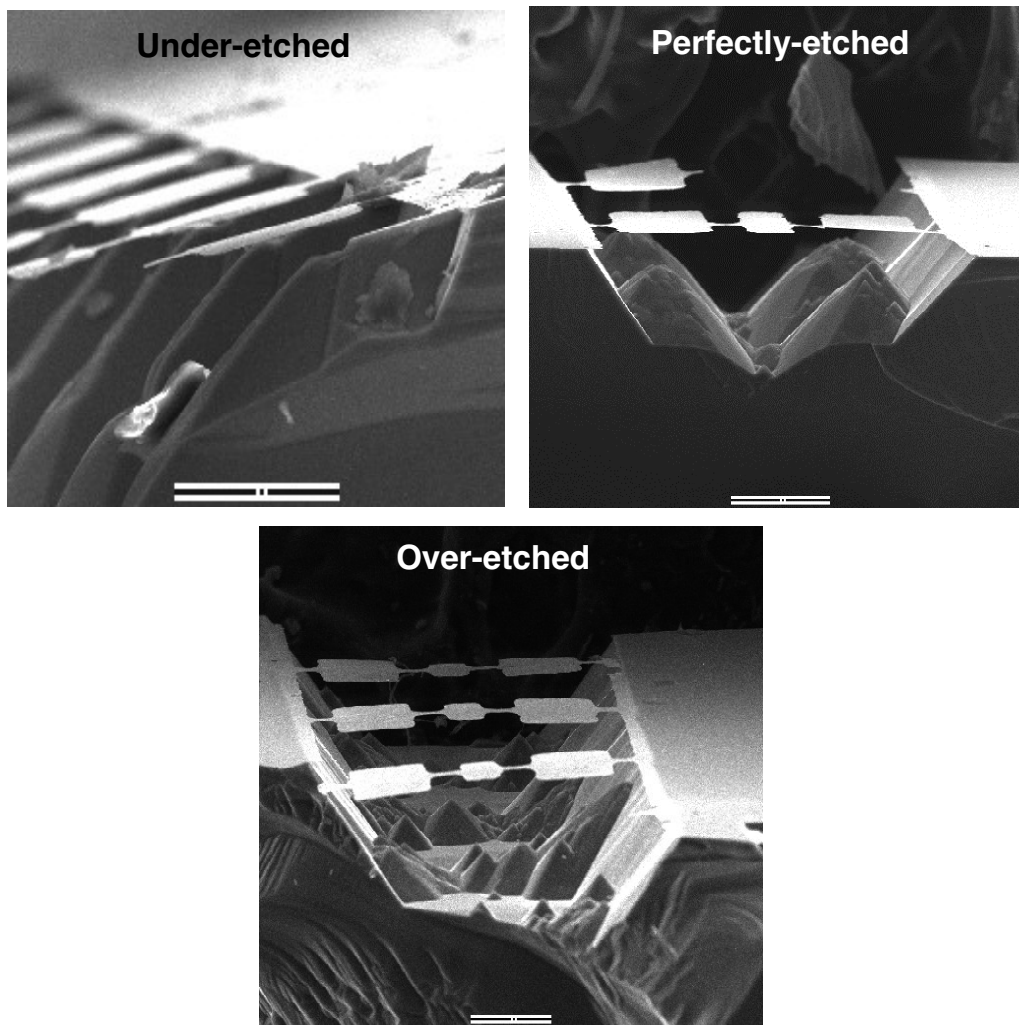
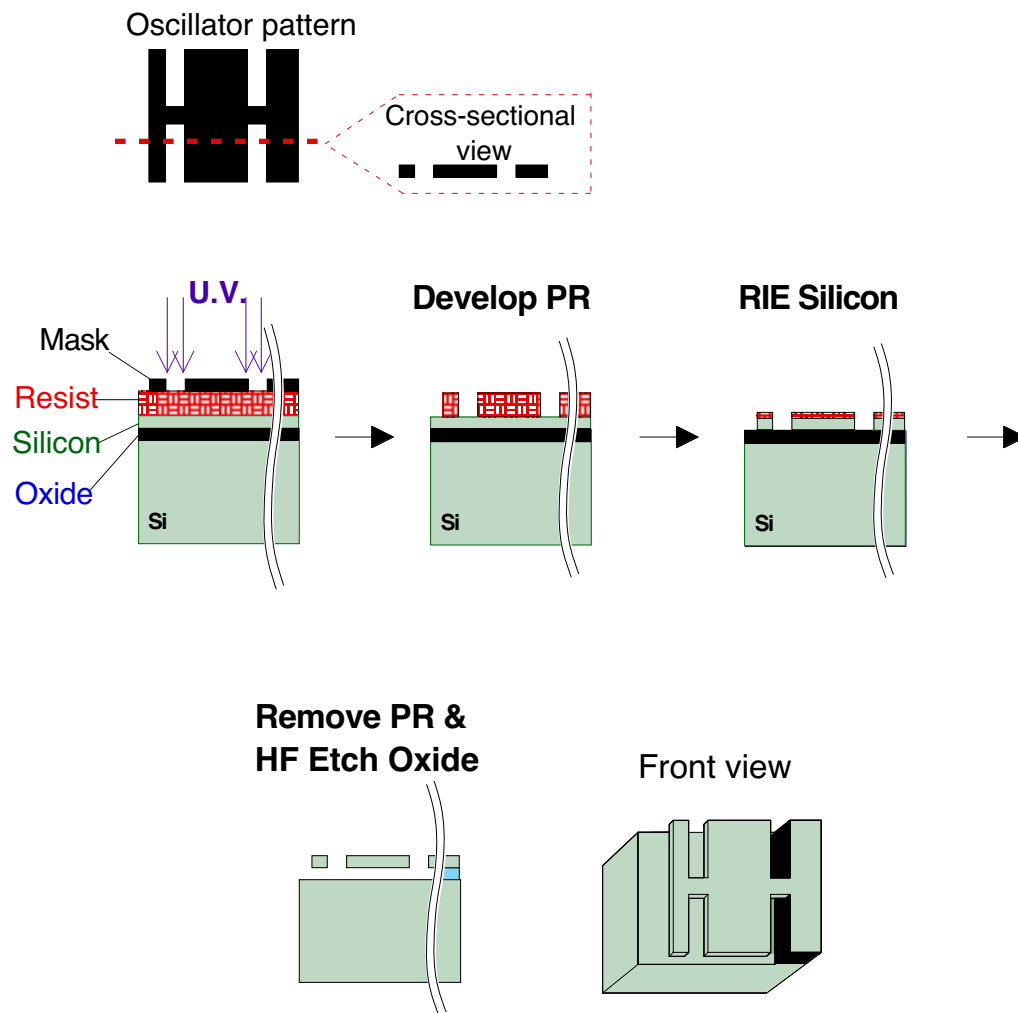


Figure 3.13: SEM images of oscillators which have been left in the KOH for varying times (between 5 and 8 days).

Figure 3.14: Outline of the process used to fabricate oscillators using the SOI wafers.

## SOI Oscillator Fabrication



to accommodate these new substrates. This is illustrated in Figure 3.14.

The first important difference is that the SOI mask must be a negative version of the plain Si one since the oscillators will be protected by the photoresist. The reactive ion etch is used to remove the 350 nm thick exposed silicon surfaces. The wafer will then be placed in a carefully-watched BOE which will etch the oxide while leaving the pure silicon<sup>5</sup>. This will result in some under-cutting of the substrate, but it is unclear whether this is even a problem at all. The resulting oscillators will be 350 nm thick, single crystal silicon; this is comparable to the boron-doped thicknesses of 200 – 400 nm and has little to no variation. Because the processing has eliminated the ion implantation and the KOH wet-etch steps, almost no defects will be created, and the losses due to movement of dislocations will be greatly minimized.

However, due to the expense of these wafers, and thus the inability to replace them, most processing up to this point has still used the boron-doping method. Once the design of the oscillators has been optimized and tested in the boron-doped process, the SOI wafers will prove to be a significant benefit.

### 3.4 CHARACTERIZATION

The oscillators are characterized using a fiber optic interferometer to measure their resonance frequencies and their Q's. SEM images are used to determine the thickness of the oscillators and therefore help to give an estimate of the spring constants. This section will summarize these results and give the corresponding force sensitivities.

#### 3.4.1 FREQUENCY SCANS

Scans are performed using Labview to externally scan through a frequency range with the desired step size and dwell time. At each point, the output of a lock-in

---

<sup>5</sup>This procedure has been attempted once unsuccessfully due to the extremely long time necessary to etch 100  $\mu\text{m}$  of oxide. Creating a mask with tiny holes in the oscillators may help overcome this problem. Successful etches of 1 $\mu\text{m}$  have been done using BOE on SOI wafers [45].

amplifier is recorded. The oscillators are placed onto a piezo which is excited with a variable drive voltage, determining the amplitude of the piezo oscillation. In air, it is necessary to use a drive of at least 1 V to get an appreciable signal due to air resistance. Also, in air it is common for the substrate to have strong resonances of its own which are comparable in size to the oscillator resonances. A scan of the substrate is therefore done in order to find the location of the strongest substrate peaks so that they are not mistaken for oscillator resonances.<sup>6</sup>

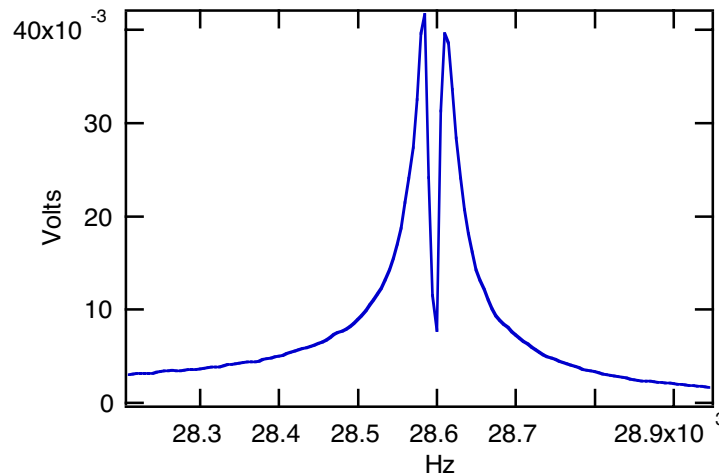


Figure 3.15: Frequency scan showing the effect of using too high a drive voltage on the piezo. The dip in the middle of the resonance is due to the oscillator passing through an interference fringe.

Once the system is put into vacuum (less than 1 mTorr) the drive can be decreased significantly, to as low as 0.01 V for a resonance with a Q of 10,000. Lowering the drive is necessary to avoid amplitudes which are too large to remain in the linear portion of a fringe, as shown in Figure 3.15. (See also Section 4.2.2). Also, driving the oscillators at very high amplitudes tends to weaken them, causing them to break. Subsequent scans with a lower drive and a smaller step size will eventually

<sup>6</sup>The quality factors of the substrate resonances will not increase significantly in vacuum, so this is also another method for distinguishing the two.

result in an accurate determination of the  $Q$ . If the resonance has been accurately characterized, the lower drive should decrease the amplitude proportionally and the smaller step size should make no difference, as shown in Figure 3.16. If this is not the case, as is illustrated in Figure 3.17, then smaller step sizes with a lower drive must be used until it is.

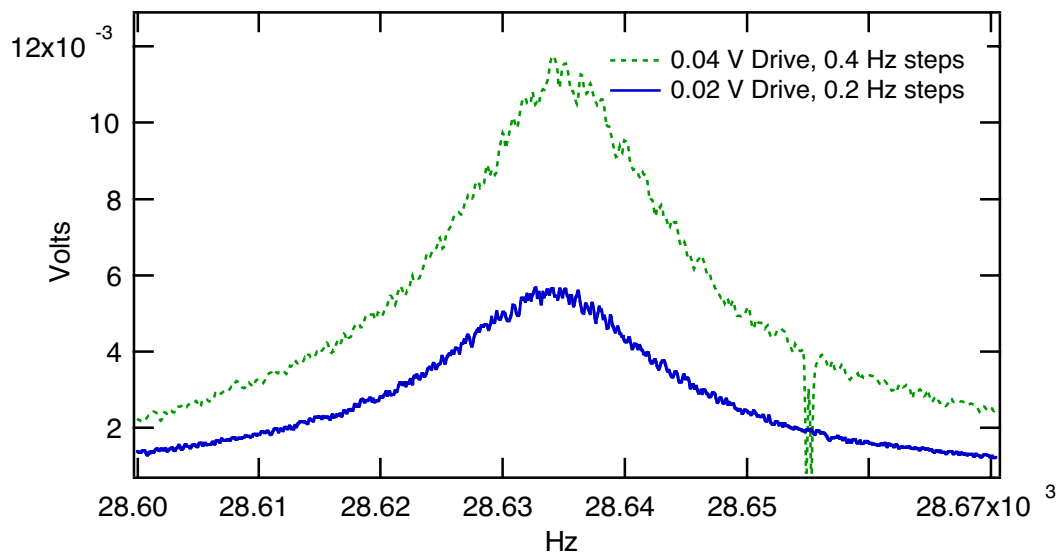


Figure 3.16: Frequency scan illustrating the desired effect of lowering the drive and step size. When this behavior is observed, the oscillator has been well characterized, and an accurate determination of its  $Q$  can be found.

Figure 3.18 shows another effect that lowering the step size has on the measured resonance. Although, of course, the resonance is physically in the same location despite how it is measured, this is not the observed result. This is purely an artifact in Labview and therefore can be ignored as long as its effect is taken into account when finding the true value of the resonance frequency.

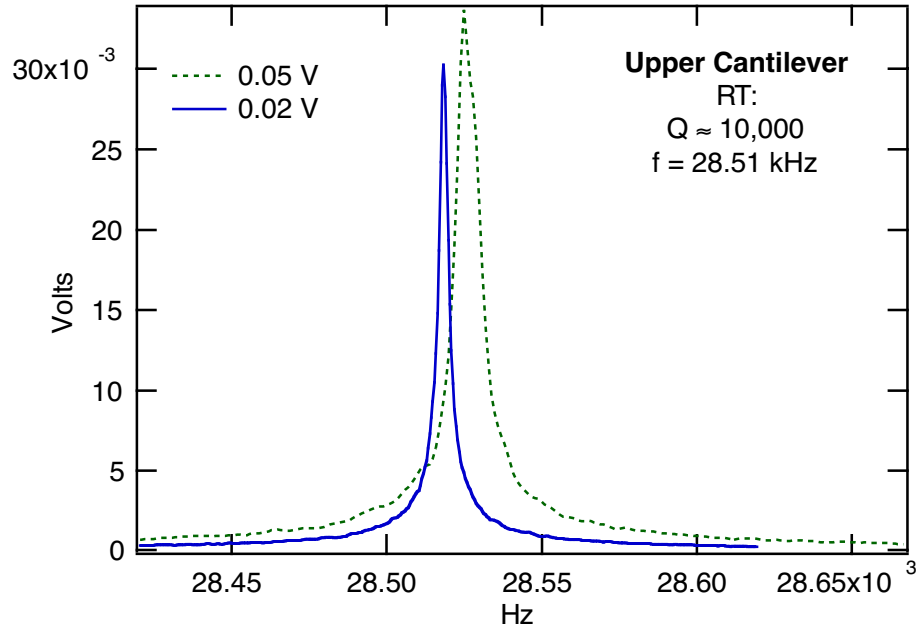


Figure 3.17: Frequency scans of the upper cantilever mode of a double torsional oscillator. Scans taken in vacuum at two different drive voltages.

### 3.4.2 RESONANCES OF DOUBLE-TORSIONAL OSCILLATORS

Figure 3.19 shows a typical frequency sweep of one double-torsional micro-oscillator [46]. Four resonances are generally evident.<sup>7</sup> These are assigned, in order of increasing frequency, to the lower cantilever, lower torsional, upper cantilever, and upper torsional modes. The type of mode has been verified by moving the interferometer laser spot to various points on the oscillator while maintaining the same excitation signal. (See Figure 3.20 for an example.) For the lower cantilever mode, both sides of the head and both sides of the wing move in phase. For the lower torsional, both sides of the head and both sides of the wing move with opposite phase, and the same side on the head and the wing move together. Similar tests have verified the upper

<sup>7</sup>If the fiber is pointed in the middle of the oscillator, the torsional resonances often are too weak to show up. Also, the double-torsional oscillators are known to have more than four observed resonances, but for the purposes of this research only the four described in Section 3.1.1 are investigated.

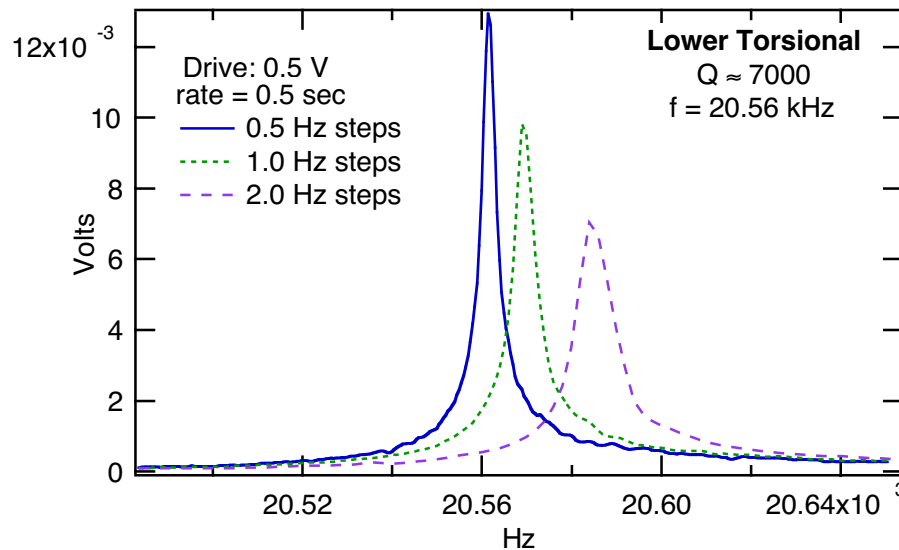


Figure 3.18: Frequency scans on the lower torsional mode of a double torsional oscillator illustrating the effect of the step size on the measured location of the resonance. All data was taken at a rate of 500 ms. As the step size decreases from 2 Hz steps (long dashes) to 0.5 Hz steps (solid line), the measured location of the frequency is lowered by approximately 20 Hz. This is purely an artifact of Labview, and as smaller step sizes and time constants are used, the actual value of resonance is found.

resonance modes as well. Finite element modeling [47] has also been used to verify each mode, as is shown by the vertical lines in Figure 3.19.

The location of the resonance frequencies did not change greatly for the different dimensions of the upper torsional design. Designs with the smaller head ( $100 \mu\text{m}$  wide as opposed to  $150 \mu\text{m}$ ) have slightly larger resonance frequencies (about 5 kHz larger on average) than large-head oscillators from the same wafer. The width of the neck was varied from  $14 \mu\text{m}$  to  $20 \mu\text{m}$ , but the effect of this on the observed resonances was not found. It is expected that increasing the width of the neck would increase the resonant frequencies, but the effect from a  $4 \mu\text{m}$  change was evidently too small to be detected reliably with the observed variations within each batch of oscillators.



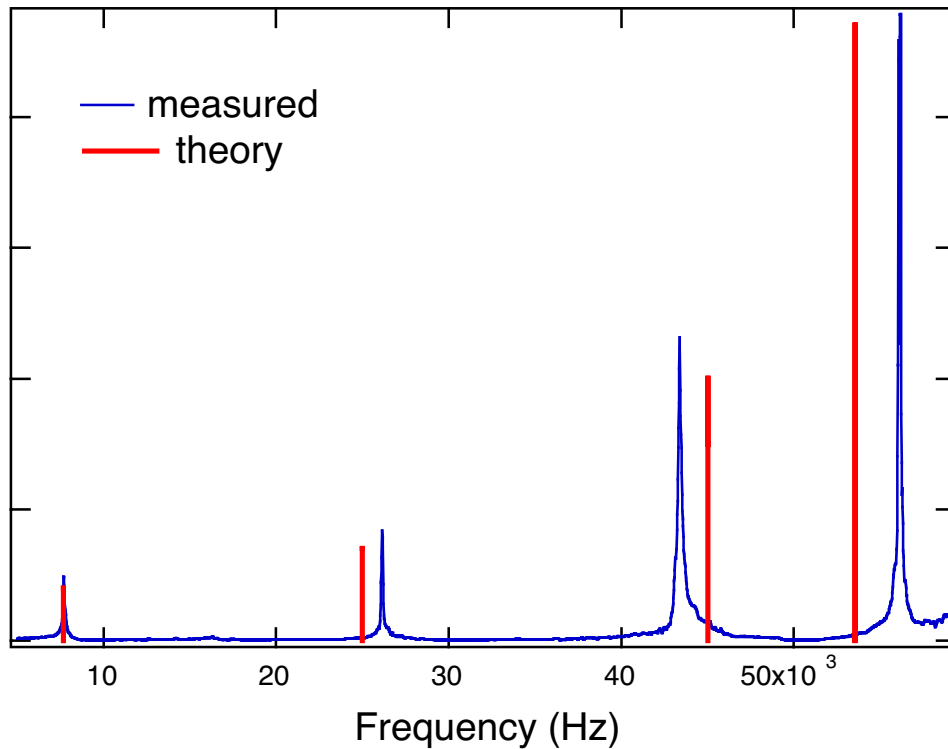


Figure 3.19: Frequency scans of the four modes of a double-torsional oscillator performed at room temperature and vacuum. Vertical lines are theoretically predicted locations for the resonances [47].

As the thickness of the oscillators decreased, the observed resonance frequencies also decreases. However, the thicknesses, which varied from 150 – 350 nm, were not determined accurately enough to do a quantitative analysis of the effect.

#### 3.4.3 LOW TEMPERATURE RUN

The Q's of the oscillators are expected to increase when the temperature is lowered, as has been observed in their larger counterparts [48]. However, it was discovered that this is not the case for the boron-doped oscillators which have been subjected to the long KOH wet-etch. The defects are too numerous and it seems the quality factor is most greatly affected by these at low temperatures. The characterization results of

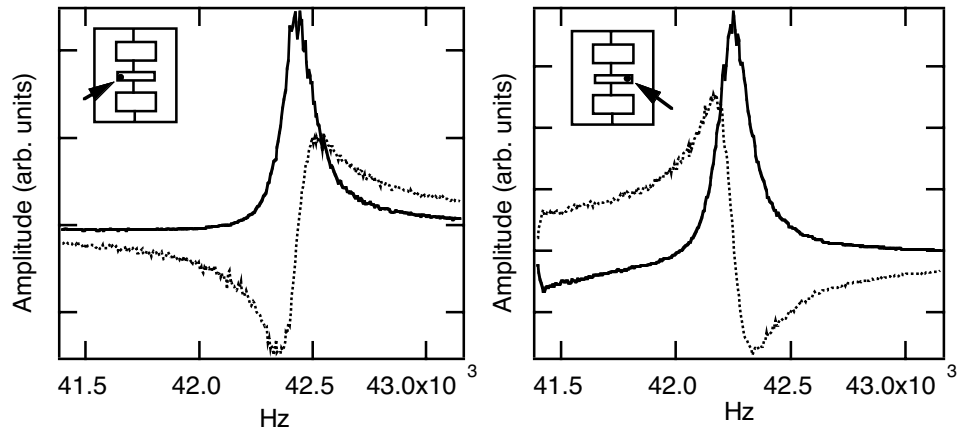


Figure 3.20: Phase-sensitive motion detection of a resonance of a triple-torsional oscillator. The fiber was pointed at opposite sides of the head. Opposite phases were observed for the two locations, indicating this mode is most likely a torsional mode of oscillation.

a scan performed at 77 K are shown in Figure 3.21 for the four resonances, with the scans of the same oscillator resonances at room temperature given for comparison. It is clear that at low temperatures, the  $Q$  in fact *decreases*. This effect has not been remedied, but it is hoped that pure single-crystal silicon oscillators fabricated from the SOI wafers will result in a different low temperature behavior.

#### 3.4.4 THICKNESS MEASUREMENTS

Oscillators were annealed at different temperatures for different times in order to determine the dependence on the thickness. It was found that the thickness was only mildly dependent on the anneal conditions, and instead depended most strongly on the doping level. The oscillators doped with  $2 \times 10^{16}$  boron ions/cm<sup>2</sup> had an average thickness of 200 nm, while those doped with  $4 \times 10^{16}$  boron ions/cm<sup>2</sup> had an average thickness of 300 nm. This is illustrated in the SEM images in Figure 3.22(a) and (c).

The anneal time did have a slight effect on the thickness, as is shown in Table 3.2 and Figure 3.22(b),(c), and (d). All of the oscillators were initially doped

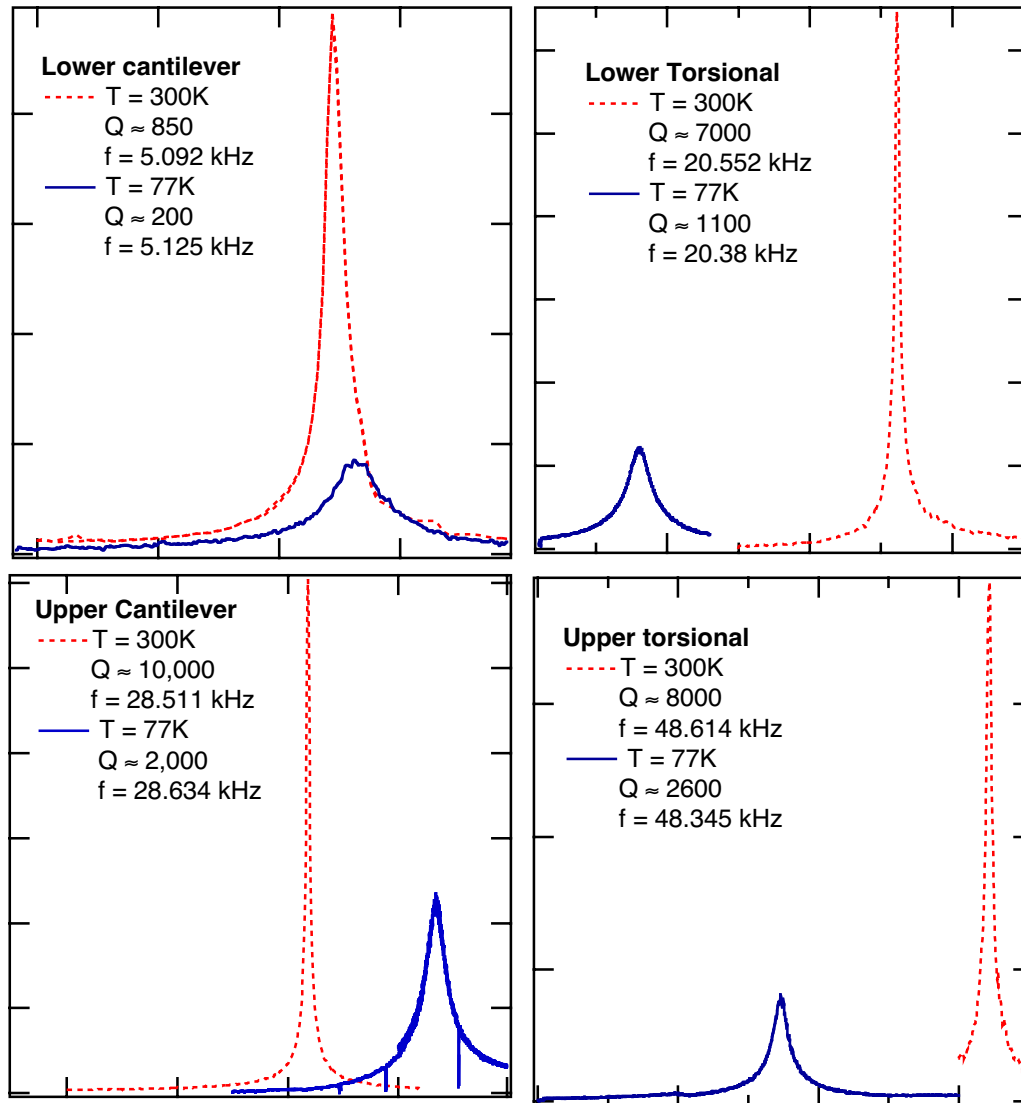


Figure 3.21: Frequency scans of the four modes of a double-torsional oscillator performed at room temperature (dotted line) and 77 K (solid line).

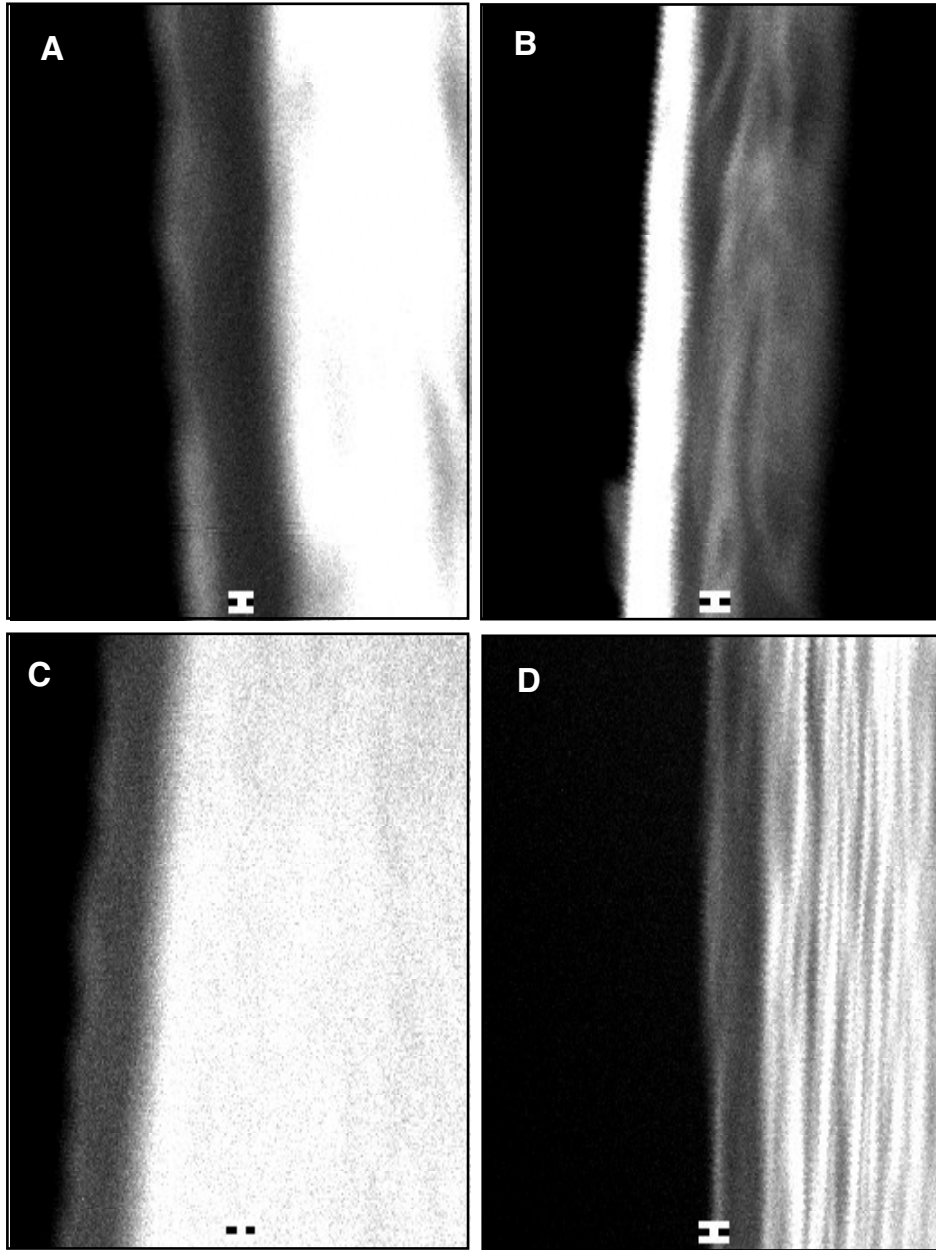


Figure 3.22: SEM images of oscillator thicknesses for different anneal times and doping levels. (A)  $4 \times 10^{16}$  ions/cm<sup>2</sup>; 1000°C for 180 min. (B)  $2 \times 10^{16}$  ions/cm<sup>2</sup>; 975°C for 180 min. (C)  $2 \times 10^{16}$  ions/cm<sup>2</sup>; 1000°C for 180 min. (D)  $2 \times 10^{16}$  ions/cm<sup>2</sup>; 1000°C for 30 min. All bars are 100 nm long.

with  $2 \times 10^{16}$  boron ions/cm<sup>2</sup>. It has been observed that a 975°C anneal results in oscillators which can be up to two times thinner than those annealed at 1000°C. However, changing the anneal parameters too much resulted in unsuccessful KOH etches and therefore an extensive study of this effect could not be done for this doping level.

Table 3.2: Thickness vs. Anneal for a dose of  $2 \times 10^{16}$  boron ions/cm<sup>2</sup>

	1000°C	975°C	950°C
15 min	no etch	no etch	no etch
30 min	100 nm	no etch	no etch
60 min	150 nm	100 nm	no etch
90 min	200 nm	150 nm	no etch
180 min	250 nm	150 nm	no etch

#### 3.4.5 FORCE SENSITIVITY

It has been found that the Q's for the upper resonances of the oscillators (regardless of the different lateral dimensions) are generally on the order of 10,000 at room temperature and vacuum. Using this value in equation 2.19, along with a typical value for the effective spring constant  $k \approx 5 \times 10^{-3}$  N/m (for a 300 nm thick oscillator), the force sensitivity is (for the upper torsional 62 kHz mode):

$$F_{min} = 1.5 \times 10^{-16} \text{ N}/\sqrt{\text{Hz}} \quad (3.12)$$

This value demonstrates the advantage of using the multi-torsional oscillator design. As the oscillator size, and therefore thickness, decreases, it is expected the sensitivity will improve due to a lower effective spring constant.

## CHAPTER 4

### NMRFM EXPERIMENTAL APPARATUS AND CONSIDERATIONS

*“If we knew what it was we were doing, it would not be called research, now would it?”*

*- Albert Einstein*

Once oscillators have been made with a thermal noise low enough to detect the desired volume of sample, the rest of the microscopy apparatus needs to be attended to. Aside from the oscillator, the main components of an NMRFM are the cryostat probe, which holds the sample area in vacuum and at low temperatures, the fiber-optic interferometer, which detects the motion of the oscillator, the magnetic field gradient, and the modulation electronics. A schematic of the entire experimental set-up is illustrated in Figure 4.1. Additionally, a method is needed to mount the sample onto the oscillator. All of these components will be discussed in this chapter. Focus will be given to the fiber optic interferometer and the sample mounting, as these have undergone the most improvements.

#### 4.1 CRYOSTAT PROBE

A vacuum-sealed cryostat probe is used which fits into a He dewar inside of an 8.2 T NMR magnet. Simple quick-connect feedthroughs are used which allow for external control of the translation. Figure 4.2 shows the sample area inside the

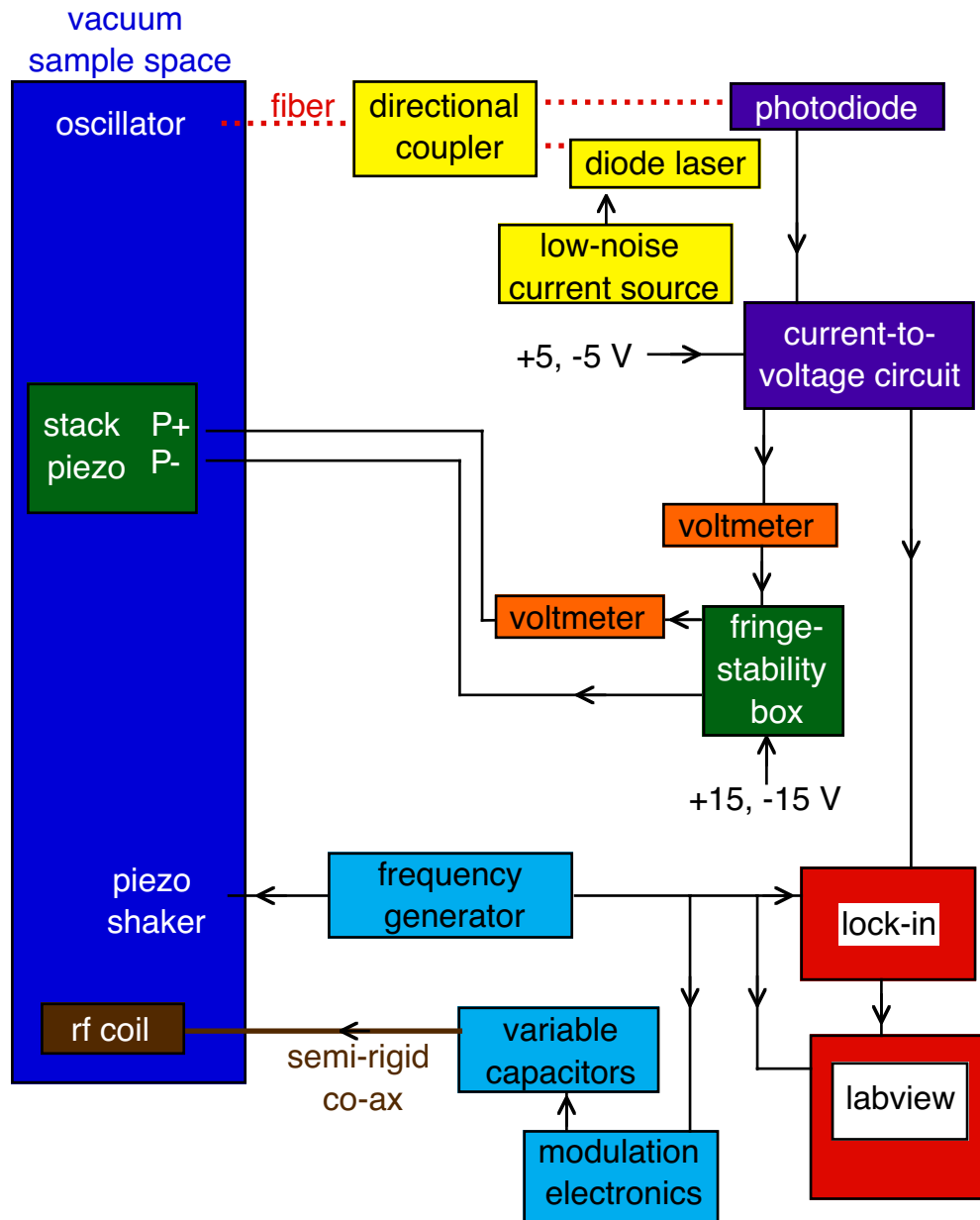


Figure 4.1: Overview of the entire experimental set-up for NMRFM.

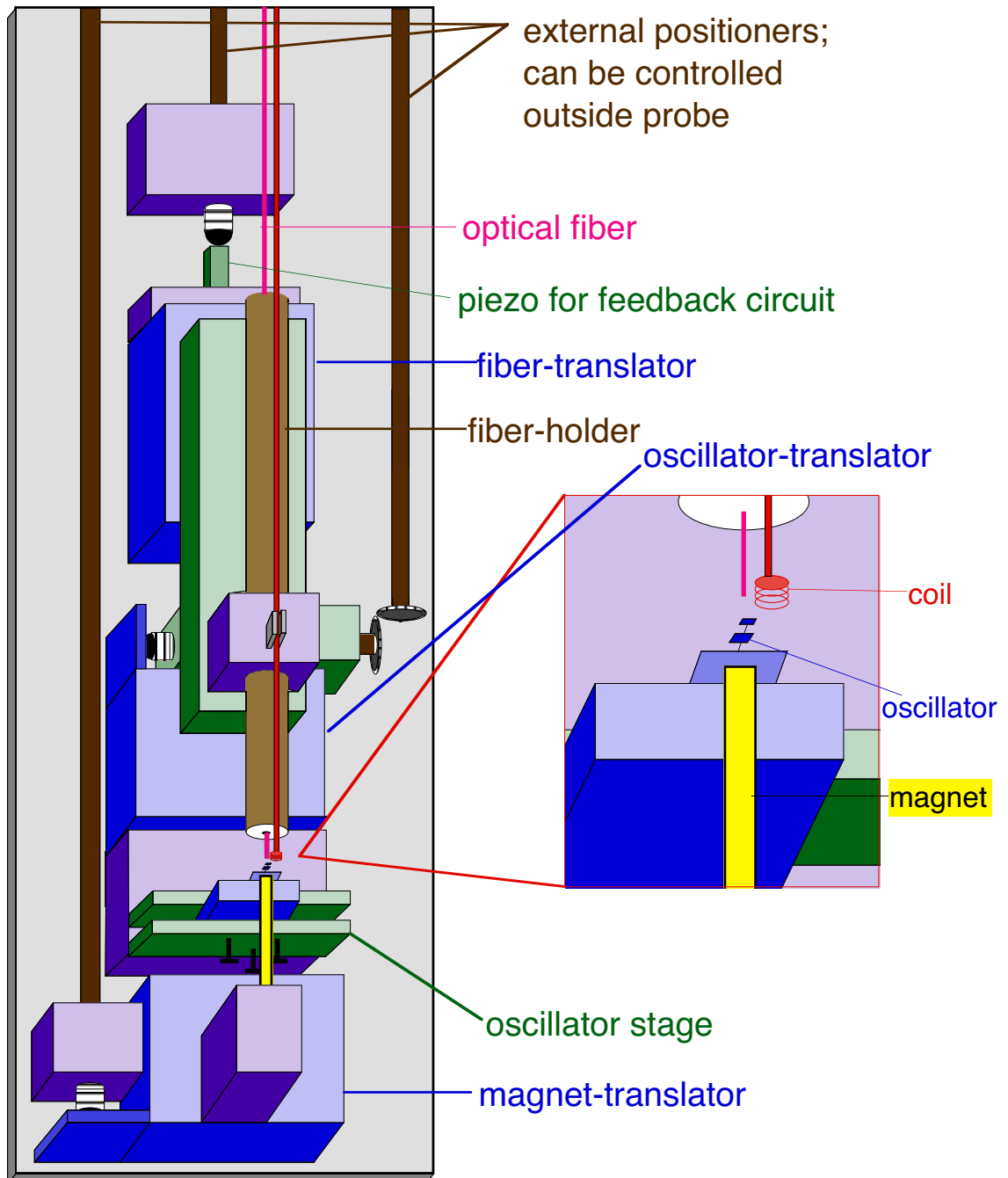


Figure 4.2: The sample stage showing the various coarse positioners.



probe. There are three coarse positioning stages that allow for alignment of the fiber to the oscillator. The fiber-translator allows for  $z$ -approach of the fiber-stage towards the oscillator-stage. The oscillator-translator controls the  $y$ -motion of the oscillator stage. Also, the stage the oscillator is mounted on allows for  $x$ -motion as well as small tilts when necessary. The first two are ball-bearing translation stages controlled externally through a gear set-up. However, the last one cannot be controlled once the probe has been sealed. Therefore, everything must be reasonably sturdy so that putting on the large vacuum can does not result in too much misalignment of the fiber. Any misalignment that occurs can be detected by observing the changes in the DC signal. The direction of this misalignment cannot be determined since there is no visual access to the sample space when the probe is closed, so realignment is (generally) not possible.

In addition to the positioning translators on the sample stage, there is also a translator which allows for movement of the permanent magnet (i.e. the field gradient) in the  $z$ -direction. This is the positioner that allows for a one-dimensional scan to be performed (Section 2.1.4). It can be controlled externally with a rotary shaft; a 360 degree clockwise rotation equals a 100  $\mu\text{m}$  translation of the magnet away from the oscillator.

The oscillator is mounted onto an aluminum plate which has an electrical connection, and this in turn is mounted onto a piece of piezo. The piezo sits onto a larger piece of aluminum which fits into the oscillator-stage and can be aligned. The two aluminum pieces serve as the electrodes for the piezo stack. The piezo is used for the initial characterization of the oscillators, as was demonstrated in the previous chapter. This is the same mounting process which is used during an experiment, so that characterization and various tests on the oscillator can be performed during an NMRFM experiment if necessary.

## 4.2 FIBER-OPTIC INTERFEROMETER

Possibly the most crucial aspect of the microscope is the fiber-optic interferometer [49-52]. An overview of the interferometer is given in Figure 4.3. A 680 nm diode laser with an optical isolator is used as the light source. It is coupled via a fiber connector to one arm of fiber from the directional coupler. The light passes through the directional coupler and out to the two optical fibers on the opposite side. One of these is not in use at the moment,<sup>1</sup> and has a bad cleave so that there is negligible reflection from the end. The light which passes through the fiber which is aligned on the oscillator experiences interference between the light which is internally reflected from the end and the light which is reflected from the oscillator. This interference pattern travels back towards the directional coupler, which sends the signal in its entirety to the fiber leading to the photo diode. The signal from the photodiode is converted to a voltage and then sent to a lock-in amplifier and a standard voltmeter. The DC level of this signal is sent through a feedback circuit box which adjusts the  $z$ -position of the fiber with a piezo so that the signal is held at the sensitive area of the interference fringe (See Section 4.2.2).

### 4.2.1 PHOTO DIODE CIRCUITRY AND CONSIDERATIONS

In order to know what signal is expected, the amount of light going to the photodiode must be known. This depends on the initial amount of light from the laser and the quality of the cleave.

The first factor has posed quite a few problems. It seems the output of this diode laser has diminished over time. When an initial measurement was made of the power output, it was found that the laser put out approximately 6 mW before being connected to the fiber. Approximately 2 mW of this was transmitted out to the

---

<sup>1</sup>This unused fiber has potential to be used as a reference signal. Also, should something happen to the fiber which is being used, this extra one allows for the quick repair of the system without changing the entire directional coupler.

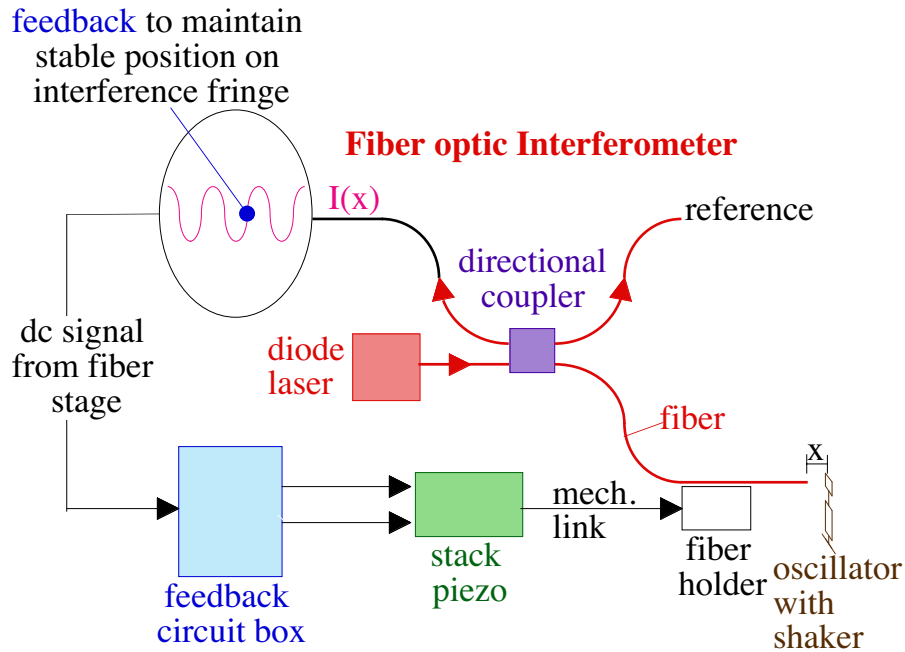


Figure 4.3: Overview of the fiber-optic interferometer.

oscillator and approximately  $60 \mu\text{W}$  was reflected to the photodiode. A more recent measurement indicated that approximately  $1 \text{ mW}$  was going to the fiber, resulting in approximately  $10 \mu\text{W}$  reaching the photodiode. However, approximately one year later, the same measurement found that only  $100 \mu\text{W}$  was being transmitted to the oscillator, resulting in approximately  $1 \mu\text{W}$  of light reaching the photodiode. Thus a factor of 10 depletion has been observed, and the amplification circuitry has been modified to account for this.

The photodiode signal is converted to a voltage by the circuit shown in Figure 4.4. Because of the design of the fringe stability circuit, a DC voltage of approximately  $1 \text{ V}$  is desired in order for the fringe-locking to occur (See Section 4.2.2). Therefore, when the factor of ten decrease was observed, the  $100 \text{ k}\Omega$  gain resistor was replaced with  $1 \text{ M}\Omega$  so that the amplification factor increased by a factor of 10 also. This also increased the noise level by a factor of 10, but because the photodiode noise is considerably lower than the necessary detection sensitivity, this has not resulted

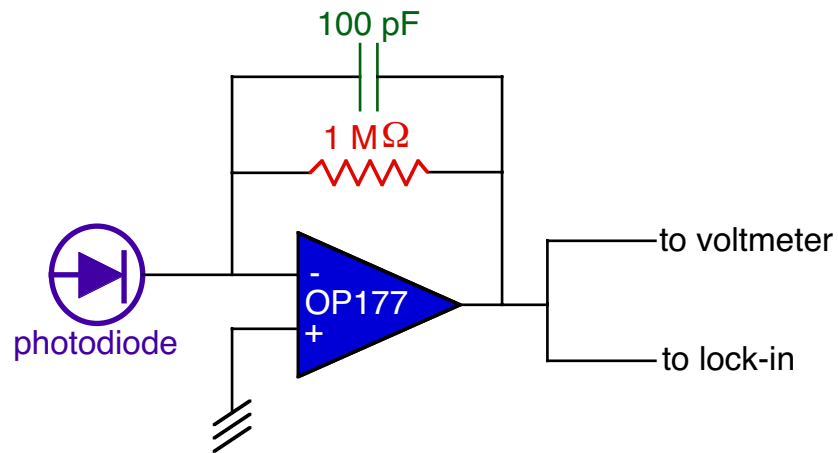


Figure 4.4: Schematic of the voltage-to-current circuit.

in a problem. Thus the overall conversion from power to volts can be found by:

$$\begin{aligned} \text{Voltage output} &= \\ \text{Power (in W)} \times \text{PD Responsivity (in A/W)} \times \text{Gain (in } \Omega), \\ &= \text{Power (in W)} \times 0.6 \text{ (A/W)} \times 10^6 \Omega. \end{aligned}$$

The cleave at the oscillator end strongly affects the strength of the observed signal. A maximum of 4 percent of the light can be reflected back from the fiber surface when a perfectly flat cleave is achieved. This, however, has never been accomplished in the current experiment. A cleave which results in approximately 2 percent reflection is considered “good” and most likely cannot be improved very much with the available tools.

Small photodiodes (EG-G FFD-040; Area  $\approx 1 \text{ mm}^2$ ) have been used in the past. An overly complicated method was used to cut the protecting glass and mount the fiber to the photodiode. It was decided that a larger, and therefore more stable, photodiode (Area  $\approx 1 \text{ cm}^2$ ) would be used. The glass no longer needs to be cut away; instead, an index-of-refraction-matching liquid is used on the surface to ensure almost

total transmission.<sup>2</sup> This new set-up allows for quick repair and a still negligible noise level.

#### 4.2.2 FEEDBACK CIRCUIT FOR FRINGE STABILITY

When the fiber is aligned to an oscillator, fringes in the DC signal are observed. For example, if the fiber is not reflecting off of anything other than its own surface, then a DC value of 1 V is standard. As some light begins to be reflected externally and an interference pattern develops, small deviations of the 1 V signal should be noticeable. At first they may appear to be just noise, but as the fiber is moved closer, the deviations will increase. (The average DC level may also shift slightly upward, but usually never by more than a fraction of a volt. For this example, it will be assumed to remain at 1 V.) Typical deviations from the DC level are on the order of 30 percent while the fiber is still approximately 50-100  $\mu\text{m}$  from the oscillator. For the current example, this simply means the observed voltage will be fluctuating from 0.7 to 1.3 V. If this is not observed, then most likely the reflection off of the oscillator is poor due to a small tilt angle (i.e. the fiber is not normal to the oscillator).

It is extremely important to measure and record the voltage values of these fringes and to notice whenever they change. Each peak-to-peak deviation corresponds to a movement of the fiber by  $\lambda/4$  (from simple interference considerations). Now, since the measured voltage is converted directly into an amplitude of oscillation, it should be clear that the method of conversion depends very much on the position along the fringe. Ideally, it is hoped that all measurements are made while the DC level is at the same point on a fringe, and therefore an accurate conversion can be made from voltage to distance which is not changing. Since remaining at *exactly* the same point is experimentally impractical, a more reasonable solution is to attempt to remain on the linear portion of the interference pattern. Figure 4.5 illustrates the

---

<sup>2</sup>It has also been found that, although the indices of refraction do not match, water works as a reasonable substitute.

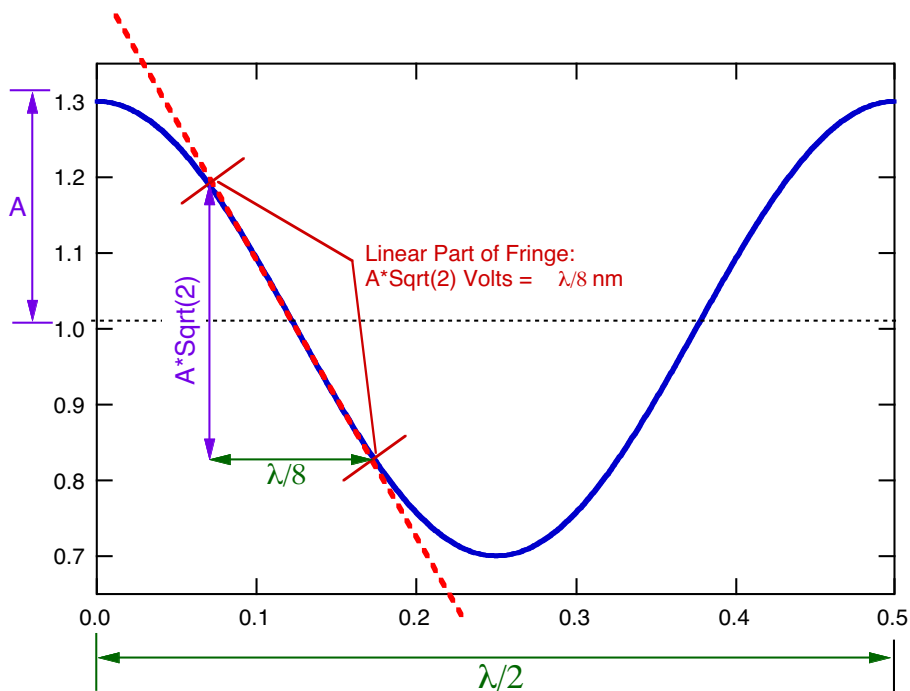


Figure 4.5: Typical DC signal expected illustrating the fringes. The linear part of the fringe spans a distance of approximately  $\lambda/4$ .

benefit of this method. Figure 4.6 is an example of a scan done without locking on a fringe. Although the signal is not always this noisy, it is a good illustration of what results when there is no fringe stability at all.

A fringe-stability box was made which keeps the fiber locked onto the linear region of an interference fringe. This schematic is given in Figure 4.7. A stacked piezo has been placed immediately before the fiber-holder stage. A varying voltage from  $-15$  to  $+15$  volts controls the length of the piezo and thus the position on a fringe. The DC level is used at a setpoint for the feedback, and the piezo adjusts its length so that the DC level remains at a constant pre-set value. There are two inputs into the piezo; one is a manual control of the movement which allows for an accurate measurement of the fringe amplitude, and the other is the feedback circuit. The manual input can be used while the automatic part of the circuit is running,

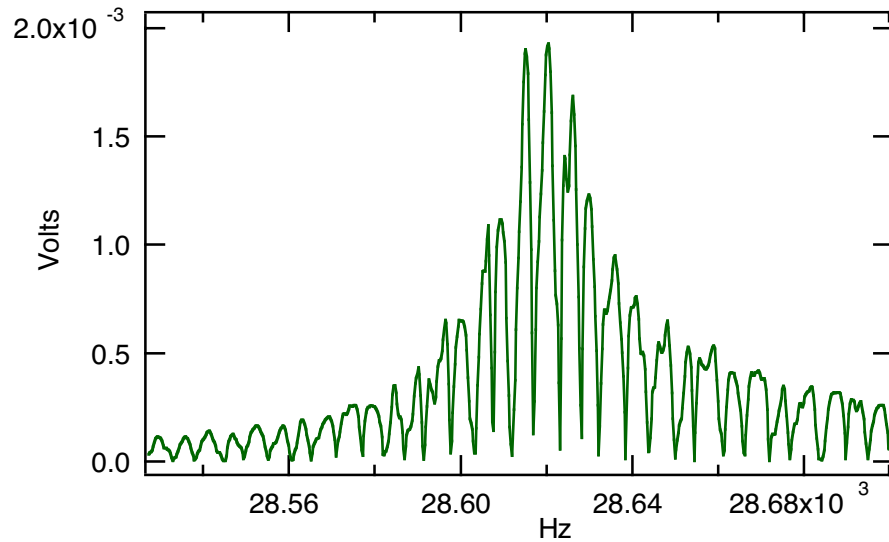


Figure 4.6: Frequency scan done when the fiber was not held stable onto a fringe.

allowing for adjustments when necessary. The 30 V range allows for travel between approximately 2 complete fringes, corresponding to a total distance of  $\lambda$  ( $= 680$  nm). Fringes of at least 0.10 V (0.20 V peak-to-peak deviation) are needed to reliably lock on a fringe, regardless of the actual DC value. However, larger fringes are desired and are reasonably easy to achieve. See Appendix B for the specific details of operation.

### 4.3 MAGNETIC FIELD GRADIENTS

In the current one-dimensional NMRFM experiment, an external permanent magnet is used to supply the field gradient, while the sample is mounted onto the mechanical oscillator. All future experiments will most likely be done with the sample held externally and the magnet on the oscillator [53, 54]. Efforts are underway to deposit cobalt magnets onto the double torsional oscillators. Once this is accomplished characterization needs to be done to determine the exact strength of the field gradient. This future method offers the benefit of a fixed microscopy apparatus in which a new sample can easily be mounted for every new run. The oscillator with the magnet

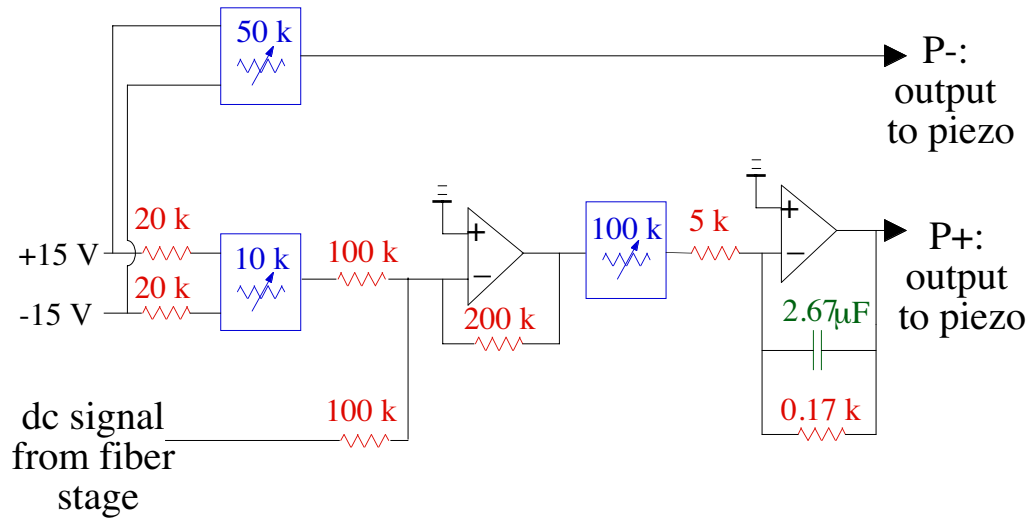


Figure 4.7: Diagram of the feedback circuit used for fringe stability.

will already be well characterized, and can remain in place no matter what sample is used.

However, for the current experimental set-up, it was decided to use a long permanent magnet with a well-defined field gradient in order to eliminate one more unknown from an already not-well-understood experiment. The magnetic field along the  $z$ -axis from a long cylindrical bar (length  $L$ , radius  $r$ ) is given by:

$$B(z) = 4\pi M \left( \frac{z}{2\sqrt{z^2 + r^2}} - \frac{z - L}{2\sqrt{(z - L)^2 + r^2}} \right), \quad (4.1)$$

which yields the field gradient:

$$\frac{dB}{dz}(z) = 4\pi M \left( -\frac{z^2}{2(z^2 + r^2)^{3/2}} + \frac{1}{2\sqrt{z^2 + r^2}} \right. \\ \left. + \frac{(z - L)^2}{2((z - L)^2 + r^2)^{3/2}} - \frac{1}{2\sqrt{(z - L)^2 + r^2}} \right). \quad (4.2)$$

The above equations have been calculated assuming the end of the bar is at  $+L$  along the  $z$ -axis. The magnet used is a cylindrical iron rod 24 mm long and 3 mm in diameter. Equations 4.1 and 4.2 have been plotted for these specific parameters



and are shown in Figure 4.8. Assuming that the magnet is 1 mm away from the oscillator, then the static field at this point (to be added to 8.2 T external field) is 0.47 T, and the field gradient is 400 T/m.

#### 4.4 MODULATION ELECTRONICS

Figure 4.9 gives an overview of the electronics used to generate the rf pulse which causes the cyclic adiabatic inversion of the magnetization. A modulation box supplies the initial offset frequency, the modulation frequency, and the modulation amplitude. The signal output is a varying voltage with the desired parameters, as shown in Figure 4.10. The decay time to resonance, the initial offset, the modulation amplitude, and the modulation frequency are all variable parameters.

This voltage signal goes to the input of a HP8656B frequency modulator which translates the voltage into a frequency. It then modulates the frequency about the pre-set carrier frequency. This is the desired cyclic adiabatic inversion sequence sent to the input of the power amplifier and then to the coil.

The length of the pulse is also determined by the modulation box. This is in the form of a logic pulse sent to the logic input of the power amplifier. This pulse is a high-low-high pulse which turns the rf power on for the time which the pulse is low. A trigger pulse is also sent to the digitizer when the logic pulse is sent to the power amplifier. Thus the signal can be accurately recorded for the desired time period.

#### 4.5 SAMPLE MOUNTING

The minimum detectable force must be found in order to determine the minimum sample size which can be mounted onto the oscillator. However, this is not simply the value found in Section 3.4.5 because the properties of the oscillators change significantly when a sample is mounted onto them due to the excess weight that has been added. Therefore, before determining the sample to be mounted, reasonable guesses need to be made for the new values for the Q and the resonance frequency.

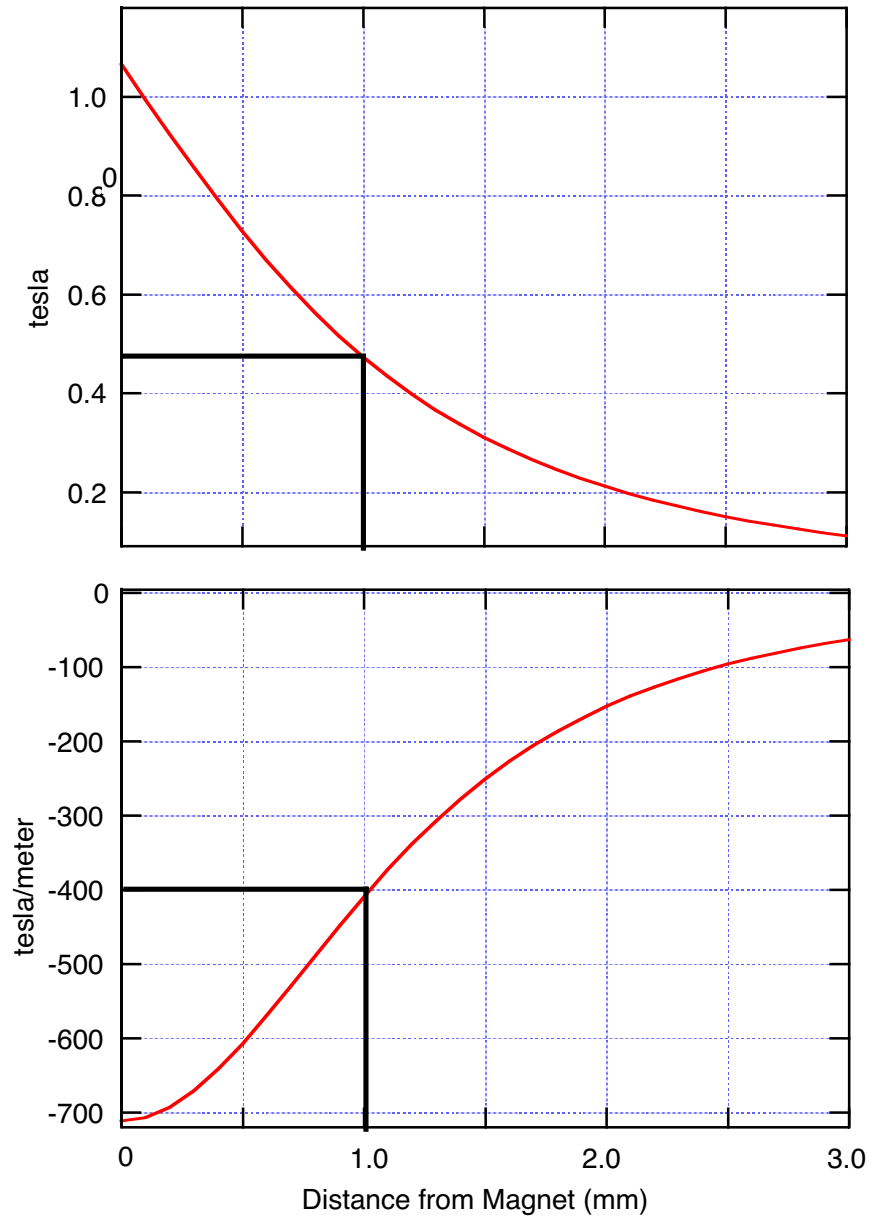


Figure 4.8: (a) Field and (b) field gradient as a function of the distance from the surface of the permanent magnet. Dark lines indicate the expected values 1 mm away.

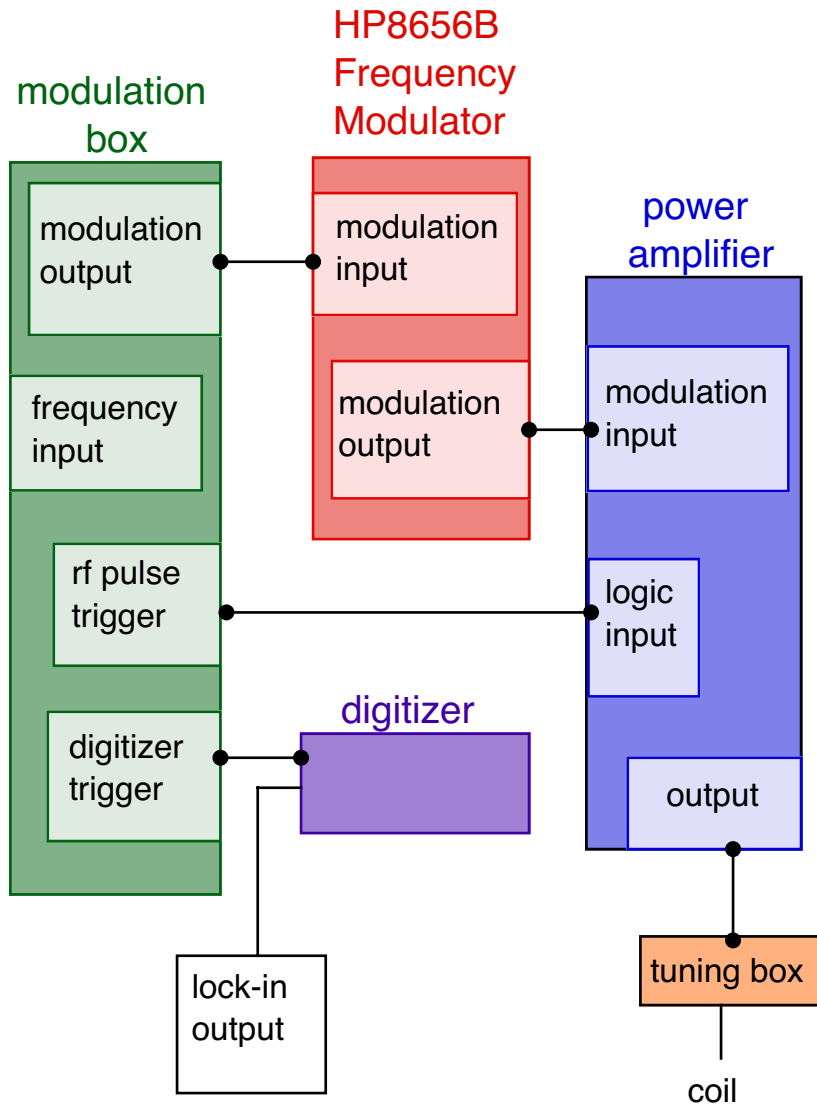


Figure 4.9: Overview of the electronics used for generating the modulation used in cyclic adiabatic inversion.

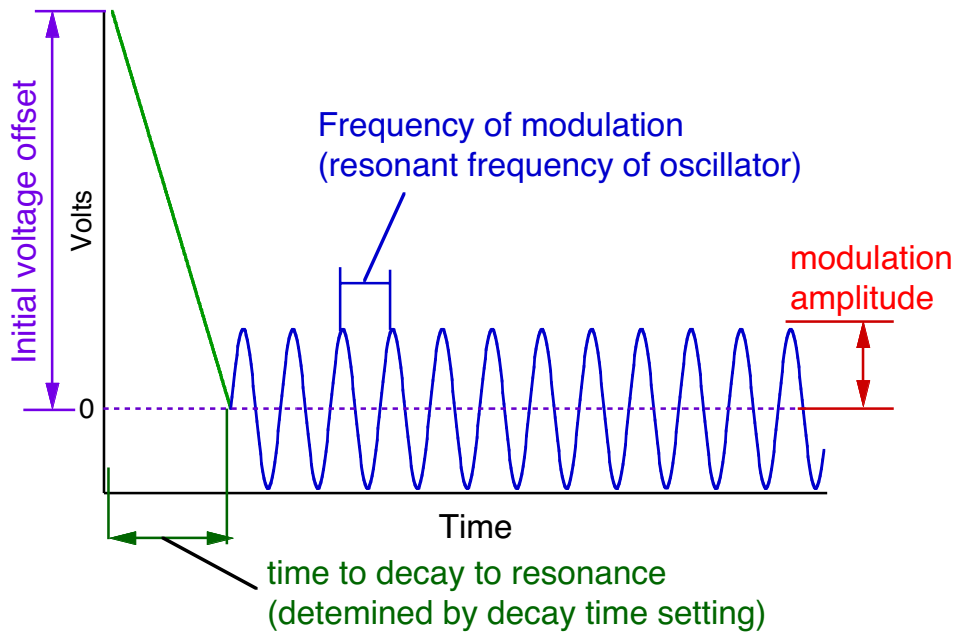


Figure 4.10: Illustration of the voltage output from the modulation box. This output goes to the input of the HP8656B where it gets translated into a frequency modulation about the carrier frequency.

These can then be used in the worksheet shown in Figure 4.11 to calculate the minimum detectable force for these new parameters. Then various sample diameters can be put in to determine the force that would result from a sample of the specified size. It is hoped that the sample size chosen will create a force at least 2 to 5 times larger than the minimum detectable limit, to account for errors in the initial guesses. Once the desired sample size has been determined, the sample mounting process can begin.

This process is done entirely manually. Samples of diameters as small as  $3\ \mu\text{m}$  have been successfully mounted onto the  $50\ \mu\text{m}$  tall head of the double torsional oscillators. See Figure 4.9 for examples. Initially epoxy was used to glue the sample on. However, it was discovered that once the oscillator was excited at resonance, the amplitude of oscillation was large enough for the epoxy to crack, causing the sample

<b>sample.....</b>	NH4Cl			
<b>density.....</b>	1.527	g/cm <sup>3</sup>		
<b>atomic weight.....</b>	53.49	g/mol		
<b>#mole H/mole formula.....</b>	4			
<b>spin density.....</b>	68764957936	#/ $\mu\text{m}^3$	<b>radius</b>	10 $\mu\text{m}$
<b>volume of resonance slice.....</b>	2.09E+03	$\mu\text{m}^3$		
<b>N (# spins @ res).....</b>	1.44E+14			
<b>H_z.....</b>	8.2	Tesla		
<b>Temp.....</b>	300	K		
<b>M (Mag Mom).....</b>	5.67658E-17	J/Tesla		
<b>actual dB/dz.....</b>	300	T/m	3	G/m
<b>Thickness of resonance slice..</b>	6.666666667	$\mu\text{m}$		
<b>Force made by res. slice.....</b>	1.70298E-14	N/Hz <sup>(1/2)</sup>		
<b>Q of oscillator</b>	5000			
<b>resonant frequency</b>	50	kHz		
<b>bandwidth</b>	1	Hz		
<b>torsional k</b>	5E-11	N-m		
<b>spring constant</b>	0.005	N/m		
<b>temperature</b>	300	K		
<b>minimum detectable force</b>	7.26215E-15	N		

Figure 4.11: Excel spreadsheet for calculation of the expected minimal detected force for a given sample.

to fall off. Therefore, grease is currently used for mounting.<sup>3</sup> Grease is thicker than the epoxy and thus it is harder to get a sufficiently small amount onto the oscillator. This needs to be remembered when analyzing the data, since there will most likely be a non-negligible contribution from the mounting grease.

The mounting process uses thin glass fibers which have diameters at their tips of approximately the same diameter of the desired sample size. These are made using the hydrogen torch to melt glass. Two glass tubes are touched together in the blue part of the flame, and when they glow they are quickly and forcefully pulled apart. This results, after some practice, in tapered pieces of glass that are extremely thin at the end. The tapered pieces, which ideally are approximately 2–3 cm long, can be broken off easily. It is recommended that quite a few fibers be made, allowing for various tip diameters from which to choose. A strong taper is desired so that the majority of the fiber is relatively thick, and therefore more resistant to shaking.

Once the fibers have been made, two need to be selected with the desired diameters (corresponding to the desired sample size). A vertical translator has been made onto which the fiber can be attached with tape. This is used along with the *xy*-translation stage and microscope. The 20× magnification is used to allow for a close enough view while still allowing for sufficient room to move underneath. The fiber is attached to the vertical translator and positioned under the microscope so that the tip is in the center of the field of view. A small amount of grease is placed onto a microscope slide and moved into the field of view. The fiber is then gently dipped into the grease and lifted up. The grease is moved away. At this point, there is an excessive amount of grease on the end of the fiber. To remove this, touch the fiber to a clean area of the glass slide multiple times until an amount slightly larger than that desired is on the slide. Carefully translate over to the oscillator and lower the fiber to the head. DO NOT LIFT UP, as this will break the oscillator. Instead,

---

<sup>3</sup>Badly mixed epoxy was also used, with the belief that this would result in a thin yet viscous material. However, this method was extremely hard to repeat accurately, and was therefore unreliable.

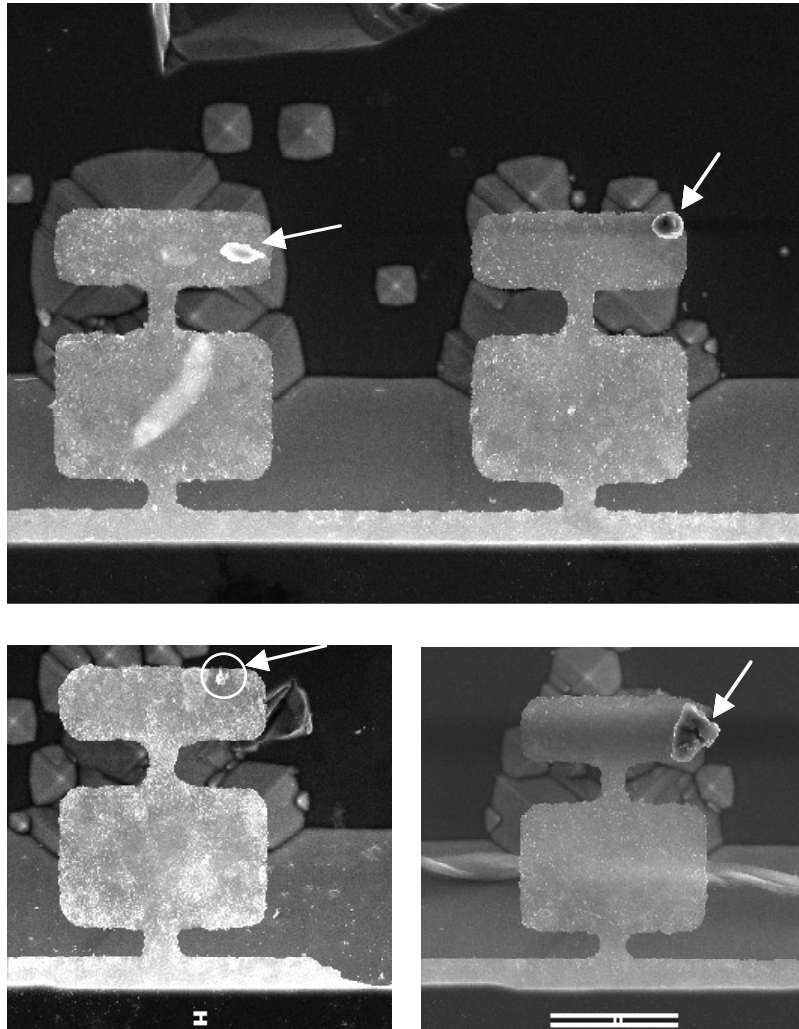


Figure 4.12: SEM images of samples which have been mounted onto the double-torsional oscillators. For length scales, recall the height of the head is  $50 \mu\text{m}$ .

use the  $xy$  translator to slide the fiber off of the oscillator (preferably in a direction parallel to the neck of the oscillator). The oscillator is now ready for the sample to be applied.

If there is an abundance of the desired sample material, then the easiest way to achieve a particle with the desired diameter is to grind up some of the material and spread it over part of the glass slide. Under the microscope, choose the particle with the desired diameter. Use a new fiber, or clean the existing one so there is no grease. Move the desired particle so that it is directly under the tip of the fiber and then slowly move the fiber so that it touches the particle. Electrostatic forces cause the particle to stick so that when the fiber is lifted up, the particle is attached to the end. Multiple tries may be necessary to get the particle on the tip of the fiber. Once this has been accomplished, move the oscillator with the grease on it under the fiber. Slowly touch the particle to the grease, and slide the fiber away. The sample mounting process is complete and the oscillator is ready for characterization.



## CHAPTER 5

### FORCE DETECTION OF NMR: RESULTS OF A 1D SCAN

*“Good.”*

*- The author’s father*

A one-dimensional scan was performed using the set-up described in the previous chapters. A signal of the appropriate strength was observed, and the NMR origin of the signal was verified. The parameters of the experiment will first be detailed, followed by a discussion of the results.

#### 5.1 EXPERIMENTAL PARAMETERS

The first step in doing the experiment was to mount a sample onto a double-torsional oscillator as described in the previous section. The sample chosen was ammonium sulfate ( $(\text{NH}_4)_2\text{SO}_4$ ). This compound was chosen because of its high proton density ( $6.4 \times 10^{22} \text{ } ^1\text{H}/\text{cm}^3$ ), its long relaxation time ( $T_1 \approx 5 \text{ s}$ ) [11], and its availability. A relatively large sample with a radius of  $\approx 10 \text{ } \mu\text{m}$  was attached to the head of the oscillator with N-grease. Vacuum scans were then performed to characterize the resonances of the oscillator and sample. These are shown in Figure 5.1. As expected, the relatively large mass of the sample drastically lowers the resonance frequencies of the thin double-torsional oscillator. Also, due to the mass effects, it was extremely difficult to characterize the exact behavior of the oscillator for each resonance, and

phase-sensitive detection as was described in Section 3.4 was inconclusive. Most likely, the oscillator can no longer be modeled by the simple classical mass-spring configuration. Because of this, the exact spring constant is unknown and is therefore estimated to be 0.01 N/m.

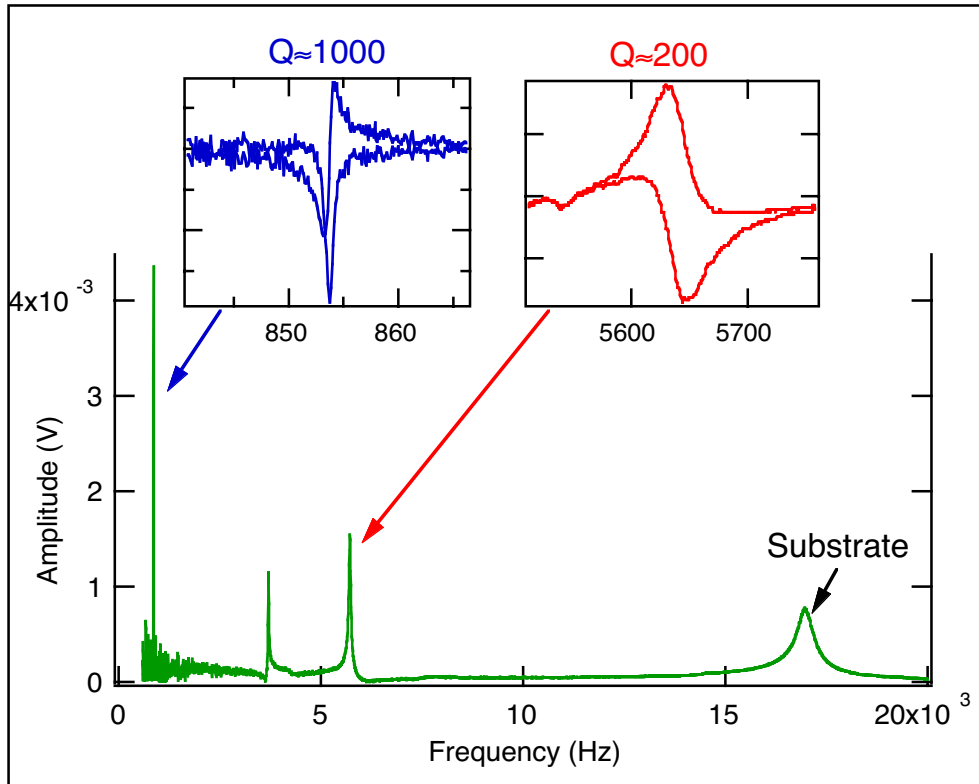


Figure 5.1: Frequency scan of the oscillator plus sample used for the one-dimensional experiment. Both resonances shown have approximately the same force sensitivity of  $5 \times 10^{-15} \text{N/Hz}^{1/2}$ .

Three main oscillator resonances are observed at 850 Hz, 3200 Hz, and 5600 Hz. The lowest frequency has a  $Q$  of 1000, while the two upper frequencies have  $Q$ 's on the order of 200. Therefore, the force sensitivity of the 850 and the 5600 Hz resonances are both on the order of  $5 \times 10^{-15} \text{N/Hz}^{1/2}$ , as calculated by equation 2.19.

The force expected from the sample was then calculated to make sure it was a reasonable amount above the noise level. For this, some estimates had to be made. First, it was assumed that the field gradient at the sample would be on the order of 300 T/m, a reasonable value derived from Figure 4.8. The amplitude of the adiabatic inversion (Figure 5.2),  $\Omega/\gamma$ , was estimated to be  $\approx 25$  G, corresponding to a peak to peak amplitude of 100 kHz about resonance. Therefore the thickness of the resonance shell was found to be approximately 8  $\mu\text{m}$ , resulting in a total of  $1.7 \times 10^{14}$  spins at resonance for the sample. Taking into account the 8.073 T static field from the NMR magnet and the 0.35 T field from the iron bar (see Figure 4.8), the Curie susceptibility of the nuclear magnetization (equation 2.26) yields a magnetic moment of  $6.8 \times 10^{-17} \text{J/T}$ . Using this value with the 300 T/m field gradient gives the value for the force expected from the resonant slice:  $F_{calc} \approx 2 \times 10^{-14} \text{ N/Hz}^{1/2}$ . This value is approximately four times larger than the thermal noise of the oscillator and therefore sufficient for doing a single-sweep experiment.

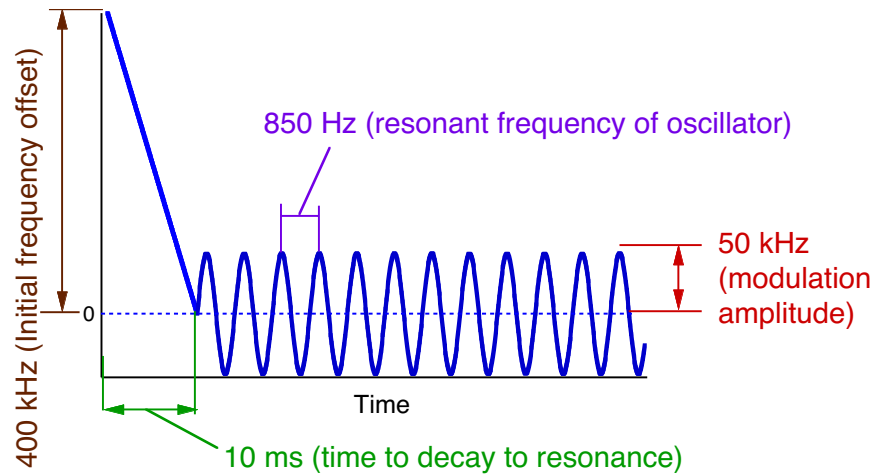


Figure 5.2: Cyclic adiabatic inversion parameters used in the 1D experiment.

The coil was a 3 mm diameter coil with 3.5 turns, positioned 1.5 mm away from the oscillator. The coil was tuned to  $50 \Omega$  using a tank circuit with a parallel and

a series capacitor. It is estimated that the field produced by this coil is on the order of 5 G for a power setting of 38 dBm (= 6.4 W). The iron bar was initially placed 0.8 mm away from the oscillator with the intention of moving it further away in 10  $\mu\text{m}$  steps. A location approximately 1.4 mm away from the oscillator was chosen as the target in order to account for variations in the estimated parameters. The field from the iron bar 1.4 mm away is 0.35 T, assuming full saturation. The exact field from the NMR magnet was 8.073 T. The carrier frequency of the cyclic adiabatic inversion was therefore set to  $\frac{\gamma}{2\pi}H_{total} = (42.577 \text{ MHz/T})(8.073\text{T} + 0.35\text{T}) = 358.6 \text{ MHz}$ . The 860 Hz resonance was chosen due to the larger measured amplitude as well as the 5 times lower speed of inversion, in order to assure the adiabatic condition was met. The cyclic adiabatic inversion began 400 kHz above resonance and decayed in less than 10 ms to the carrier frequency. It then oscillated about this carrier frequency with an amplitude of 50 kHz and a frequency of 858.25 Hz.<sup>1</sup> The rf pulse length was set to 260 ms, giving the oscillator sufficient time to ring up. The lock-in output was recorded in 1 ms intervals for 1 second. The digitizer was pre-triggered so that 200 ms of the signal was taken before the pulse.

The experiment consisted of turning the external control of the magnet translator 36° clockwise in order to move the magnet 10  $\mu\text{m}$  away from the oscillator. The position was recorded, and an rf pulse was sent into the coil as described above. The signal was stored and this procedure was repeated.

## 5.2 RESULTS

### 5.2.1 SIGNAL ARTIFACT

A strong artifact was observed for every signal, even when far off resonance. The origin of this artifact is unknown but has also been observed in other MRFM experiments using cyclic adiabatic inversion [55]. The strength of the signal depended

---

<sup>1</sup>Due to peculiarities with the HP8656B frequency modulator, the value of 400 kHz initial offset and 50 kHz amplitude were fixed and therefore could not be changed to examine the effects on the signal.

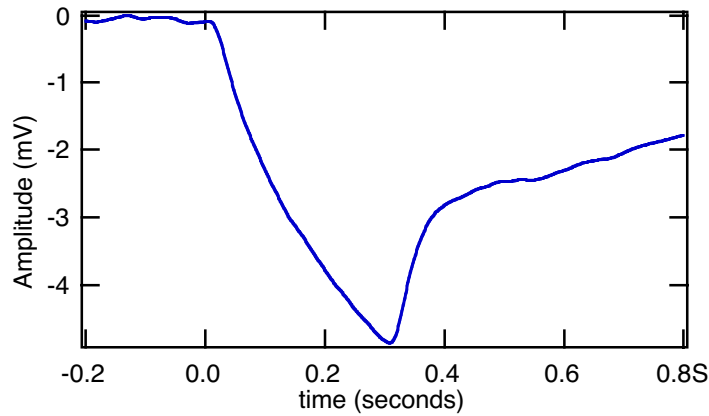


Figure 5.3: Typical average of the artifact signal which is subtracted off.

on the quality of the reflection, but was always approximately five times the noise level. Because of this, the measured signals had to be compared to this standard response in order to detect the actual response from the spins in the sample. In the analysis of the final data, this artifact has been subtracted off. This is done simply by averaging many artifacts measured at varying locations with equivalent qualities of reflection.<sup>2</sup> An example of an average of ten such artifacts is shown in Figure 5.3. The signal behaves mostly as expected: it is flat before the pulse, rings up during the pulse, and decays after the pulse is turned off.<sup>3</sup>

### 5.2.2 SIGNAL CAUSED BY NUCLEAR MAGNETIC RESONANCE

The position of the iron bar was moved in 10  $\mu\text{m}$  steps from 0.8 mm to 1.9 mm. Eventually, it was discovered that the signal to noise ratio appeared to increase in the vicinity of 1.3 mm, indicating an added contribution to the signal besides that of the artifact. This area was carefully scanned in both directions, and the resulting

<sup>2</sup>Due to thermal drifting and mechanical shaking, the detected amplitude at resonance for a given amount of applied voltage to the piezo resulted in as much as a factor of two discrepancy. Therefore, the magnitude of resonance for a 0.1 V drive voltage sent into the piezo shaker was recorded before every signal in order to know the quality of reflection.

<sup>3</sup>The cause of the odd decay behavior observed from about 0.4 seconds is unknown.

measurements are shown by the solid circles in Figure 5.4. Each point is the result of one signal which has had the artifact subtracted. The value of the adjusted signal is then found at the end of the pulse, and this is the value plotted. No averaging has been performed, other than that used to subtract the artifact. Thus this proves to be a successful single-sweep experiment. From the data it is clear that there is a peak at 1.290 mm with a width of 20  $\mu\text{m}$ , approximately the same size as the sample.

This however is inconclusive by itself. To verify the NMR origin of this signal, the frequency was shifted up by 1 MHz to 359.6 MHz. This corresponds to  $\approx 0.025$  T, corresponding to roughly 100  $\mu\text{m}$  in the region 1.3 mm away from the sample (Figure 4.8). Therefore, it would be expected that this new frequency would result in the resonance moving approximately 100  $\mu\text{m}$  towards the oscillator. The open squares in Figure 5.4 indicate that this was indeed observed. The peak shifted towards the oscillator by  $\approx 90\mu\text{ m}$ , and the width was still  $\approx 20\mu\text{ m}$ .<sup>4</sup>

To further investigate the observed signal, the magnet was held at the fixed position of 1.2 mm and the frequency was scanned. This added the benefit of eliminating discrepancies in adjacent signals due to the mechanical shaking caused by turning the magnet positioner. Therefore the quality of reflection remained constant for each point of the frequency scan. The results of this frequency sweep are given in Figure 5.5. A peak is observed at 359.6 MHz as expected. The width of the peak is  $\approx 0.4$  MHz, which corresponds to  $\approx 40\ \mu\text{m}$ . This is larger than the width observed in the position scans but still in the expected range.

The measured values of the noise and the force due to the sample can now be compared to those predicted in Section 5.1. First, the measured noise is on the order of a few tenths of a mV, as can be seen in Figure 5.4. The fringes had an approximate amplitude from 0.1 V to 0.2 V peak to peak, corresponding to an amplitude conversion of 1 mV  $\approx$  1 nm (Section 4.2.2). Thus the measured noise level

---

<sup>4</sup>The strength of the signal increased by a small amount due to the better reflection which was achieved for the later scans. However, the noise also increased as is expected.

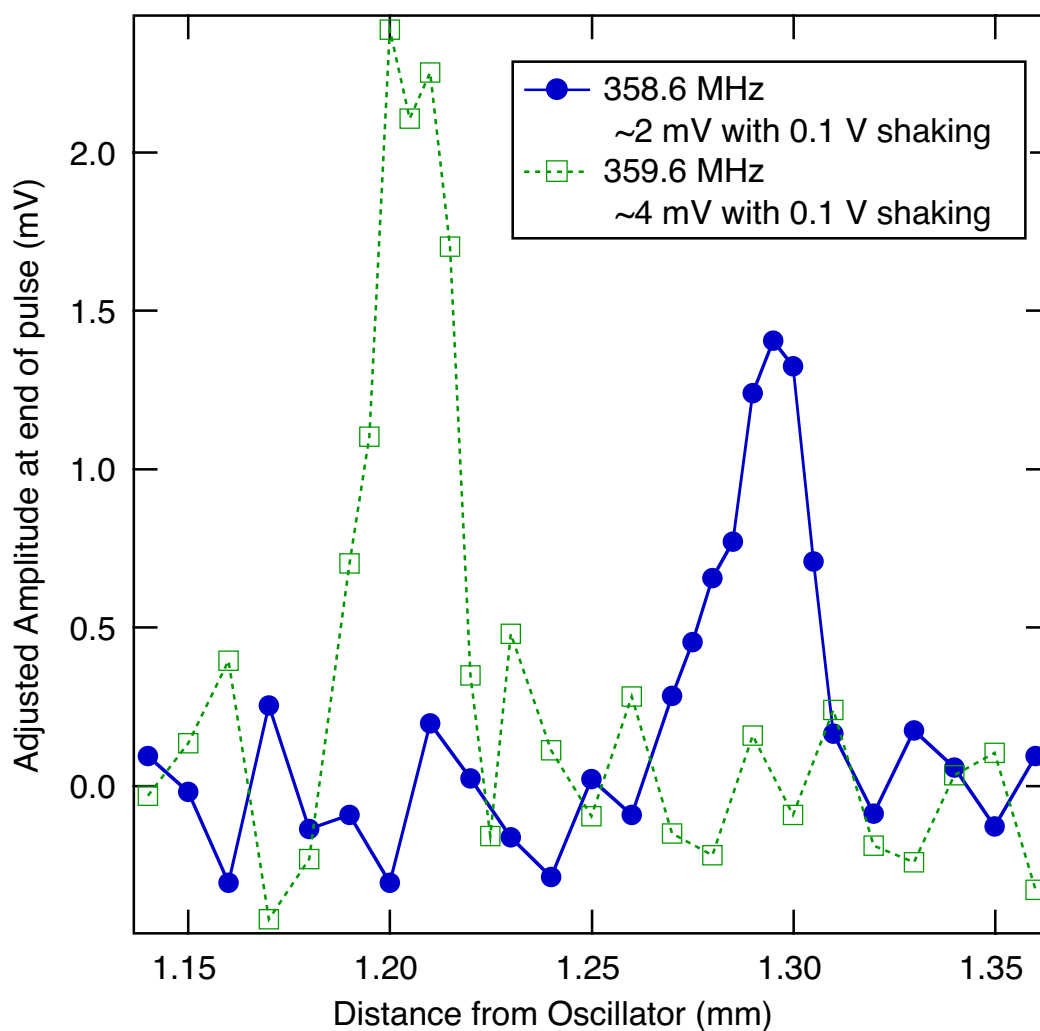


Figure 5.4: Results of a position scan at two different frequency values, verifying the NMR nature of the signal. A  $90 \mu\text{m}$  shift is observed for a 1 MHz change, as is expected from the magnetic field predictions.

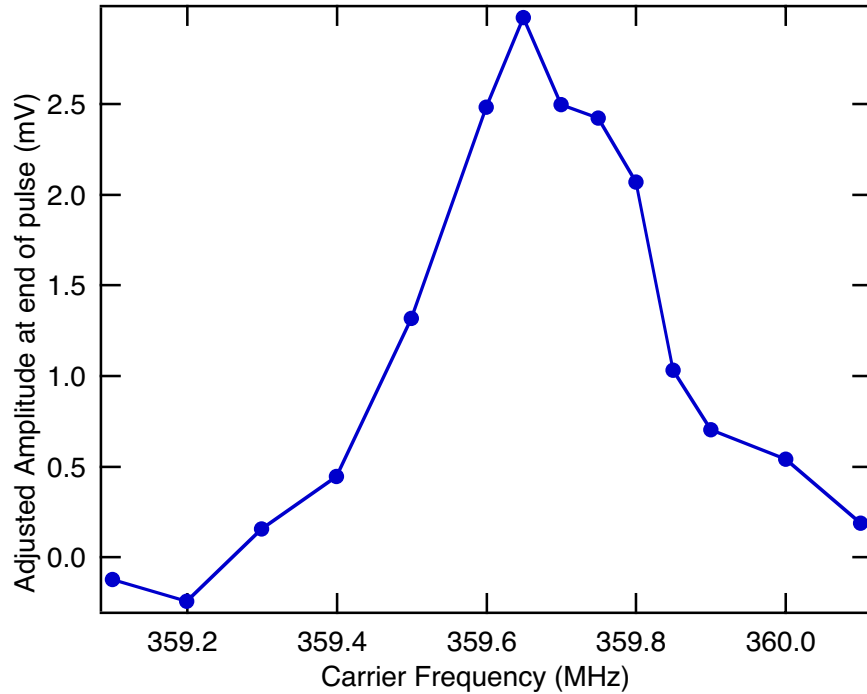


Figure 5.5: Results of scanning the frequency while keeping the position fixed at 1.20 mm.

of  $\approx 0.3$  mV corresponds to 3 angstroms. Using a  $Q$  of 1000 and a spring constant of  $0.01$  N/m, this translates to a noise level of  $3 \times 10^{-15}$  N/Hz $^{1/2}$ , in good agreement with the calculated value of  $5 \times 10^{-15}$  N/Hz $^{1/2}$ .

The signal strength is on the order of 1.5 mV, corresponding to roughly 15 angstroms. This equals a measured force from the sample of  $1.5 \times 10^{-14}$  N/Hz $^{1/2}$ , in excellent agreement with the predicted value of  $2 \times 10^{-14}$  N/Hz $^{1/2}$ .

### 5.3 SUMMARY

Double torsional micro-oscillators have been designed specifically for use in a nuclear magnetic resonance force microscope. These boron-doped single-crystal silicon oscillators were made using micro-electronic fabrication techniques, including a crucial KOH wet-etch as the final process step. The effects of the orientation, anneal pa-



rameters (time and temperature), and doping specifications (dose and energy) on the final structure were examined. The oscillator resonances were characterized using a fiber-optic interferometry system with a piezo feedback circuit for fringe stability. Four resonances were generally found with frequencies in the desired range for cyclic adiabatic inversion ( $< 100$  kHz) and with quality factors of the upper resonances on the order of 10,000 at room temperature.

In addition, the process of manipulating the magnetization using cyclic adiabatic inversion was examined. The adiabatic condition was derived exactly as a function of the angle that the effective field (initially) makes with the external field. Non-adiabatic and relaxation effects during inversion were considered separately, and the effect of each on the observed signal was modeled. Pulse sequences were given which can be used to measure the spin-lattice relaxation times of a sample, as is commonly done in conventional NMR.

Finally, the results presented in this chapter clearly show that the nuclear magnetic resonance of a sample of ammonium sulfate has been successfully detected by coupling the magnetic force from the spins to a double torsional micro-oscillator. Single-sweep sensitivity of  $3 \times 10^{-15}$  N/Hz<sup>1/2</sup> and a signal-to-noise ratio of 5 were observed at room temperature for a sample-on-oscillator configuration. With no sample mounted, the upper resonances of the oscillators were found to have force sensitivities as low as  $1.5 \times 10^{-16}$  N/Hz<sup>1/2</sup> at room temperature. It is believed that the magnet-on-oscillator experimental configuration will allow for the high-Q characteristic of these multiple-torsional oscillators to be used without the large loss of sensitivity inherent in the sample-on-oscillator configuration.

## Appendices

## APPENDIX A

### RELEVANT REFERENCE VALUES

#### Fundamental Constants

$\gamma$  for  $^1\text{H}$ :  $2\pi \times 42.577$  MHz/T

$k_B$ :  $1.38 \times 10^{-23}$  J/K

$\mu_n$ :  $5.051 \times 10^{-27}$  J/T

$\mu_p$ :  $1.4 \times 10^{-26}$  J/T

#### Information on Silicon

Density:  $2.33$  g/cm<sup>3</sup>

Shear Modulus ( $G$ ) for Si:  $6.63 \times 10^{11}$  dynes/cm<sup>2</sup>

Shear Modulus ( $G$ ) for Si<sub>3</sub>N<sub>4</sub>:  $1 \times 10^{12}$  dynes/cm<sup>2</sup>

Elastic Modulus ( $E$ ):  $1 \times 10^{12}$  dynes/cm<sup>2</sup> for Si at 300K

Unit cell:  $a = 0.543$  nm

p++ concentration necessary for KOH etch stop:  $1 \times 10^{20}$  ions/cm<sup>3</sup>

Solid solubility limit of boron in silicon:  $6 \times 10^{20}$  ions/cm<sup>3</sup>

Activation energy ( $E_a$ ) for (100) Si surface:  $0.595$  eV

Activation energy ( $E_a$ ) for (110) Si surface:  $0.60$

**Spin Densities**

Ammonium Sulfate:  $6.4 \times 10^{22} \text{ } ^1\text{H}/\text{cm}^3$

Ammonium Nitrate:  $5.1 \times 10^{22} \text{ } ^1\text{H}/\text{cm}^3$

Ammonium Chloride:  $6.9 \times 10^{22} \text{ } ^1\text{H}/\text{cm}^3$

## APPENDIX B

### FRINGE-STABILITY CIRCUIT: DIRECTIONS FOR USE

This is a step-by-step list of the directions for using the fringe-stability feedback box. As experience is acquired, it becomes extremely easy to keep the fringe locked onto a fringe for up to eight hours. Note that the gain knob is always set at its maximum value and does not need to be adjusted. The time constant can be adjusted by a screw inside the circuit, but this is not recommended. If problems arise because of the time constant, it is recommended, instead, that the signal be amplified by a reasonable factor to allow for larger fringes. This is done by putting a larger resistor into the op-amp circuit as was described in Section 4.2.1.

1. As mentioned in Section 4.2.2, it is first required that you have a fringe height of at least 0.15 Volts, corresponding to a total peak to peak fringe height of 0.3 V. With the box in the off position, align the fiber so that this is the case.
2. Make sure the voltage power supply is on and the switch on the box is on manual. Then switch the box on.
3. Slowly turn the P- piezo input and watch the DC level monitor. The voltage should be fluctuating as the fiber is moved through each fringe. Make a note of the average DC level and the peak-to-peak fringe height.
4. Adjust the P- input so that it can be moved in either direction. In other words, do not leave the P- knob completely to the left or right. (This will allow for fine adjustments while the automatic control is on, allowing for longer fringe-locking

capability.) Then make the fine adjustments on the P- input so that the DC level is approximately at its average value.

5. When the DC level is at its average value, look at the output from the box titled “error”. Adjust the setpoint knob until the output of this reads zero when the DC level is at its average value. The P- output may have to be readjusted a few times while monitoring the error output in order to make sure that the error output reads zero at the average value of the DC level. (This is the step in which the setpoint is determined. This is the value onto which the box will lock, therefore it is extremely important to lock onto the linear region.)

6. Once the setpoint has been calibrated, the box can be turned to automatic. Flip this switch and monitor the P+ voltage going to the piezo. Up to this point, it should have been zero. Once the box is switched to automatic mode, this value should jump to some finite value between +15 and -15 volts.

7. If the P+ reading is saturated at 15 V<sup>1</sup> then it was not able to lock onto a fringe. If this is the case, then switch back to manual mode and adjust P- so that the fiber moves to a neighboring fringe. Then turn the box back to automatic. Do this until the box locks. If it never locks, then most likely the alignment is not good enough or there is some strong source of external noise in the lab.

8. Once the box has been locked on, the fiber optic system is ready for measurements. However, for extended measurements, it is recommended that the P+ output is monitored frequently. Using the manual P- control, the P+ value can be kept around zero.

9. To turn the box off, simply switch the box to automatic and then switch it off.

It is also relevant here to mention that the noise level when the probe is in the NMR magnet is significantly lower than it is when the probe is on the table.

---

<sup>1</sup>Actually, the box tends to saturate at around 13.5 Volts, not 15 V.

Therefore when the probe is in the magnet, it is possible to manually lock onto a fringe. It will remain stable enough to perform accurate characterization scans. However, on the table, the fringe-locking circuit is necessary to keep the detection level below that of the thermal noise level.

## BIBLIOGRAPHY

- [1] J. A. Sidles, *Appl. Phys. Lett.* **58** (1991) 2854.
- [2] J. A. Sidles, *Phys. Rev. Lett.* **68** (1992) 1124.
- [3] J. A. Sidles, J. L. Garbini, and G. P. Drobny, *Rev. Sci. Instrum.* **8** (1992) 3881.
- [4] D. Rugar, C. S. Yannoni, and J. A. Sidles, *Nature* **360** (1992) 563.
- [5] O. Zuger and D. Rugar, *Appl. Phys. Lett.* **63** (1993) 2496.
- [6] K. Wago, D. Botkin, C. S. Yannoni, and D. Rugar, *Phys. Rev. B* **57** (1998) 1108.
- [7] K. Wago, O. Zugar, J. Wegener, R. D. Kendrick, C. S. Yannoni, and D. Rugar, *Rev. Sci. Instrum.* **68** (1997) 1823.
- [8] K. J. Bruland, J. Krzystek, J. L. Garbini, and J. A. Sidles, *Rev. Sci. Instrum.* **66** (1995) 2853.
- [9] D. Rugar, O. Zugar, S. Hoen, C. S. Yannoni, H.-M. Vieth, and R. D. Kendrick, *Science* **264** (1994) 1560.
- [10] See note (6) in ref. [6]
- [11] O. Klein, V.V. Naletov, and H. Alloul, *Eur. Phys. J. B* **17** (2000) 57.
- [12] Arnd Schaff and Wiebren S. Veeman, *J. Mag. Res.* **126** (1997) 200.
- [13] K. Wago, O. Zugar, R. Kendrick, C. S. Yannoni, and D. Rugar, *J. Vac. Sci. Technol. B* **14** (1996) 1197.



- [14] O. Zugar, S. T. Hoen, C. S. Yannoni, and D. Rugar, *J. Appl. Phys.* **79** (1996) 1881.
- [15] T.A. Barrett, C. R. Miers, H. A. Sommer, K. Mochizuki, and J. T. Markert, *J. Appl. Phys.* **83** (1998) 6235.
- [16] K. J. Bruland, J. L. Garbini, W. M. Dougherty, and J. A. Sidles, *J. Appl. Phys.* **83** (1998) 3972.
- [17] K. J. Bruland, J. L. Garbini, W. M. Dougherty, and J. A. Sidles, *J. Appl. Phys.* **80** (1996) 1959.
- [18] D. Canet, *Nuclear Magnetic Resonance: Concepts and Methods* New York: John Wiley and Sons, Inc. (1996).
- [19] C. P. Slichter, *Principles of Magnetic Resonance, 2nd edition* New York: Springer-Verlag (1978).
- [20] E. Fukushima and S. G. W. Roeder, *Experimental Pulse NMR: A Nuts and Bolts Approach* New York: Addison-Wesley Publishing (1981).
- [21] N. W. Ashcroft and N. D. Mermin, *Solid State Physics* Philadelphia: Saunders College (1976).
- [22] J. A. Sidles, J. L. Garbini, K. J. Bruland, D. Rugar, O. Zuger, S. Hoen, and C. S. Yannoni, *Rev. Mod. Phys.* **67** (1995) 249.
- [23] C. P. Slichter, *Principles of Magnetic Resonance, 2nd edition* Chap. 5, pp 167, New York: Springer-Verlag (1978).
- [24] E. Fukushima and S. G. W. Roeder, *Experimental Pulse NMR: A Nuts and Bolts Approach* Chap. 4, pp 236, New York: Addison-Wesley Publishing (1981).
- [25] D. Canet, *Nuclear Magnetic Resonance: Concepts and Methods* Chap. 4, pp 184, New York: John Wiley and Sons, Inc. (1996).

- [26] C. P. Slichter, *Principles of Magnetic Resonance, 2nd edition* Chap. 6, pp 213, New York: Springer-Verlag (1978).
- [27] R. N. Kleiman, G. K. Kaminsky, J. D. Reppy, R. Pindak, and D. J. Bishop, *Rev. Sci. Instrum* **56** (1985) 2088.
- [28] Xiao Liu, S. F. Morse, J. F. Vignola, D. M. Photiadis, A. Sarkissian, M. H. Marcus, and B. H. Houston, *Appl. Phys. Lett.* **78** (2001) 1346.
- [29] C. L. Spiel, R. O. Pohl, and A. T. Zehnder, *Rev. Sci. Instrum.* **72** (2001) 1482.
- [30] S. D. Timoshenko and J. N. Goodier, *Theory of Elasticity* New York: McGraw-Hill (1970).
- [31] W. C. Young, *Roark's Formulas for Stress and Strain* New York: McGraw-Hill (1989).
- [32] A. Torii, M. Sasaki, K. Hane, and S. Okuma, *Meas. Sci. Technol.* **7** (1996) 179.
- [33] T. D. Stowe, K. Yasumura, T. W. Kenny, D. Botkin, K. Wago, and D. Rugar, *Appl. Phys. Lett.* **71** (1997) 288.
- [34] S. K. Ghandhi, *VLSI Fabrication Principles Silicon and Gallium Arsenide, 2nd ed.* New York: John Wiley and Sons, Inc. (1994).
- [35] H. Seidel, L. Csepregi, A. Heuberger, and H. Baumgartel, *J. Electrochem. Soc.* **137** (1990) 3626.
- [36] I. P. Kozlov, V. B. Odzhaev, V. N. Popok, and V. Hnatowicz, *Semicond. Sci. Technol.* **11** (1996) 722.
- [37] G. Schropfer, S. Ballandras, M. de Labachellerie, P. Blind, and Y. Ansel, *J. Micromech. Microeng.* **7** (1997) 71.
- [38] <http://www.duke.edu/web/wbl/ch7/ch7-hpge.html#7.2.2.1>

- [39] M. Elwenspoek, *J. Micromech. Microeng.* **6** (1996) 405.
- [40] H. Seidel, L. Csepregi, A. Heuberger, and H. Baumgartel, *J. Electrochem. Soc.* **137** (1990) 3612.
- [41] N. F. Raley, Y. Sugiyama, and T. Van Duzer, *J. Electrochem. Soc.* **131** (1984) 161.
- [42] P. R. Scheeper, J. A. Voorthuyzen, W. Olthius, and P. Bergveld, *Sens. and Act. A* **30** (1992) 231.
- [43] C. Seassal, J. L. Leclercq, and P. Viktorovitch, *J. Micromech. Microeng.* **6** (1996) 261.
- [44] R. Legtenberg, H. A. C. Tilmans, J. Elders, and M. Elwenspoek, *Sens. and Act. A* **43** (1994) 230.
- [45] H. Kawakatsu, H. Toshiyoshi, D. Saya, K. Fukushima, and H. Fujita, *J. Vac. Sci. Technol. B* **18** (2000) 607.
- [46] M. D. Chabot and J. T. Markert, *Proc. of the SPIE* **3875** (1999) 104.
- [47] Xidex Corporation, private communication.
- [48] A. Barr, *UT Austin Dissertation* (1996).
- [49] T. R. Albrecht, P. Grutter, D. Rugar, and D. P. E. Smith, *Ultramicroscopy* **42** (1992) 1638.
- [50] D. Rugar, H. J. Mamin, R. Erlandsson, J. E. Stern, and B. D. Terris, *Rev. Sci. Instrum.* **59** (1988) 2337.
- [51] D. Rugar, H. J. Mamin, and P. Guethner, *Appl. Phys. Lett.* **55** (1989) 2588.
- [52] A. D. Drake and D. C. Leiner, *Rev. Sci. Instrum.* **55** (1984) 162.

- [53] J. A. Marohn, Raul Fainchtein, and D. D. Smith, *Appl. Phys. Lett.* **73** (1998) 1998.
- [54] J. D. Hannay, R. W. Chantrell, and D. Rugar, *J. Appl. Phys.* **87** (2000) 6827.
- [55] D. D. Smith, private communication.

## VITA

Michelle Diane Chabot was born on June 21, 1974 in Hollywood, California to Mary and Paul Chabot. She graduated from Rice University, Houston, in May 1996 with a Bachelor's degree in physics and mathematics. From there, she went to the Physics Department of the University of Texas at Austin to begin her graduate career. She had the good fortune of meeting Dr. John T. Markert and began to work in his Superconductivity and Magnetism Lab. She received her Master's degree in 1998 with work done on a semi-adiabatic calorimetry experiment. Her Ph.D. work focussed her attention on the novel field of magnetic resonance force microscopy. After graduation, she will move to Boulder, Colorado, where she has received a NRC postdoctoral fellowship to work with Dr. John Moreland.

Permanent address: 2401 S. Lakeshore  
Austin, Texas 78741

This dissertation was typeset with  $\text{\LaTeX}^\ddagger$  by the author.

---

<sup>‡</sup> $\text{\LaTeX}$  is a document preparation system developed by Leslie Lamport as a special version of Donald Knuth's  $\text{\TeX}$  Program.